June 2017

Lagrangian Visualization and Real-Time Identification of the Vortex Shedding Time in the Wake of a Circular Cylinder

Matthew Rockwood
Syracuse University

Abstract

The flow around a circular cylinder, a canonical bluff body, has been extensively studied in the literature to determine the mechanisms that cause the formation of vortices in the cylinder wake. Understanding of these mechanisms has led to myriad attempts to control the vortices either to mitigate the oscillating forces they cause, or to augment them in order to enhance mixing in the near-wake. While these flow control techniques have been effective at low Reynolds numbers, they generally lose effectiveness or require excessive power at Reynolds numbers commonly experienced in practical applications. For this reason, new methods for identifying the locations of vortices and their shedding time could increase the effectiveness of the control techniques. In the current work, two-dimensional, two-component velocity data was collected in the wake of a circular cylinder using a planar digital particle image velocimetry (DPIV) measurement system at Reynolds numbers of 9,000 and 19,000. This experimental data, as well as two-dimensional simulation data at a Reynolds number of 150, and three-dimensional simulation data at a Reynolds number of 400, is used to calculate the finite-time Lyapunov exponent (FTLE) field. The locations of Lagrangian saddles, identified as non-parallel intersections of positive and negative-time FTLE ridges, are shown to indicate the timing of von Kármán vortex shedding in the wake of a circular cylinder. The Lagrangian saddle found upstream of a forming and subsequently shedding vortex is shown to clearly accelerate away from the cylinder surface as the vortex begins to shed. This provides a novel, objective method to determine the timing of vortex shedding. The saddles are impossible to track in real-time, however, since future flow field data is needed for the computation of the FTLE fields. In order to detect the Lagrangian saddle acceleration without direct access to the FTLE, the saddle dynamics are connected to measurable surface quantities on a circular cylinder in cross-flow. The acceleration of the Lagrangian saddle occurs simultaneously with a maximum in lift in both numerical cases, and with a minimum in the static pressure at a location slightly upstream of the mean separation location in the numerical cases, as well as the experimental data at a Reynolds number of 19,000. This allows the von Kármán vortex shedding time, determined objectively by the acceleration of the Lagrangian saddle away from the circular cylinder, to be detected by a minimum in the static pressure at one location on the cylinder, a quantity that can be measured in real-time using available pressure sensors. These results can be used to place sensors in optimal locations on bluff bodies to inform closed-loop flow control algorithms of the timing of von Kármán vortex shedding.

Lagrangian Visualization and Real-Time Identification of the Vortex Shedding Time in the Wake of a Circular Cylinder

by

Matthew P. Rockwood
B.S. Clarkson University, August 2011
M.S. Syracuse University, December 2012

SUBMITTED IN PARTIAL FULFILLMENT OF THE
REQUIREMENTS FOR THE DEGREE OF
DOCTOR OF PHILOSOPHY
IN
MECHANICAL AND AEROSPACE ENGINEERING
AT
SYRACUSE UNIVERSITY

May 2017

Acknowledgements

I would like to take this opportunity to thank all of the people that helped me complete this work. First and foremost, my wife Danica, whose unwavering support has kept me motivated through periods of travel, working long hours, and frustration when progress was slow. I would also like to thank my parents for their guidance throughout my time in school, as well as serving as great roles models in STEM.

I would like to thank my advisor, Dr. Melissa Green, for giving me the opportunity to be her first graduate student. I enjoyed helping build the Green Fluids Laboratory from empty rooms to functional spaces full of exciting research. I especially appreciate her giving me the freedom to pursue topics of interest in my research, while also pointing me in the direction of useful results. I would like to thank Dr. John Dannenhoffer, Dr. Jacques Lewalle, and Dr. Mark Glauser for all their assistance with research questions, and for their helpful feedback during my thesis proposal.

I would like to thank all of the past and present students at Syracuse University who assisted me in my work. I would like to thank past graduate students Dr. Patrick Shea, Dr. Zachary Berger, and Dr. Christopher Ruscher. They provided guidance on data collection, analysis methods, and writing papers, and I can't thank them enough for all the advice they gave. I am especially thankful to Dr. Patrick Shea for all of his assistance early on in graduate school, for teaching me how to collect data using PIV, and helping me set up experiments. I would like to thank all of the past and current members of the Green Fluids Laboratory for all of their help and support. I would like to thank past undergraduate researchers Jacob Morrida, Ranbir Dhillon, and Evan Hyde for assisting with data collection and analysis. In particular, I would like to thank Yangzi Huang and Justin King. Our many conversations about our work have expanded my perspective and strengthened my research. I would also like to thank them for helping to keep things fun along the way.

I am indebted to Dr. Kunihiko Taira's research group at Florida State University for providing large quantities of high quality numerical data for me to analyze. I would like to thank Phillip Munday and Robert Reger (advised by Dr. Louis Cattafesta) for

providing me with the datasets that I used as the basis for all of my work. I would like to especially thank Yiyang Sun for taking the time to set up and run a three-dimensional simulation that took valuable time away from her own work to provide invaluable data for my analysis. I would also like to thank Dr. Kunihiko Taira for his assistance on papers and advice on research.

I would like to thank the staff in the Mechanical and Aerospace Engineering Office, particularly Kristin Shapiro, Kathy Datthyn-Madigan, Kelly Jarvi and Linda Lowe, for their help with all of the paperwork associated with getting through graduate school. I would like to thank John Banas, Dick Chave, and Bill Dossert in the Engineering Machine Shop for all of their help designing and machining the equipment I used throughout my time at SU. Special thanks to Dick Chave for his fantastic work on the two-piece aluminum cylinder I used in the final portion of my research.

This work was supported by AFOSR Award No. FA9550-14-1-0210, and the Syracuse University Fellowship Program.

Contents

List of Figures

List of Tables

Chapter 1

Introduction

1.1 Circular Cylinder

A bluff body is a non-streamlined object where significant portions of the body experience separated flow when immersed in a moving fluid. Circular cylinders in cross-flow are a canonical bluff body for the study of flow separation and vortex shedding, and have been the focus of research for over 100 years. The vortex shedding process causes the bluff body to experience oscillating forces, which can decrease the longevity of structures built with a non-streamlined cross-section. Vortex shedding can also be beneficial as an unsteady bluff body wake can increase mixing rates for reacting flows and heat exchangers. For a wide range of flow regimes, the complex three-dimensional wake produced by flow around a circular cylinder has proven to be a challenging problem to fully understand and control. Research has focused on topics ranging from the characterization of the vortex dynamics, analysis of the transition from the steady separation bubble to unsteady vortex shedding, stability analysis, analysis of the fluctuating forces, and attempts to control various aspects of the vortex shedding and flow separation. While an understanding of flow separation and vortex shedding can be applied to many flows, such as aircraft wings at high angles of attack, wind turbine blades, combustion, and turbomachinery, the specific understanding of flow around a circular cylinder also has direct importance in the design of smokestacks, oil risers, and long suspended cables.

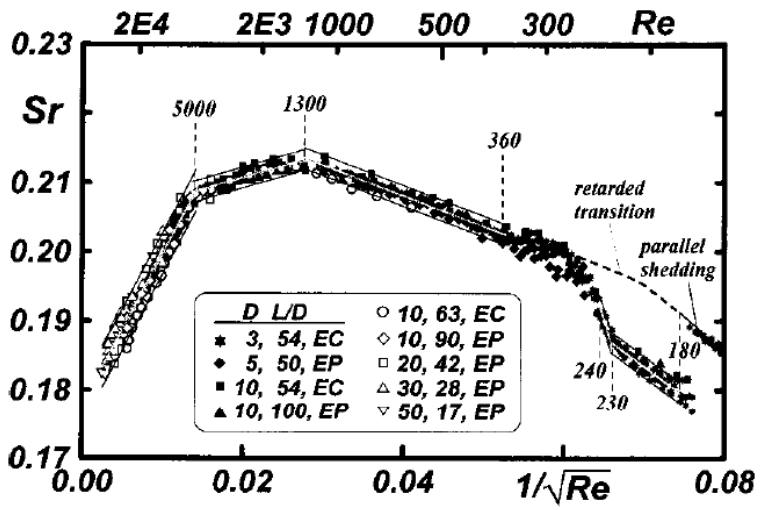

Figure 1-1: Strouhal-Reynolds number relationship from Fey et al. (1998).

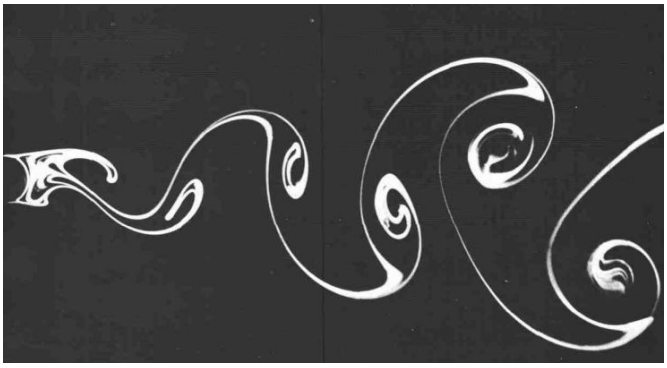

Figure 1-2: Flow visualization of the von Kármán vortex street from Van Dyke (1982).

1.1.1 Bluff Body Vortex Shedding

Many researchers have studied the wake of a circular cylinder in an attempt to gain a full understanding of the physics that causes the formation and shedding of vortices. The primary non-dimensional parameter that governs the wake behavior of a circular cylinder is the Reynolds number, Re, which is defined as

$$Re = \frac{U_\infty D}{\nu}, \tag{1.1}$$

where U_∞ is the free stream velocity, D is the cylinder diameter, and ν is the kinematic viscosity of the working fluid. When the Reynolds numbers is at $\mathcal{O}(1)$, the flow stays fully attached around the circular cylinder, but as Re is increased to $\mathcal{O}(10)$ a steady

separation bubble develops immediately downstream of the circular cylinder. Once Re reaches a value around 47 (the actual value is dependent on surface roughness and free stream turbulence) the steady separation bubble begins to oscillate and breaks down into an unsteady laminar wake characterized by vortices being shed alternatively from the upper and lower portions of the cylinder in the classic von Kármán vortex street (Von Kármán and Rubach, 1912). The non-dimensional frequency associated with the von Kármán vortices is the Strouhal number, St, which is defined as

$$St = \frac{fD}{U_\infty}, \tag{1.2}$$

where f is the von Kármán vortex shedding frequency, D is the cylinder diameter, and U_∞ is the free stream velocity. Fey et al. (1998) studied the relationship between St and Re, and a plot from their study is shown in figure 1-1, where they used Sr to indicate the Strouhal number. While there is large variation in the Strouhal number across the range of Reynolds numbers plotted, there is a nearly constant Strouhal number of 0.21 between the Reynolds numbers of 500 and 5,000.

The von Kármán vortices formed in the cylinder wake have alternating signs of vorticity associated with their respective shear layer, and induce oscillating forces on the cylinder that can lead to structural fatigue (Baarholm et al., 2006; Tognarelli et al., 2008). An example of the von Kármán vortex street from Van Dyke (1982) is shown in figure 1-2. The von Kármán vortex street persists through a large range of Re, with evidence being found up to $Re = 8.4 \times 10^6$ (Roshko, 1961). Coutanceau and Defaye (1991) present clear visualizations of the cylinder wake over a range of Re, and Williamson (1996) contains a thorough description of the changes in the vortex wake as Re is increased, which is summarized below.

Once the Reynolds number is increased to about 190, the previously fully two-dimensional laminar wake begins to be affected by three-dimensional turbulence, which causes spanwise variation in the von Kármán vortices as well as the formation of streamwise-oriented vortices. These streamwise vortices have a spanwise wavelength of three diameters, and are referred to as mode A shedding (Williamson, 1996). As Re is increased

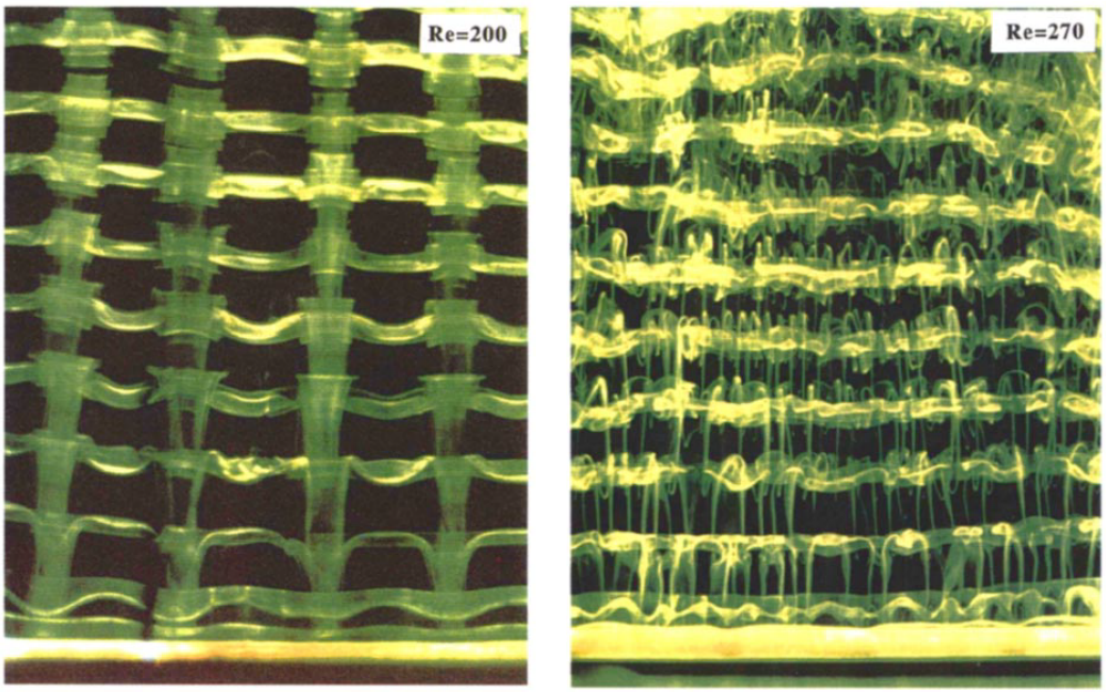

(a) Mode A shedding at $Re = 200$.

(b) Mode B shedding at $Re = 270$.

Figure 1-3: Flow visualization of mode A and B shedding from Williamson (1996). Flow is from bottom to top. Vortices are colored by fluorescein dye (green).

to 250, the wavelength of the streamwise vortices gradually decreases to one diameter, which is referred to as mode B shedding. Mode A and B shedding can be seen in figure 1-3 from Williamson (1996). The vortex formation distance, which is the distance downstream that the von Kármán vortices form behind the cylinder, gradually increases with increasing Reynolds number for this range of Reynolds numbers between 190 and 1,000. At the same time, the location that the wake transitions from laminar flow to turbulent flow gradually moves upstream, as shown by the dye flow visualizations of Gerrard (1978). Once Re reaches 500, this transition has reached the edge of the formation region just behind the cylinder, resulting in the breakup of the coherent streamwise vortices referred to as mode A and B shedding (Gerrard, 1978). As Re is further increased beyond 1,000, the formation distance begins to decrease with increasing Reynolds number, and two-dimensional Kelvin-Helmholtz instabilities begin forming in the shear layers (Braza et al., 1986).

The wake of the circular cylinder undergoes a critical transition when the Reynolds number reaches 200,000, which is when the wake turbulent transition point reaches the boundary layer on the circular cylinder (Williamson, 1996). This is characterized by a large decrease in both drag and wake size behind the cylinder due to the formation of a separation bubble when the turbulent separated flow reattaches to the cylinder surface. The wake size decreases due to a smaller portion of the cylinder experiencing separated flow, as shown in the schematic in figure 1-4. The drag decreases because the pressure recovers to a higher value upstream of the separation due to the increased amount of attached flow, as seen in figure 1-7(a). The flow then separates significantly further along the cylinder body than in the laminar separation case. At $Re > 1,000,000$ the entire boundary layer has become fully turbulent, resulting in the disappearance of the separation bubble, and the flow remains attached along the majority of the cylinder surface. Achenbach (1968) contains several nice schematics of the mean flow over a range of Reynolds numbers bounding this critical point at $Re = 200,000$, shown in figure 1-4, as well as pressure and skin friction measurements. The results presented in the current work span $150 < Re < 19,000$, and therefore encompass the majority of the von Kármán vortex shedding regimes.

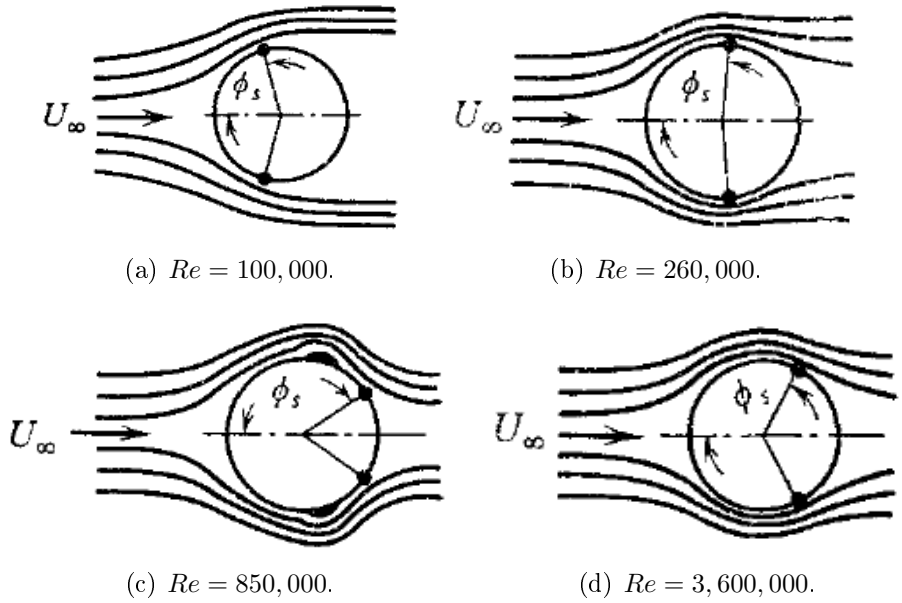

(a) $Re = 100,000$. (b) $Re = 260,000$.

(c) $Re = 850,000$. (d) $Re = 3,600,000$.

Figure 1-4: Flow schematics in the vicinity of the critical point from Achenbach (1968). The separation location is marked by ϕ_s.

The physical mechanism that causes the initial transition in the cylinder wake from a steady separation bubble to unsteady vortex shedding at $Re = 47$ has been analyzed and discussed thoroughly in the literature. Triantafyllou et al. (1986) found that an absolute instability in the near wake created a self-sustaining motion of fluid just behind the cylinder that allowed fluid to enter the separation bubble in an alternating periodic manner. This absolute instability determines the shedding frequency of the vortices by controlling the rate at which the fluid enters the separation bubble. Using experimentally-obtained instantaneous streamlines, it was found that the unsteady separation bubble was penetrated by fluid from alternating shear layers (Perry et al., 1982). Inside the separation bubble, vortex sheets underwent multiple folds that led to the vortex roll-up. Figure 1-5, from Perry et al. (1982), shows a sketch of the transition from a steady separation bubble to the oscillating separation bubble that leads to the formation of von Kármán vortices. The interaction between the two sides of the cylinder wake was further studied by placing a small "control" cylinder in the shear layer on one side of the wake (Strykowski and Sreenivasan, 1990). When the control cylinder was implemented at Reynolds numbers below 100, the shear layer interactions were inhibited in the wake

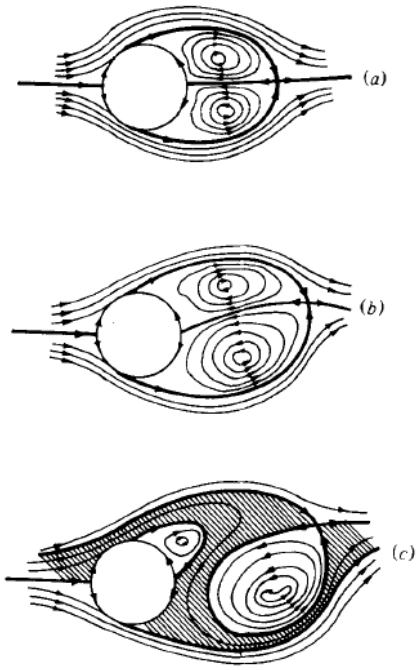

Figure 1-5: Streamlines in the wake of a circular cylinder showing the transition from the steady separation bubble to the unsteady separation bubble. Cross-hatch indicates an instantaneous alleyway of fluid. Adapted from Perry et al. (1982).

just downstream of the main cylinder, and the vortex shedding was effectively eliminated.

Researchers have also investigated what mechanism perpetuates the formation of the von Kármán vortices once the shedding is fully developed in the cylinder wake. The formation of these vortices behind a circular cylinder at Reynolds numbers below 350 is thought to be due to the presence of high shear near the downstream portion of the cylinder along with the induced velocity field caused by the momentum deficit (Griffin, 1995). As the vortex grows, its induced velocity begins to pull fluid from the opposing shear layer into the region between the forming vortex and the cylinder surface (Gerrard, 1966). A figure from Gerrard (1966) illustrating this concept is shown in figure 1-6. Since this fluid is from the opposite shear layer, it has oppositely-signed vorticity, and separates the vortex from the region of momentum deficit just behind the cylinder. Once the vortex begins to move downstream from the cylinder, it no longer has access to the strong shear that formed it, halting the increase in vortex strength that was present during formation. Many attempts to mitigate the vortex shedding focus on disrupting the transfer of vorticity from one side of the wake to the other, as shown by the use of

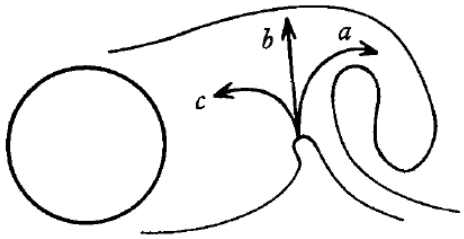

Figure 1-6: Filament-line sketch showing entrainment (a and b) and reverse flow (c) during vortex formation from Gerrard (1966).

splitter plates (Roshko, 1954), or by forcing the vortices to shed before they become large enough to entrain vorticity from the opposite shear layer (Jukes and Choi, 2009).

More recently, studies have focused on the stability analysis of the cylinder wake. A low-dimensional dynamical systems approach using an incompressible potential flow model of the cylinder wake found that when $Re < 47$, vorticity perturbations on the wake symmetry line decayed, but when $Re \geq 47$, vorticity perturbations located outside of the separation bubble on the symmetry line grew and caused oscillations in the separation bubble (Tang and Aubry, 1997). A numerical study investigating the wake oscillation at $Re > 47$ found that any small, localized vorticity disturbance propagated both up and downstream. When the disturbance reached the cylinder, it caused oscillation leading to the global instability (Takemoto and Mizushima, 2010). These two studies demonstrated that once the Reynolds number is above 47, any small perturbation in the flow field, regardless of its location, will cause the steady separation bubble to begin oscillating in an unsteady manner, leading to the formation of von Kármán vortices. Therefore, it is highly unlikely that the initial formation of the von Kármán vortices can be prevented as Re is increased above 47, but attempts have been made to suppress the vortices at a variety of Re using other methods.

1.1.2 Force and Pressure Measurements

The analysis of the unsteady forces acting on a circular cylinder in cross-flow is crucial for the design and control of hydrodynamic and aerodynamic structures (Blevins, 1977). The mean and fluctuating static pressure distribution on a circular cylinder over a range

of Reynolds numbers has been extensively investigated in the literature, and has yielded a large quantity of information on the influence that vortices have on bluff bodies. The fluctuating lift force is of particular interest since it is primarily induced by the von Kármán vortices (Norberg, 1986). A review by Norberg (2003) details numerous studies that investigated the fluctuating lift on a circular cylinder using pressure taps in various configurations. The distribution of the non-dimensional coefficient of pressure, C_p, is often used to compare the results obtained at different Re. C_p is defined as

$$C_p = \frac{p - p_\infty}{0.5\rho U_\infty^2}, \tag{1.3}$$

Where p is the static pressure on the cylinder surface, p_∞ is the freestream static pressure, ρ is the freestream density, and U_∞ is the freestream velocity. An example of various mean C_p distributions plotted versus the angular distance along the cylinder from the upstream stagnation point, θ, can be seen in figure 1-7(a). The mean C_p distribution is used to find the base pressure coefficient (mean C_p at $\theta = 180°$), the mean separation location, and the overall distribution of pressure on the cylinder surface. The mean separation location is found at the inflection point in the $\overline{C_p}$ distribution within the region of increasing $\overline{C_p}$ that occurs after it reaches its minimum (Zdravkovich, 1997). The time-dependent pressure distribution on the cylinder is often integrated to calculate the lift and drag forces, but other techniques to find the lift force without fully resolving the pressure distribution exist, and are discussed thoroughly in Norberg (2003). These include techniques such as cross-correlations between pressure taps at two arbitrary locations, and comparing the pressure values at $\theta = \pm 90$. Figure 1-7(b) displays the variation of the root mean square (r.m.s.) coefficient of lift for a range of Reynolds numbers. There is large variation in the r.m.s. lift coefficient with the highest fluctuating lift located around $Re = 250$ and between 20,000 and 200,000.

The location of the mean separation point is of particular interest in the current study, as the pressure signal just upstream of this location experiences the largest fluctuations due to the von Kármán vortices, and therefore is the location at which a pressure tap is generally placed if used for phase-averaging (Perrin et al., 2007). Nishimura and Taniike

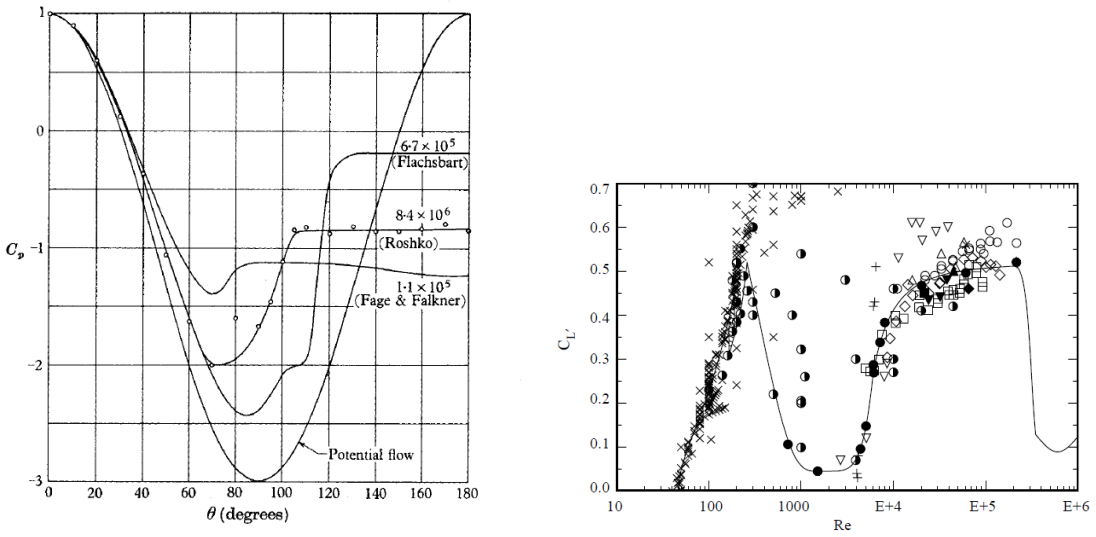

(a) C_p curves for various Re from Roshko (1961).

(b) R.m.s. lift coefficient vs. Reynolds number from Norberg (2003).

Figure 1-7: Pressure and r.m.s. lift coefficients with varying Re.

(2001) investigated the relationship between fluctuating lift and the stagnation and separation point locations. They found that the von Kármán vortices forming downstream of the cylinder affected the pressure distribution on the entire surface of the circular cylinder, even upstream of the separation point. They also found that the upstream stagnation point and the separation point move 180° out of phase from each other along the cylinder surface.

1.1.3 Control of von Kármán Vortex Shedding

Flow control techniques can be broadly classified as passive, open-loop active, or closed-loop active. Passive techniques generally rely on a permanent change in the geometry such as a surface pattern to change the flow physics. Open-loop active techniques either add or subtract momentum from the fluid in a prescribed manner, which can include continuous, periodic, or aperiodic application of the control system. Closed-loop active techniques add or subtract momentum from the fluid by an amount determined from an algorithm that uses sensors in the system, such as pressure transducers, for feedback. Multiple investigations have explored the control of bluff body vortex shedding with active

or passive flow control techniques, and a few representative publications are summarized here.

A passive attempt to affect the cylinder near-wake involved attaching longitudinally oriented o-rings to the cylinder (Lim and Lee, 2004). This study realized a drag reduction of 9% at $Re = 120,000$, which was attributed to the elongation of the vortex formation region. The addition of v-cut microgrooves aligned in the streamwise direction instead of o-rings on the cylinder surface created a 7.6% drag reduction at $Re = 3,600$, but a 4.2% drag increase at $Re = 36,000$ (Lee et al., 2005). An open-loop active technique used synthetic jets to create local separation bubbles on circular cylinders at Reynolds numbers of 500 and 3,900, and produced a reduction in drag coefficient of approximately 12% (Catalano et al., 2002). Alternatively, low power electro-hydrodynamic actuators were shown to affect the time-averaged separation location on the cylinder surface at $Re = 2,500$ when the flow was perturbed steadily, but at Reynolds numbers of the order of 50,000 they had a minimal effect (Artana et al., 2003). Changing the location of the separation point was shown to also affect the magnitude of the oscillating forces experienced by the cylinder. Another control method used dielectric barrier discharge plasma actuators to add momentum to the flow in the vicinity of the separation point on the cylinder surface in an open-loop pulsed manner (Jukes and Choi, 2009). This method achieved a drag reduction of 32% at $Re = 15,000$, but required 50 times more power than was saved. A combination of steady windward suction and steady leeward blowing was numerically shown to effectively eliminate the oscillatory forces on the cylinder at Reynolds numbers up to 1,000 (Dong et al., 2008). A closed-loop control scheme enabled increased mixing in the simulated flow around a square cylinder when wall-tangential velocity sensors were correlated with Lagrangian separation locations, and wall-tangential velocity actuators were driven to increase the shear layer interaction in the downstream wake (Wang et al., 2003). While several techniques have shown adequate control of the von Kármán vortex shedding at low Reynolds numbers, for Reynolds numbers encountered in practical applications, $\mathcal{O}(10^6)$, the current techniques require a prohibitive amount of power or lose their effectiveness. The research outlined in this dissertation seeks to obtain a new phenomenological representation of the shedding mechanism that contains flow physics

that are easier to manipulate than previous attempts.

1.2 Vortex Identification

Although studies on vortex dynamics have been carried out for over a hundred years, a widely-accepted, objective definition of a vortex and its boundaries remains an open question. Techniques used to define vortices are broken down into Eulerian and Lagrangian analyses. Eulerian vortex identification techniques use the instantaneous velocity field and its gradients to identify regions that contain vortices, while Lagrangian vortex identification techniques calculate scalar quantities based on particle trajectories using multiple velocity fields to determine which regions of the flow are dynamically distinct. A combination of Eulerian and Lagrangian techniques have been found to be useful when studying the cylinder near-wake and flow separation (Rockwood et al., 2016; Miron and Vétel, 2015; Miron et al., 2015).

1.2.1 Eulerian Techniques

Many Eulerian vortex criteria identify the coherent structures by a local swirling motion, which has the presence of closed or spiral streamlines or pathlines in a suitable reference frame. The Q criterion, developed by Hunt et al. (1988), identifies regions as vortices if the norm of the local rate of rotation tensor is dominant over the norm of the local rate of strain, and is discussed further in section 3.1.1. Several Eulerian criteria other than Q have been used in similar analyses previously, but do not yield distinctly dissimilar results, and for this work the Q criterion is chosen for simplicity and for consistency with similar studies in the literature. The Δ criterion proposed by Chong et al. (1990) defines vortices as regions where the velocity gradient has complex eigenvalues, which occurs in when there is are locally spiraling streamlines. The λ_2 criterion (Jeong and Hussain, 1995) defines vortices as regions where the second eigenvalue of $\boldsymbol{S}^2 + \boldsymbol{\Omega}^2$ is negative, where $\boldsymbol{S}$ is the symmetric rate of strain tensor, and $\boldsymbol{\Omega}$ is the anti-symmetric rate of rotation tensor. This condition guarantees a pressure minimum at the vortex core in three-dimensional flows. The swirl criterion proposed by Zhou et al. (1999) defines a vortex as regions

with a positive value of λ_{ci}^2 above a certain percentage of its global maximum. λ_{ci} is the imaginary component of the complex eigenvalue of the velocity gradient tensor. This criterion is a more stringent version of the Δ criterion mentioned above, that requires the imaginary eigenvalue to have a certain magnitude to be considered within a vortex. Graftieaux et al. (2001) defined a scalar function Γ_1 by using the topology of the velocity field to yield the center of the vortex core. Another common method of studying vortices involves the calculation of their circulation. Circulation is a spatially integrated scalar quantity that is a measure of the flux of vorticity through an area boundary, and can be used as a measure of the strength of the vortex. The implementation of circulation and Q in this work is explained in more detail in section 3.1. Some examples of studies comparing the different Eulerian vortex identification techniques can be found in Haller (2005); Dubief and Delcayre (2000), and Chakraborty et al. (2005).

A large body of past work has analyzed vortex structures using Eulerian criteria. Braza et al. (1986) developed an early simulation of the cylinder wake that studied the merging of the shear layer vortices at $Re = 1,000$ using vorticity and pressure contours, and determined that they form main eddies to the von Kármán vortex path. Perrin et al. (2006) analyzed turbulence statistics in the cylinder near wake, and used the rate of rotation tensor to determine vortex locations. Onoue and Breuer (2016) used swirl strength to identify the leading and trailing edge vortices shed from a pitching panel, and attributed changes to the leading edge vortex structure to changes in the plate pitch rate. Adrian et al. (2000) used swirl strength and Galilean transformations to visualize vortices in a shear layer where quantities like vorticity fail to accurately locate coherent vortices. Kriegseis et al. (2013) used vorticity contours to determine the location of the leading edge, trailing edge, and tip vortices for a pitching airfoil and found that the shear layer feeding velocity had a larger impact on the vortex characteristics than the more commonly used Reynolds number. Dabiri and Gharib (2004) used streamlines and vorticity in a frame of reference convecting with vortex rings to study their formation and entrainment. While these techniques can quickly identify regions of the flow that contain coherent structures, they generally require a suitable frame of reference and a carefully selected threshold, and therefore are not objective methods for detecting

coherent structures.

1.2.2 Lagrangian Techniques

Lagrangian vortex identification methods define a scalar field at a certain time by using the final locations of particle trajectories that have been initialized at the given time and integrated over a prescribed duration of time. One commonly used technique requires the calculation of the finite-time Lyapunov exponent (FTLE) field (Haller, 2001), which has proven to be a powerful tool for the purposes of identifying and tracking coherent structures in complex vortex-dominated fluid flows. This method has been used for both periodic (Green et al., 2011; Bourgeois et al., 2012; Kourentis and Konstantinidis, 2011; Miron and Vétel, 2015) and aperiodic (Beron-Vera et al., 2008; Blazevski and Haller, 2014; O'Farrell and Dabiri, 2014; Mulleners and Raffel, 2011; du Toit and Marsden, 2010) flow fields, and can be implemented using velocity field data from both numerical simulations and experiments if the proper spatial and temporal resolution of the data is available.

Ridges of high FTLE values locate transport boundaries which separate dynamically distinct regions of fluid whose material remains distinct over a certain length of time. The details of this technique are further discussed in section 3.1.3. Maximizing ridges of the scalar FTLE field have often been defined as Lagrangian coherent structure (LCS), as they are the simplest representation of attracting and repelling material surfaces that can be calculated from velocity data, but there are some shortcomings to using this technique to detect LCS as discussed by Allshouse and Peacock (2015). These shortcomings include the sensitivity of the FTLE calculation to the computational grid resolution, and the requirement of additional analysis to determine if the FTLE ridges identify shear or hyperbolic LCS. FTLE and LCS analyses have been applied to study unsteady wakes behind a pitching panel (Green et al., 2011), oceanic eddies (Beron-Vera et al., 2008), aortic valve jets (Shadden et al., 2010), fluid transport of translating and flapping wings (Eldredge and Chong, 2010), and hurricanes (du Toit and Marsden, 2010). As mentioned previously, FTLE analysis enabled increased mixing in simulated flow around a square cylinder when combined with a closed-loop control scheme (Wang et al., 2003). The

current study uses FTLE to gain additional understanding of the underlying flow physics in order to inform the future application of similar strategies to those used by Wang et al. (2003) to alter the shedding dynamics.

FTLE, like many Lagrangian methods, requires the evaluation of the Cauchy-Green strain tensor, which is constructed at each time from the gradient of the flow map across the domain of interest initialized at that time. The flow map is a one-to-one mapping of the initial material points to their final spatial locations over the time of interest. The calculation of the Cauchy-Green strain tensor requires adequate spatial and temporal resolution of velocity fields in order to ensure accurate particle trajectories (Allshouse and Peacock, 2015). The effect of the velocity field spatial resolution, noise, and smoothing on FTLE fields has been investigated by Olcay et al. (2010), who found that poor spatial resolution in the velocity field had a significant impact on the location of the FTLE ridges. Several studies have been conducted on the effect of the velocity field spatial and temporal resolution in ocean flows (Beron-Vera, 2010; Keating et al., 2011; Hernández-Carrasco et al., 2011; Poje et al., 2010), and found that flows with unresolved small scale energetic motion can have large errors in the FTLE field, and therefore should be used with caution. Keating et al. (2011) determined the temporal resolution needed at different velocity field spatial resolutions in order to ensure particle trajectories would not overshoot small scale structures.

Many techniques have been introduced that implement a variety of theories to ensure the accuracy of the FTLE ridges or LCS. The variational theory method proposed by Haller (2011) found an exact relationship between the LCS and the invariants of the Cauchy-Green strain tensor that allowed for LCS to be defined as the locally strongest attracting or repelling material surfaces. In an attempt to rectify errors in the flow map caused by the low number of trajectories common to oceanic flows, Allshouse and Thiffeault (2012) developed a method to detect coherent structures using a three-dimensional braid structure constructed from two-dimensional trajectories. This braid structure was then used to detect non-growing topological rings that enclosed invariant regions. Further investigation of these types of rings determined that in two-dimensional turbulent flows these coherent Lagrangian vortices can travel through the flow without being de-

stroyed (Haller and Beron-Vera, 2012, 2013). In real flows, such as large scale oceanic flows, these coherent vortices can persist over long periods of time and can collect surface material such as garbage or oil into a persistently concentrated region. This type of analysis has since been extended to three-dimensional unsteady flows in an investigation of hyperbolic and elliptic transport barriers (Blazevski and Haller, 2014). A new technique looking to increase the accuracy of the flow map calculation for experimental data used tracer particles from time-resolved particle image velocimetry (PIV) and particle-tracking velocimetry (PTV) to calculate many incremental flow maps that were then compiled together (Raben et al., 2014). While this increased the accuracy of the flow map, it still relied on having adequate spatial and temporal resolution as well as dimensional support for particle tracking.

Several techniques have been proposed that attempt to move away from using the Cauchy-Green strain tensor directly. One such method uses distinguished trajectories that can reveal both hyperbolic and non-hyperbolic flow regions in time-dependent flows (Rempel et al., 2013). These trajectories are used to find both the stable and unstable manifolds in the same calculation. The function "M" defined by these trajectories is less sensitive to integration time than the standard FTLE calculation and does not use the Cauchy-Green strain tensor, but still relies on accurate tracking of particle trajectories. The finite-size Lyapunov exponent (FSLE) has also been used to extract LCS, but in order to extract true LCS, the FSLE must meet a stringent set of requirements that increases the difficulty of the calculation (Karrasch and Haller, 2013). The calculation of the FSLE field also relies on accurate integration of particle trajectories, and relies on adequate spatial and temporal resolution (Hernández-Carrasco et al., 2011; Poje et al., 2010). A method proposed by Leung (2011) and Leung (2013) relies on partial differential equations and Eulerian data to predict the FTLE field instead of using particle trajectories and the Cauchy-Green strain tensor. While this method may eliminate the need for accurate particle trajectory information, it has yet to be implemented in flows that are not simple kinematic models. A method proposed by Froyland et al. (2010) uses probabilistic methods to study the evolution of probability densities to find the regions that remain coherent and relatively non-dispersive. Haller et al. (2016) conducted an

in-depth review of many of the currently utilized Lagrangian techniques for identifying vortices.

In this work we define a Lagrangian saddle as the intersection of the positive and negative-time FTLE ridges, which are discussed in detail in section 3.1.3. These Lagrangian saddles are critical points in the flow, and their locations have been shown to contain useful information about vortices and their behavior. In particular, the emergence of saddles was shown to accompany the birth of secondary hairpin vortices in a turbulent channel direct numerical simulation (Green et al., 2010). Also, in an FTLE analysis of two-component PIV data in the wake of a low aspect ratio trapezoidal pitching panel, the wake breakdown was observed to occur at the streamwise location where two independent Lagrangian saddles merged (Green et al., 2011). The location of the Lagrangian saddles has been found to contain information about vortices shed from pitching plates (Huang and Green, 2015), pitching airfoils (Mulleners and Raffel, 2012), and circular cylinders (Rockwood et al., 2016). Previous FTLE results have been presented for the flow around a circular cylinder for both experimental and numerical data (Rockwood et al., 2014; Rockwood and Green, 2015, 2016; Kourentis and Konstantinidis, 2011; Lei et al., 2015; Miron and Vétel, 2015).

1.3 Motivation

While a large body of research has been dedicated to understanding, detecting, and controlling the von Kármán vortices shed from bluff bodies, there is still no objective method to define the shedding time of a vortex, or to relate this information to real-time sensors that could be used to inform closed-loop flow control. The goal of the research presented in this dissertation is to objectively identify and track the behavior of the von Kármán vortices shedding from a circular cylinder, and to relate this information to a sensor on the cylinder surface that could be used in real-time to inform closed-loop flow control on whether the vortex is forming, shedding, or separated from the cylinder. Previous attempts in the literature to determine the coherent structures, or vortices, in the wake of bluff bodies primarily used Eulerian techniques which require a subjective

threshold to determine the vortex locations.

As part of this work, it was found that the locations of Lagrangian saddles could be used to determine the behavior of von Kármán vortices in the near-wake region for numerical data at $Re = 100$ (Rockwood et al., 2016). The speed at which these saddles moved away from the cylinder changes dramatically between the forming, shedding, and convecting portions of the vortex shedding process, and provided a clear method for identifying the time of vortex shedding. While this result was helpful for determining whether a vortex was forming or shedding in the wake of bluff bodies, it does not lend itself to direct implementation in flow control applications as the FTLE ridges require extensive computational time and future information to calculate. In the research presented here, Lagrangian flow structures are related to the static pressure on the cylinder surface, a quantity that is easily and cheaply measurable with pressure transducers.

The static pressure distribution on the cylinder surface can be measured in real-time, enabling it to be used as an input for a closed-loop flow control algorithm. By investigating the changes in the cylinder static pressure distribution as the Lagrangian saddle accelerates away from the cylinder, pressure fluctuations in specific regions are compared with the Lagrangian saddle lift-off time. In this way, relating the Lagrangian saddle location to a quantity that is measurable in real-time allows phenomenological changes of the flow topology to be determined on the fly. The flow field could then be specifically manipulated with surface flow control techniques in a real-time closed-loop control system.

The wake behind a circular cylinder was visualized using Eulerian and Lagrangian techniques, and the Lagrangian saddles were tracked for two-dimensional numerical data at $Re = 150$, three-dimensional numerical data at $Re = 400$, and two-dimensional experimental data at $Re = 9,000$ and $Re = 19,000$. The force history was compared to the vortex shedding time for the two-dimensional numerical data at $Re = 150$, and the three-dimensional numerical data at $Re = 400$. The static pressure distribution on the cylinder surface was linked to the vortex shedding time for the two-dimensional numerical data at $Re = 150$, the three-dimensional numerical data at $Re = 400$, and the two-dimensional experimental data at $Re = 19,000$.

Chapter 2

Setup

This chapter contains details on the experimental setup, test conditions, and equipment used. It also provides information on the numerical simulations that were used to generate the velocity fields in the two numerical cases presented.

2.1 Water Tunnel

Two experimental investigations were conducted at the Syracuse University Flow Visualization Laboratory located at the Syracuse Center of Excellence. An ELD 505-24" closed-loop water tunnel with a 2560 gallon volume was used to conduct experiments including particle image velocimetry (PIV), static pressure measurements, and flow visualization. The 2.4 m long test section has a square-cross section with a width of 0.61 m. The tunnel was designed to be run with acrylic covers placed on the top surface of the test section, fully enclosing the tunnel. Due to apparatus constraints, the experiments were run without the covers to allow for physical access to the top surface of the tunnel. A 30 hp motor was used to drive the water tunnel at speeds from 40 mm/s to 1 m/s.

Figure 2-1: Experimental system for the $Re = 9,000$ case.

2.2 Model Configuration

2.2.1 $Re = 9,000$ Cylinder

In the $Re = 9,000$ experimental case, PIV velocity fields were collected simultaneously with static pressure at a location 70° from the upstream stagnation point. A vertically-aligned rigid PVC circular cylinder with an outside diameter of 60 mm and a wall thickness of 3.9 mm was used. This resulted in a blockage of 0.01, which has a minimal effect on the von Kármán vortex shedding (Zdravkovich, 1997). The cylinder was fixed above the test section water height with a vibration-damping u-bolt, and placed flush against the bottom of the test section. A thin ring of duct tape was applied along the bottom of the cylinder to decrease the risk of the cylinder scratching the test section. The aspect ratio, or ratio between the submerged span and diameter of the cylinder, was 10. A static pressure tap with an inside diameter of 2.5 mm was located 70° from the upstream stagnation point, at a location halfway along the submerged span of the cylinder. The pressure tap location slightly upstream of the expected separation point was chosen to ensure the signal was dominated by the von Kármán vortices (Perrin et al., 2007). This pressure signal was used for phase-averaging. 6.8 m of flexible Masterkleer PVC tubing with an inner diameter of 2.5 mm ran from the pressure tap to an Omega PX409-10WDDU10V wet-dry differential pressure transducer located outside of the test section. Figure 2-1 shows the cylinder, the associated tubing, and the u-bolt.

2.2.2 $Re = 19,000$ Cylinder

In the $Re = 19,000$ experimental case, PIV velocity fields were collected simultaneously with the static pressure distribution at one spanwise plane, and the static pressure at a location 70° from the upstream stagnation point. A vertically aligned two-piece aluminum 6061 circular cylinder with an outside diameter of 89 mm and a wall thickness of 6.4 mm was used. This resulted in a blockage of 0.146. The top 0.3 m of the cylinder was out of the water, and was inserted into a polycarbonate sleeve with a slip fit to allow the cylinder to rotate when needed without changing its location in the tunnel. The sleeve was fixed in two locations with vibration-damping u-bolts to ensure there was no movement of the cylinder during testing. Figure 2-2 contains two images showing the experimental setup for this case. The top section of the cylinder contained a circumferential ring of 5 pressure taps, each with a 1.9 mm diameter, located 25.4 mm above the cut between the two sections of the cylinder. These taps were placed in 45° increments from 0° to 180°. The bottom section of the cylinder contained one pressure tap with a 1.9 mm diameter, located 25.4 mm below the cut between the two cylinder sections, and 50.8 mm below the circumferential ring of pressure taps. The two portions of the cylinder were precision machined to slide together tightly while still allowing one section to rotate independent of the other. A thin coating of petroleum jelly was applied to the contact surface between the two sections of the cylinder before each test to keep them from binding together. The bottom portion of the cylinder was attached to the test section floor with a suction cup to keep its location fixed. A Tuohy-Borst adapter was affixed into each pressure tap with two part epoxy, and sanded to be flush to the cylinder outer diameter. An ADInstruments SPR-524 pressure transducer was inserted into each adapter during data collection. The adapters were then sealed, keeping any fluid from escaping the pressure measurement region into the interior of the cylinder. Figure 2-3 displays an image of the transducer and the adapter. The cylinder aspect ratio was 6.7, which is significantly lower than the aspect of ratio of 10 used in the other experimental setup. Szepessy and Bearman (1992) showed that if $Re = \mathcal{O}(10^4)$, there are minimal changes in the fluctuating lift and shedding frequency even when aspect ratio is decreased to 1. At $Re = \mathcal{O}(10^5)$, aspect

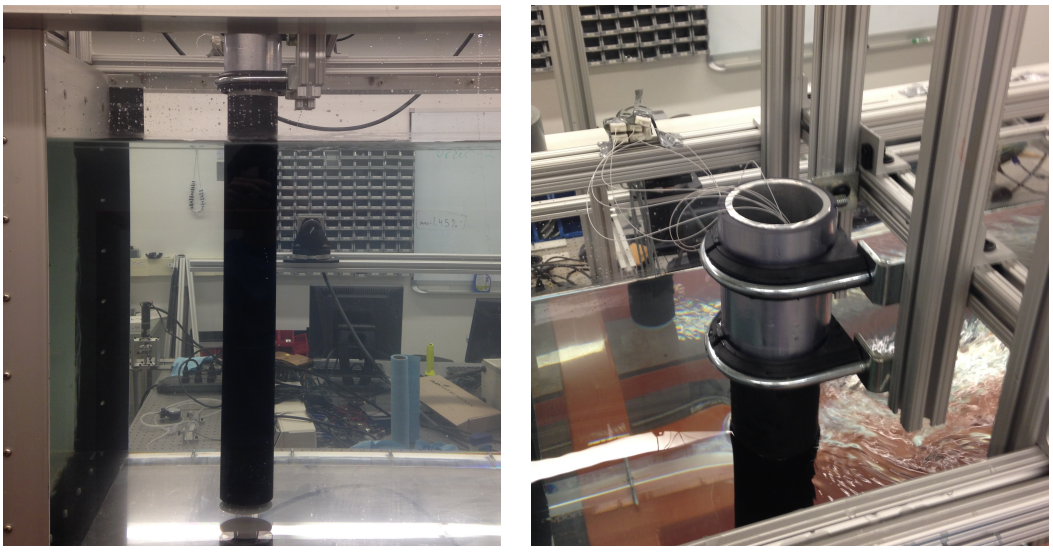

(a) Cylinder in test configuration. (b) Cylinder mounting apparatus.

Figure 2-2: Experimental system for the $Re = 19,000$ case.

ratio begins to have a larger effect. The cylinder was sandblasted with #20 grit glass beads, and then painted with a Krylon ultra-flat black paint to minimize laser reflections. The cylinder was changed from PVC ($Re = 9,000$ case) to aluminum 6061 to allow for precision machining of the joined section and multiple pressure taps, create a uniform surface roughness, and for a decrease in the likelihood of irreversible dents on the outer surface. The diameter was increased between cases so the Tuohy-Borst adapters could fit on the interior of the cylinder, and to increase the magnitude of the pressure fluctuations.

2.3 Measurement and Data Acquisition Systems

2.3.1 PXIe

A National Instruments PXIe system was used to sample the pressure signals and record the timing of the PIV snapshots. A PXIe-1078 chassis housed the PXIe-6363 multifunction DAQ card that was connected to a terminal block for voltage measurements. The PXIe-6363 has 32 analog inputs that can be sampled up to 1 megasamples per second when using multiple channels with 16-bit resolution. The PXIe system was run using a

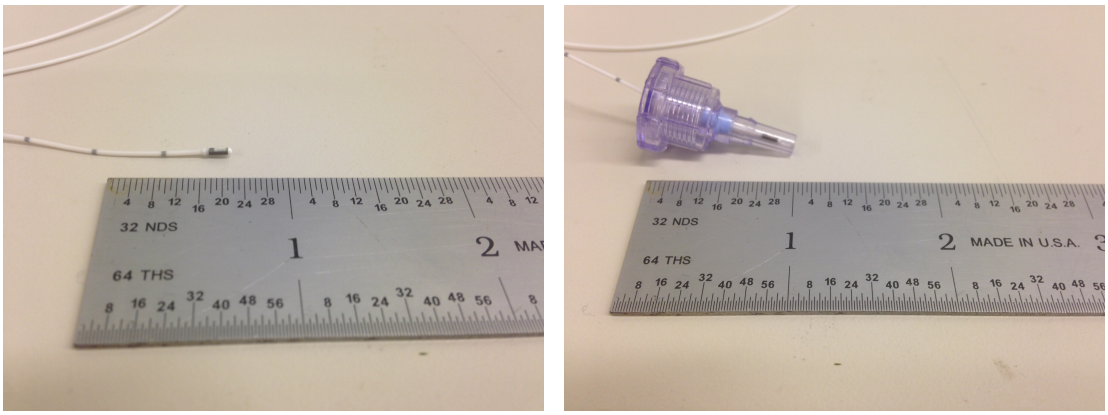

(a) SPR-524 pressure transducer. (b) SPR-524 inside of a Tuohy-Borst adapter.

Figure 2-3: $Re = 19,000$ pressure transducer.

Real-Time LabVIEW environment operating on a standalone PC.

2.3.2 Pressure Systems

***Re* = 9,000**

An Omega PX409-10WDDU10V wet-dry differential pressure transducer was used to acquire static pressure measurements on the circular cylinder. Voltage data was collected at 3 kHz by the PXIe system detailed above, with a sensitivity of 3.9 mV/Pa. The transducer was calibrated using a twelve-point calibration, where the height of the pressure transducer relative to the water surface level was varied using a manual traverse. Calibration was run before ('pre' case) and after ('post' case) each set of testing, generally separated by about 11 hours. The intrinsic polyfit command in Matlab was used to determine the linear relationship between voltage and pressure using a least-squares fit, and sample before and after calibration curves are shown in figure 2-4. The sensitivity varied by 0.1% from 'pre' to 'post' in the $Re = 9,000$ case shown, and the voltage bias varied by 12%.

***Re* = 19,000**

An ADInstruments SPR-524 pressure transducer was used with an ADInstruments PCU-2000 signal conditioner, which output a voltage that was sampled at 2 kHz by the PXIe system detailed above. The sensitivity of the system was 0.08 mV/Pa. The SPR-524 sys-

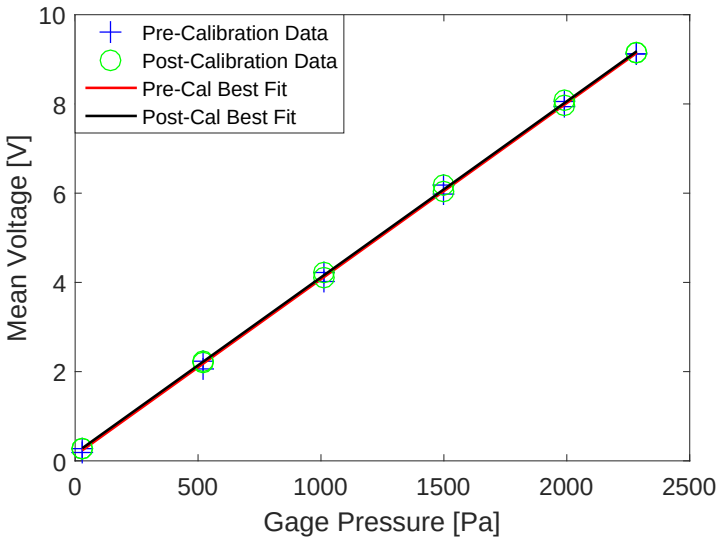

Figure 2-4: Pressure calibration curve for the Omega PX409-10WDDU10V transducer used in the $Re = 9,000$ case.

tem contains a small pressure sensor on the end of a 1.2 mm diameter straight catheter, with a submersible distance of 100 cm. This system is more commonly used to measure pressures for cardiovascular flows in rabbits. The ADInstruments system was implemented in favor of the Omega transducer detailed above to avoid the large amount of tubing that can reduce the dynamic response of pressure measurements. The small size of the SPR-524 allowed the pressure transducer to be inserted to within a couple of millimeters from the outside surface of the cylinder in the pressure taps, but the decrease in sensitivity required an increase in Re in order to allow for large enough pressure fluctuations for accurate phase-averaging. Each of the six transducers were calibrated using a three-point calibration procedure before and after all of the experimental data was collected. This procedure used a syringe to manually adjust the air pressure to each transducer individually, and an analog pressure sensor was used to determine the pressures. The calibration required the transducers to be removed from the cylinder, so this calibration could not be done once the cylinder was placed in the water tunnel. Due to concerns about maintaining an exact cylinder location between runs, the $Re = 19,000$ cylinder was not removed from the tunnel in between test cases, which meant the calibration could only be carried out before and after all of the experimental data was collected. The total time between the two calibrations was 36 hours. The intrinsic polyfit command

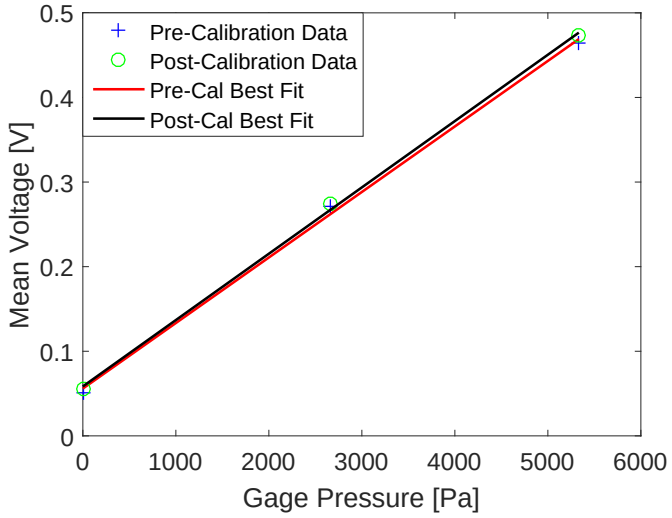

Figure 2-5: Pressure calibration curve for the ADInstruments SPR-524 transducer used in the $Re = 19,000$ case, phase-averaging channel.

in Matlab was used to determine the linear relationship between voltage and pressure using a least-squares fit, and the before and after calibration curves for channel 6, which was the channel used for phase-averaging, is shown in figure 2-5. The variation in sensitivity and voltage bias across all channels between the 'pre' and 'post' calibrations is shown in table 2.1.

Channel	Sensitivity Variation	Voltage Bias Variation
1	-1.5%	-21%
2	-4.8%	-16%
3	-4.4%	-16%
4	-4.6%	2.7%
5	-3.0%	-1.4%
6	-1.2%	-4.5%
Mean	-3.3%	-9.4%
Standard Deviation	1.5%	9.6%

Table 2.1: Change in sensitivity and voltage bias from from pre-calibration to post-calibration for the six ADInstruments SPR-524 transducers used in the $Re = 19,000$ case.

2.3.3 Particle Image Velocimetry System

Particle image velocimetry (PIV) uses image cross-correlations to determine the movement of illuminated particles between two images separated by a prescribed amount of time. The change in distance is calculated in small portions of the domain, called interrogation areas. The change in distance in each interrogation area, determined by the cross-correlation peak, is divided by the time between each image to determine the velocity vector for that interrogation area. The full area or volume of interest is generally illuminated by one or more lasers, and the particle size, material, and coating vary depending on application. In water, plastic or hollow glass spheres are commonly used. Both experimental setups used Dantec Dynamics DynamicStudio software, and were calibrated using a Dantec two-dimensional calibration plate 200 mm $\times$ 200 mm in size. The plate contained solid dots with a 5 mm constant spacing. The pixel (px) to mm ratio was determined by measuring the scale factor across the calibration plate. The DynamicStudio adaptive correlation analysis technique was used to calculate the velocity vectors using the single-image/dual-frame technique. This technique used 64×64 px initial interrogation areas, and the results from this initial calculation were then used to inform the final interrogation windows, which were 16×16 px. The interrogation window offset was determined using central differencing, and spurious vectors were identified if they exceeded an acceptance factor of 0.1, which were then replaced using a 3×3 px moving average with 3 iterations. The acceptance factor is a measure of how large a velocity gradient is allowed in the neighborhood of each vector. An estimation of the error in the PIV velocity vector calculations in shown in Appendix A.

***Re* = 9,000**

To measure the flow field around the smaller diameter PVC cylinder at $Re = 9,000$, Dantec polyamid particles with a diameter of 20.0 µm were used to seed the flow, and two Gemini Nd-Yag 200-15 laser at 532 nm were used to illuminate the flow in a single spanwise-constant plane aligned with the pressure tap. Two 1.3 megapixel HiSense PIV cameras were used to capture image pairs at a rate of 4 Hz. Each camera had a measurement window of 1280×1024 px with a spatial resolution of 4.8 px/mm, which provided a

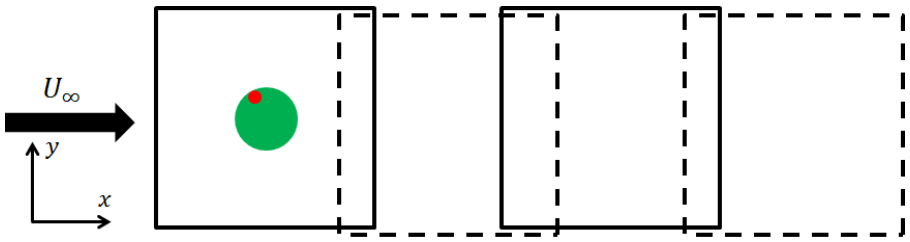

Figure 2-6: Location of cylinder (green), pressure tap (red), PIV camera one (solid black box), and PIV camera two (dashed black box) for $Re = 9,000$ experimental setup as viewed from above the water tunnel.

field of view of approximately 267×213 mm. A final interrogation window size of 16×16 px was selected in DynamicStudio with an overlap of 50%, resulting in a 160×128 vector field. This yielded a grid spacing of 8 px or 1.7 mm, which is about $0.03D$. 3000 image pairs were captured by the two cameras simultaneously with a streamwise overlap of 37%, and the resulting instantaneous velocity vector fields were stitched together by bilinearly interpolating onto a common grid within both domains. The cameras were then moved to a location downstream of the cylinder to increase the total field of view with a 5% overlap in the streamwise direction, and the process was repeated. A schematic of the data domain is shown in figure 2-6. The stitched velocity fields at each downstream location were phase-averaged into 18 phases per period using two different methods to increase the temporal resolution of the data for the Lagrangian calculations. The phase-averaging methods are described in detail in section 3.3. The phase-averaged results were then stitched together using bilinear interpolation which resulted in a full field of view of 396×198 mm, or $(x/D, y/D) \in [-2, 4.6] \times [-1.5, 1.8]$, with 265×133 vectors.

$Re = 19,000$

To measure the flow field around the larger diameter aluminum cylinder at $Re = 19,000$, Potter Industries particles with a mean diameter of 11.7 μm were used to seed the flow, and a Quantel Evergreen EVG00200 laser at 532 nm was used to illuminate the flow in a single spanwise-constant plane aligned with the circumferential array of pressure taps. A mirror was used to reflect the laser sheet into the shadow cast by the cylinder. Two 1.3 megapixel HiSense PIV cameras were used to capture image pairs at a rate of 4 Hz. Each camera had a measurement window of 1280×1024 px with a spatial resolution

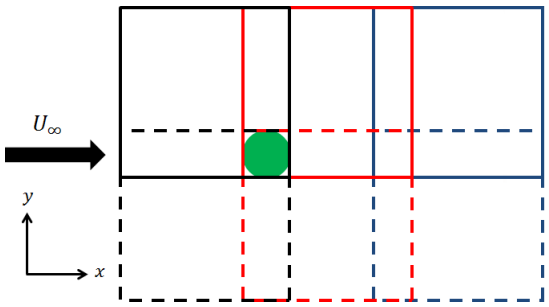

Figure 2-7: Location of cylinder (green), PIV camera one (solid boxes), and PIV camera two (dashed boxes) for $Re = 19,000$ experimental setup as viewed from above the water tunnel.

of 4.9 px/mm, which provided a field of view of approximately 262×209 mm. A final interrogation window size of 16×16 px was selected in DynamicStudio with an overlap of 50%, resulting in a 159×127 vector field. This yielded a grid spacing of 8 px or 1.6 mm, which is about $0.02D$. 3300 image pairs were captured by the two cameras simultaneously with an 11% overlap in the transverse direction, and the mean brightness field for each camera was subtracted from each respective image to increase the signal to noise ratio. The resulting instantaneous velocity vector fields were stitched together by bilinearly interpolating onto a common grid within both domains. The cameras were moved to two different locations downstream using a Dantec 9041T031 one-dimensional traverse, each with a 13% overlap in the streamwise direction. The camera locations are shown in figure 2-7. The stitched velocity fields were then phase-averaged into 24 phases per period using the a static pressure tap that was kept at a location 70° from the upstream stagnation point. More phases were used in this case compared to the $Re = 9,000$ case to increase the temporal resolution of the final results. The number of PIV snapshots taken was increased to ensure each phase-averaged velocity field converged. The three phase-averaged windows of data were then stitched together using bilinear interpolation, resulting in a final field of view of 577×354 mm, or $(x/D, y/D) \in [-1.9, 4.6] \times [-2.0, 2.0]$, with 413×254 vectors.

2.4 Test Conditions

Data at multiple Re was collected for each experimental case presented in this dissertation. For both cases, the static pressure was measured for a duration encompassing each PIV run.

$Re = 9,000$

The $Re = 9,000$ setup was run at freestream velocities corresponding to Reynolds numbers of 5,000 to 10,000 in increments of 1,000. Cases with $Re < 9,000$ did not have strong enough fluctuations in pressure to allow for accurate phase-averaging, so $Re = 9,000$ was chosen as the case presented in this dissertation. The $Re = 10,000$ case was also valid, but was nearly identical to the $Re = 9,000$ data, so it is not shown for brevity. Samples results are shown in Appendix C for comparison. The experimental setup for this case utilized a camera centered below the circular cylinder. The bottom of the cylinder blocked a small circular portion of the field of view of the camera since the PIV object plane was further away than the bottom of the cylinder, resulting in a ring of no velocity data around the cylinder. This restricted the near-cylinder FTLE calculation for this data (far case), so another supplemental set of data (near case) was collected with cameras slightly offset from the cylinder to allow for the resolution of the near-cylinder region. This supplemental dataset only used one laser, so a shadow existed on one side of the cylinder, and no velocity information was acquired in that region. The FTLE field was calculated for each dataset independent of the other, and the datasets were not stitched together between the separate experiments. Results from these datasets are shown in figure 4-6.

$Re = 19,000$

The $Re = 19,000$ setup was run at freestream velocities corresponding to Reynolds numbers of 13,000 to 22,000 in increments of 3,000. Cases with $Re < 19,000$ had smaller pressure fluctuations, which increased the likelihood of errors in the phase angle found from the phase-averaging algorithm. The $Re = 22,000$ case caused the water tunnel impeller to scrape the return pipe at times, so it was not considered. At each Re, the cylinder section containing the circumferential pressure taps was rotated twice in 15°

increments to increase the angular resolution of the pressure measurements from 45° to 15° spanning a range from 0° to 210° from the upstream stagnation point.

2.5 Freestream Quality

Freestream two-component PIV data was collected at each experimental Reynolds number to determine the mean and standard deviation of the velocity components, and the turbulence intensity. Turbulence intensity was calculated as:

$$I = \frac{\sqrt{\frac{1}{3}\left(u_x'^2 + u_y'^2 + u_z'^2\right)}}{\sqrt{U_x^2 + U_y^2 + U_z^2}} \tag{2.1}$$

where $u_x'^2$ is the r.m.s. of the x-component (streamwise) of the fluctuating velocity, and U_x is the x-component of the mean flow. Y-component (transverse in experiments) values were not measured, but were assumed to be equivalent to the measured z-component (spanwise) values. The results are shown in table 2.2. The turbulence intensity was high in the $Re = 9,000$ case, which causes the pressure to decrease around a large portion of the cylinder. As turbulence intensity increases, the flow tends to stay attached to the cylinder, resulting in a higher mean separation angle (Batham, 1973). In the time between the $Re = 9,000$ and $Re = 19,000$ experiments, blemishes on the interior surface of the water tunnel were repaired, which likely helped reduce the turbulence intensity. The upstream screens that generate small scales of turbulence were cleaned more frequently in the $Re = 19,000$ case during data collection, which likely contributed to the smaller turbulence intensity as well.

Approximate Re	$\boldsymbol{U}$ [mm/s]	$\boldsymbol{\sigma}$ [mm/s]	I	Exact Re
9,000	(151,0.2,0.2)	(2.52,0.52,0.52)	11%	9,069
19,000	(218,0.8,0.8)	(0.76,0.22,0.22)	2.3%	19,303

Table 2.2: Freestream quality information.

2.6 Numerical Simulations

Circular cylinder flow velocity and surface static pressure data were generated by two numerical simulations run by collaborators at Florida State University. A two-dimensional simulation was run at $Re = 150$, and a three-dimensional simulation was run at $Re = 400$.

2.6.1 Two-dimensional Simulation at $Re = 150$

Data from a simulation generated by Robert Reger, advised by Drs. Taira and Cattafesta, used the CharLES solver developed by Cascade Technologies to simulate the flow in the cylinder near-wake and near the surface (Khalighi, Nichols, Lele, Ham and Moin, 2011). CharLES employs a second order finite volume method in space and a third order Runge-Kutta scheme in time. The coefficients of pressure, lift, and drag matched well with a similar simulation conducted by Inoue and Hatakeyama (2002). The code used an r, θ O-grid mesh with a constant $\Delta\theta = 0.725°$ and an increasing $\Delta r/D$ from 0.005 to 0.6 as the distance from the cylinder increased. The domain extended 200 diameters in the radial direction, and the velocity data generated on this grid was interpolated onto a uniform x, y grid using bicubic interpolation with a coordinate transformation developed by Zingg and Yarrow (1989) to simplify the FTLE particle integration. Bicubic interpolation requires the value and derivatives of velocity (or other function of interest) to be known at each grid point surrounding the location of interest. Bicubic interpolation preserves the derivative information, resulting in a smoothly varying function in space. The data had a temporal resolution of 55 velocity files for each von Kármán vortex shedding period.

2.6.2 Three-dimensional Simulation at $Re = 400$

A three-dimensional direct numerical simulation (DNS) was performed by Yiyang Sun, advised by Dr. Taira, for a spanwise-periodic circular cylinder flow at $Re = 400$ using the high-fidelity incompressible flow solver, Cliff (CharLES software package) (Khalighi, Nichols, Lele, Ham and Moin, 2011; Khalighi, Ham, Moin, Lele and Schlinker, 2011; Bres et al., 2012). The solver uses a finite-volume method to solve the Navier–Stokes equations on structured or unstructured grids with second-order spatial and temporal schemes. The

simulation utilized an unstructured grid which was refined around the cylinder surface and wake region. The total number of grid points was approximately 16 million with an overall computational domain size of $(x/D, y/D, z/D) \in [-10, 30] \times [-15, 15] \times [0, 2\pi]$. At the inlet, uniform flow with free-stream velocity $\mathbf{v}/U_\infty = (1, 0, 0)$ was prescribed. At the outlet, a convective outflow condition was specified to allow wake structures to leave without disturbing the near-field flows. The slip condition was applied on the remaining far-field boundaries. The velocity data generated by this simulation was interpolated onto a uniform x, y, z grid using two different techniques to simplify the FTLE particle integration. The structured brick grid in the near cylinder region was interpolated using bicubic interpolation with a coordinate transformation (Zingg and Yarrow, 1989). The unstructured triangular prism grid in the wake region was interpolated using barycentric interpolation. Barycentric interpolation determines the function value at a point on the interior of a triangle by determining the weighting of the function values at the vertices using area coordinates. The data has a temporal resolution of 25 velocity files per period.

Chapter 3

Analysis Techniques

This chapter details the techniques used to visualize the vortex cores, track their movement, analyze the acquired pressure signals, phase-average the velocity fields collected using PIV, and study the errors related to using two-dimensional PIV for Lagrangian calculations in a three-dimensional flow field.

3.1 Wake Visualization Techniques

The circular cylinder wake was visualized using both the Eulerian Q criterion and the Lagrangian finite-time Lyapunov exponent (FTLE). These quantities were calculated using the numerically and experimentally-obtained velocity fields. Calculating Q was computationally cheap, and simple to implement. The FTLE calculation was more complex and computationally expensive than Q, but yielded quantative results that provided a distinctly different perspective of the flow physics.

3.1.1 Eulerian Q criterion

The Eulerian criterion employed to visualize the vortex cores was the Q criterion proposed by Hunt et al. (1988). The velocity gradient tensor, $\nabla \boldsymbol{u}$, can be decomposed into the symmetric rate of strain tensor, $\boldsymbol{S}$, and the anti-symmetric rate of rotation tensor, $\boldsymbol{\Omega}$:

$$\nabla \boldsymbol{u} = \boldsymbol{S} + \boldsymbol{\Omega}, \tag{3.1}$$

where $\boldsymbol{S} = \frac{1}{2}[\nabla \boldsymbol{u} + (\nabla \boldsymbol{u})^T]$ and $\boldsymbol{\Omega} = \frac{1}{2}[\nabla \boldsymbol{u} - (\nabla \boldsymbol{u})^T]$. The Q criterion is defined as the difference between the magnitudes of the rate of rotation and rate of strain tensors as shown in equation 3.2.

$$Q = \frac{1}{2}[||\boldsymbol{\Omega}||^2 - ||\boldsymbol{S}||^2], \tag{3.2}$$

where $||\cdot||$ represents the Euclidean or Frobenius norm. Positive Q values describe vortices as regions where the norm of the rate of rotation tensor is dominant over the norm of the rate of strain tensor, and Q is the second invariant of the velocity gradient tensor.

The Q criterion has several shortcomings as reviewed by Haller (2005). While the Q criterion is Galilean invariant, or unaffected by translations of the frame of reference, it can lead to misrepresentation of vortices when rotating or accelerating frames of reference are used. This criterion can find vortex cores effectively, but a subjective threshold, such as a percentage of the maximum value, is often defined as the boundary of the vortex in practical implementation. In flows with low levels of turbulence or noise, an appropriate threshold is often simple to determine, but becomes more difficult to determine in complex flows, especially in three-dimensional turbulence. When noise is present in the velocity field, the spatial gradients used to calculate the Q criterion magnify the errors caused by the noise significantly, resulting in inherently noisy Q results for experimental datasets. Table 3.1 contains the plotting thresholds for Q for each set of results, and figure 3-1 displays how the wake visualization changes with varying Q thresholds. When $Q = 0$ is used (figure 3-1(a)) the data is noisy, especially in the vicinity of the vortex farthest downstream in the domain. While the general locations of the vortices and shear layer can be seen, it is difficult to determine where the edges of the vortices are. When 1% or 3% of Q_{max} is used (figures 3-1(b) and 3-1(c)), the noise is reduced, and the von Kármán vortices can be seen more clearly. If the threshold is set higher, for example 5% of Q_{max} (figure 3-1(d)), the shear layer begins to appear broken in the region between the shedding vortex and the top surface of the cylinder, at the location marked with a black arrow. This is an example of how the chosen Q threshold can affect the interpretation of results. 1% of Q_{max} was chosen in the experimental cases to remove a small amount

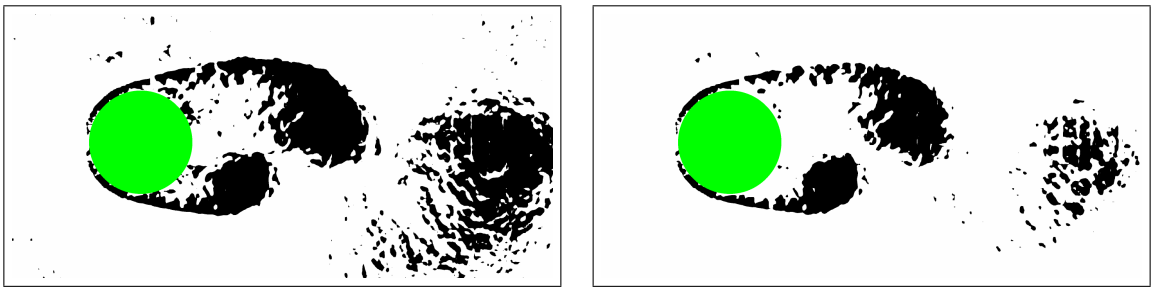

(a) $Re = 19,000$ wake at $t/T = 0.73$ with $Q_{min} = 0$.

(b) $Re = 19,000$ wake at $t/T = 0.73$ with $Q_{min} = 0.01Q_{max}$.

(c) $Re = 19,000$ wake at $t/T = 0.73$ with $Q_{min} = 0.03Q_{max}$.

(d) $Re = 19,000$ wake at $t/T = 0.73$ with $Q_{min} = 0.05Q_{max}$.

Figure 3-1: Variation in Q minimum contour for $Re = 19,000$. All values above the specified contour are colored black.

of the noise generated from inaccuracies in the PIV velocity field, while still retaining as much of the Q field as possible.

Re	Q Threshold
150	$Q = 0$
400	$Q = 0$
9,000	$0.01Q_{max}$
19,000	$0.01Q_{max}$

Table 3.1: Minimum Q thresholds for plotting.

3.1.2 Circulation

Circulation was used as a metric of vortex strength by measuring the vorticity flux into a prescribed area defined by the boundaries of the vortex. In the case of a circular cylinder, the vorticity flux is caused by the transport of vorticity generated in the shear

layer along the cylinder surface into the forming vortex. Circulation is defined, utilizing Stoke's theorem, as:

$$-\Gamma = \oint_{\partial A} \boldsymbol{u} \cdot d\boldsymbol{s} = \iint_{A} \boldsymbol{\omega} \cdot d\boldsymbol{A}, \tag{3.3}$$

where ∂A is the boundary of area A, $\boldsymbol{u}$ is the velocity field, $\boldsymbol{\omega}$ is the vorticity, $d\boldsymbol{s}$ is aligned tangent to an infinitesimal portion of the boundary, and $d\boldsymbol{A}$ is the normal vector to an infinitesimal portion of the area. When calculating circulation, especially when comparing values over time, special care must be taken to consider the circulation inside a consistently defined area. There is no clear definition of the boundary that should used to determine the correct area for all circulation calculations. This is further complicated if a shear layer is feeding the vortex, as the boundary between the vortex and the shear layer is unclear and often defined in a subjective or application-specific manner. Generally, a bounding box is drawn large enough to encompass the entire vortex while still eliminating as much of any nearby, but distinct, regions of vorticity as possible, such as a feeding shear layer (Ringuette et al., 2007).

3.1.3 Lagrangian Finite-time Lyapunov Exponent

The finite-time Lyapunov exponent was initially introduced by Haller (2001), where he extracted Lagrangian coherent structures as maximizing ridges of the scalar finite-time Lyapunov exponent (FTLE) field. The FTLE calculation is initialized by computationally creating a fine grid of particle trajectories in the domain at the time of interest, t_0. Particle trajectories are then advected in time using a fourth-order Runge-Kutta integrator until the integration time, τ, is reached. With $(\boldsymbol{x}_0, t_0)$ representing the trajectory initial location and time, and $\boldsymbol{x}(t_0+\tau, \boldsymbol{x}_0, t_0)$ representing the trajectory final location at time, $t_0+\tau$, the coefficient of expansion, σ_τ, is defined as:

$$\sigma_\tau(\boldsymbol{x}_0, t_0) = \lambda_{max}\left(\left[\frac{\partial \boldsymbol{x}(t_0+\tau, \boldsymbol{x}_0, t_0)}{\partial \boldsymbol{x}_0}\right]^* \left[\frac{\partial \boldsymbol{x}(t_0+\tau, \boldsymbol{x}_0, t_0)}{\partial \boldsymbol{x}_0}\right]\right), \tag{3.4}$$

where * is the matrix transpose operator, and σ_τ is the largest eigenvalue (λ_{max}) of the Cauchy-Green strain tensor, the quantity within the parentheses. The Cauchy-Green strain tensor is a quantification of the deformation of a infinitesimally small fluid volume element. It is used commonly in finite strain theory, but is seeing increased use in the dynamical systems and fluid dynamics communities, and is used to calculate the FTLE as follows:

$$FTLE_\tau(\boldsymbol{x}_0, t_0) = \frac{1}{2\tau}\log\sigma_\tau(\boldsymbol{x}_0, t_0). \tag{3.5}$$

This defines FTLE as a measure of the maximum rate of separation among particles that were initially separated by a finitely small distance around each trajectory initialization point, $\boldsymbol{x}_0$. If a group of particles travel together, for example in a uniform flow, the local FTLE value is small. If the particles are on either side of a material transport boundary, their trajectories will diverge over time, causing the local FTLE value to be high. In order to integrate the particle trajectories, sufficiently resolved velocity data for the spatial domain and temporal range of interest must be available. Maximal ridges of FTLE are extracted using a fixed threshold of FTLE. The FTLE ridges visualize invariant manifolds in both periodic and aperiodic flows. These manifolds are co-dimension one structures (two-dimensional surfaces in three-dimensional domains, and one-dimensional lines in two-dimensional domains) that are invariant under perturbations of the surrounding flow field. They advect with the local flow velocity, and by definition have no mass or momentum flux across their surface.

When the FTLE trajectories are integrated in forward time, for example in the two-dimensional flow, the resulting FTLE ridges denote repelling material lines, and are referred to as pFTLE ridges. The FTLE trajectories can also be integrated backwards in time. Fluid trajectories that are repelled from a region when integrated in negative time are attracted to that region when advected in positive time, resulting in attracting material lines, referred to as nFTLE ridges. FTLE ridges are generally referred to as lines since they are often plotted on two-dimensional planes, even in three-dimensional flow fields. In a three-dimensional FTLE field, the regions of high FTLE are surfaces, and the plotted FTLE ridges are the intersection of these surfaces and the plane of interest. For

both positive and negative FTLE, the scalar fields are defined at t_0, and are calculated using the flow map in both positive and negative time from that starting time for pFTLE and nFTLE fields, respectively. To calculate the FTLE fields at a later time, for example at the next phase of velocity data, t_1, a new grid of trajectories initialized at t_1 must be considered, although others have used the previously computed flow maps specifically to enable an increase in the efficiency of computing many FTLE fields in a common time range (Brunton and Rowley, 2010). The FTLE ridges can be computationally advected through the domain (Haller and Sapsis, 2011), but this would be an unstable calculation, so in the current work new FTLE calculations are performed for each starting time. Ridge extraction algorithms have been developed that decrease the difficulty and error in the ridge advection process, but these algorithms are still sensitive to the spatial resolution of the velocity field (Lipinski and Mohseni, 2010; Allshouse and Peacock, 2015). FTLE ridge advection is unstable when advecting attracting ridges backwards in time, or repelling ridges forward in time, since any location not perfectly on the ridge will rapidly move away from the ridge by definition. If both FTLE ridges were calculated over the same time window, the nFTLE ridge will have been initialized at the end of the time window, and the pFTLE ridge will have been initialized at the beginning of the time window. Therefore, one of the ridges would have to be advected in its unstable direction in order to plot the ridges at the same instant in time (Haller, 2015).

Because the FTLE field yields the attracting and repelling material lines in the flow, they are used to outline the flow structures by showing the transport boundaries between dynamically distinct regions in the flow field. The Q criterion only visualizes the vortex cores, so the ability to visualize the transport boundaries around the vortices objectively provides additional insight into the vortex dynamics, such as entrainment, especially when studying the interactions among coherent structures. FTLE has been demonstrated to be robust to velocity field errors that are small in magnitude or short in duration (Haller, 2002). Due to the Lagrangian nature of the FTLE calculation, small or short duration errors in the velocity field do not have a significant effect on the overall motion of the particles. For example, if an FTLE ridge is located between a vortex and the freestream, small errors in the individual particle integrations will have no effect on whether the

particles end up in the vortex or far downstream. Large errors could cause a particle to travel from one distinct region of the flow field to the other, but the errors would have to be persitently large at multiple spatial locations to cause enough particles to travel across the FTLE ridge to misrepresent its location. Having poor spatial or temporal resolution can have a significant negative effect on the exact FTLE ridge location in some cases, but noise had little effect on the mean location of the FTLE ridge (Olcay et al., 2010).

In order to be considered material lines or surfaces, the FTLE should move with the local flow velocity with no mass flux across them. Calculations were performed to check this using the method developed by Shadden et al. (2005) to determine the mass flux across the FTLE in our results for the $Re = 150$ numerical case. This method determined mass flux by integrating a measure of the ridge sharpness multiplied by the difference between the rotation rate of the FTLE ridge and the Eulerian velocity field along the ridge. The magnitude of the flux was determined to be about 1% of the local mass flux magnitude, but the values were calculated on the discrete computational grid, as opposed to directly on the FTLE ridge. For this reason, 1% was considered a conservative estimate, and the magnitude of normal flux across the FTLE ridge is considered small enough to be negligible.

When plotting FTLE ridges, a certain threshold of the maximum FTLE value in the field is chosen, but this threshold only affects the plotted thickness of the ridges. The location of the ridge does not change, unlike the way changing the Q threshold can change the size and shape of the region considered a vortex. Values of the FTLE threshold for plotting and the integration time in terms of the von Kármán vortex shedding period, T, are shown for the studied cases in table 3.2. The $Re = 400$ case had a shorter integration time due to limits in the available data, but previous studies have shown that the minimum required integration time for cylinder flows is $0.5T$, and any value above that just serves to further refine the FTLE ridges (Rockwood et al., 2016; Kourentis and Konstantinidis, 2011; Bourgeois et al., 2012).

Re	FTLE Threshold	Integration Time
150	0.67FTLE_{max}	$2.0T$
400	0.67FTLE_{max}	$1.5T$
9,000	0.67FTLE_{max}	$2.0T$
19,000	0.60FTLE_{max}	$2.0T$

Table 3.2: FTLE integration time and plotting threshold.

3.1.4 Lagrangian Saddles

The nFLTE and pFTLE ridges are attracting and repelling material lines or surfaces, respectively, so their intersections are topological saddle points or lines in the flow in a Lagrangian sense. These Lagrangian saddles are not always found from traditional Eulerian detection techniques such as plotted streamlines (Miron and Vétel, 2015). This failure of Eulerian methods can be due to the chosen reference frame, or due to unsteady separation behavior. A study was performed on the $Re = 150$ data to ensure the particles in the vicinity of the saddle exhibit saddle-like movement (attraction along one direction with repulsion along another direction) in the Lagrangian sense, especially since the positive time movement occurs over a different "dynamical system" (time window) than the negative time movement.

The behavior of material particles initially located in the vicinity of a Lagrangian saddle is shown in figure 3-2 for the $Re = 150$ case. Each quadrant of particles around the saddle is assigned one solid color, and any particles found near an FTLE ridge ($\text{FTLE} \geq 0.75\text{FTLE}_{max}$) are colored black. There is a clear motion of particles away from the pFTLE ridge (top left to bottom right in figure 3-2(a)) and along the nFTLE ridge (top right to bottom left in figure 3-2(a)), which agrees with the expected behavior of particles in the vicinity of a Lagrangian saddle. This is further observed in the thickening of the black region initially containing particles near the pFTLE ridge as the nearby particles are repelled away, and a narrowing of the black region initially containing particles near the nFTLE ridge as the particles are attracted closer. This trend holds over the entire integration time. While this study was not conducted for the other cases presented, the Lagrangian saddle persists for the entire period of FTLE calculations for

all cases. This persistence implies that the saddles are indeed Lagrangian saddles for initial times considered since the same dynamics are found for each FTLE calculation, and the validation of the $Re = 150$ saddle served to further confirm this.

Following the Lagrangian saddles associated with vortices has revealed vortex dynamics such as the location of wake breakdown in the study of the wake of a trapezoidal pitching panel (Green et al., 2011), and the shedding of the leading edge vortex for a pitching plate (Huang and Green, 2015) and a pitching airfoil (Mulleners and Raffel, 2012). In general, multiple Lagrangian saddles can be found along a vortex-bounding FTLE ridge, even in relatively simple flows such as the von Kármán vortex street behind a circular cylinder. Tracking any of the Lagrangian saddles can indicate the motion of the vortex, but in the results presented in this dissertation, only the locations of the saddle found upstream of the forming and shedding vortex have been observed to be related to the vortex shedding time.

While the FTLE calculation is robust to small scale errors in the velocity fields, there is a finite amount of uncertainty in the location of the Lagrangian saddle related to the discrete grid used. When the Lagrangian saddle is located, the exact point chosen is the location of maximum combined FTLE values at the pFTLE and nFTLE intersection. The intersection of the two ridges is a two-dimensional area in space, so the exact center location is difficult to locate due to the use of a discrete grid. The uncertainty is on the order of two grid points on the FTLE grid. These uncertainty values are shown in table 3.3.

Re	Saddle Location Uncertainty ($2\Delta x/D$)
150	0.010
400	0.009
9,000	0.005
19,000	0.006

Table 3.3: Lagrangian saddle location uncertainties.

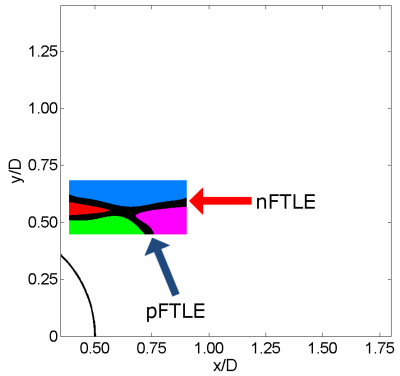

(a) $t/T = 0.75$.

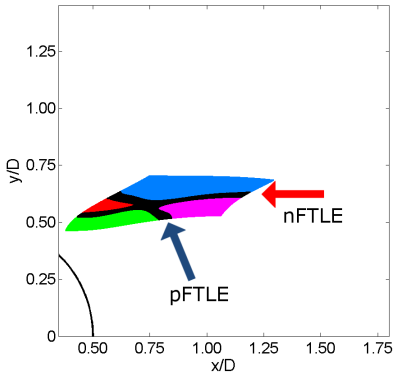

(b) $t/T = 0.82$.

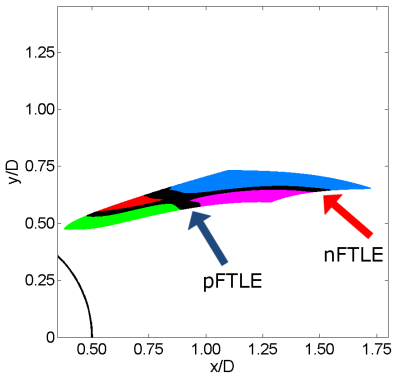

(c) $t/T = 0.89$.

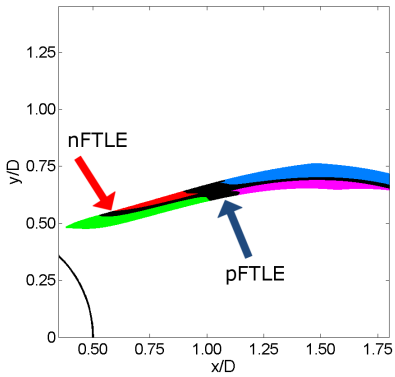

(d) $t/T = 0.96$.

Figure 3-2: Lagrangian particle evolution around a Lagrangian saddle at $Re = 150$. Particles with values above $0.75FTLE_{max}$ are black, other particles are colored by their initial location.

3.2 Pressure Signal Processing

Static pressure data was collected as voltages by the PXIe system described previously. In the raw signal, the amplitude of the fluctuations in pressure due to the formation and shedding of von Kármán vortices was on the same order as the noise levels in the signal, most notably so in the $Re = 19,000$ case due to limitations in the available pressure transducer sensitivity. Because of this, the experimental pressure signals were filtered using a Wiener filter to reduce the noise in the voltage signals. A Wiener filter uses a minimum mean square error estimator to reduce the noise. The filter required an estimation of the noise and the signal, which are approximated using the power spectral density by smoothly extrapolating the noise spectrum throughout the range of frequencies (Press et al., 2007). A curve is then approximated through the portion of the power spectral density that contains the signal. These curves are used to construct the optimal filter. In both cases, the noise was approximated as all values in the power spectral density above 0.75 Hz, and the signal was treated as all frequencies less than 0.75 Hz. 0.75 Hz was located at the high frequency limit of the von Kármán vortex shedding frequency peak in all power spectral density plots, so was used as the limit of the signal of interest. See figures 3-3(a) and 3-4 for power spectral densities. This process reduced the noise significantly in both experimental cases. A low-pass filter was not used during the data collection process, so there is some high frequency fold over into the signal, but the power at these frequencies is at least 3 orders of magnitude lower than the power at the von Kármán shedding frequency across all cases, so its effect is minimal.

$Re = 9,000$

Pressure data was collected for the $Re = 9,000$ case at a sampling frequency of 3 kHz for 300 seconds per run, for 30 runs. The observed von Kármán vortex shedding frequency was 0.53 Hz, which corresponded to a Strouhal number of 0.21 using the cylinder diameter as the wake width. This number is slightly higher than the commonly reported $St = 0.205$ for this Reynolds number (Fey et al., 1998). This is likely due to the non-parallel von Kármán vortex shedding present with the current experimental setup. The signal was oversampled by a factor of 1500 in order to allow for noise reduction in the phase-

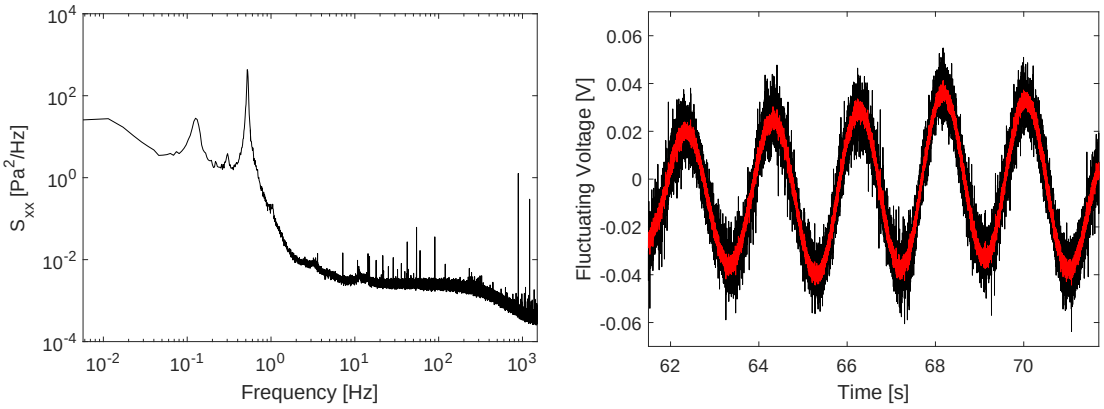

(a) Power spectral density at 70°.

(b) Pressure transducer fluctuating voltage before (black) and after (red) the application of a Wiener filter.

Figure 3-3: $Re = 9,000$ pressure power spectral density and sample signal.

averaging analysis. The block-averaged power spectral density of the raw signal is shown in figure 3-3(a) where the averaging occurred across 90 blocks. A low number of blocks was used to preserve the low frequency resolution around the 0.53 Hz von Kármán vortex shedding frequency. The pressure tap located at 70° is dominated by the von Kármán shedding frequency as expected. An example section of the fluctuating voltage signal before and after the application of the Wiener filter is shown in figure 3-3(b). The noise reduction had the greatest effect near the peak voltages, which increased the accuracy of the phase-averaging algorithm.

$Re = 19,000$

Pressure data was collected for the $Re = 19,000$ case at a sampling frequency of 2 kHz for 300 seconds per run, for 6 runs. The observed von Kármán vortex shedding frequency was 0.53 Hz, which corresponded to a Strouhal number of 0.21 using the cylinder diameter as the wake width. This number is higher than the commonly reported $St = 0.19$ for this Reynolds number (Fey et al., 1998). This is likely due to the non-parallel von Kármán vortex shedding present with the current experimental setup, and blockage effects. Figure 23.19 of Zdravkovich (1997) shows that an increase in blockage from 0.071 to 0.141 causes the Strouhal number to increase from about 0.20 to 0.22. The cases used to determine the relationship between Re and St in the literature used end plates to ensure the von

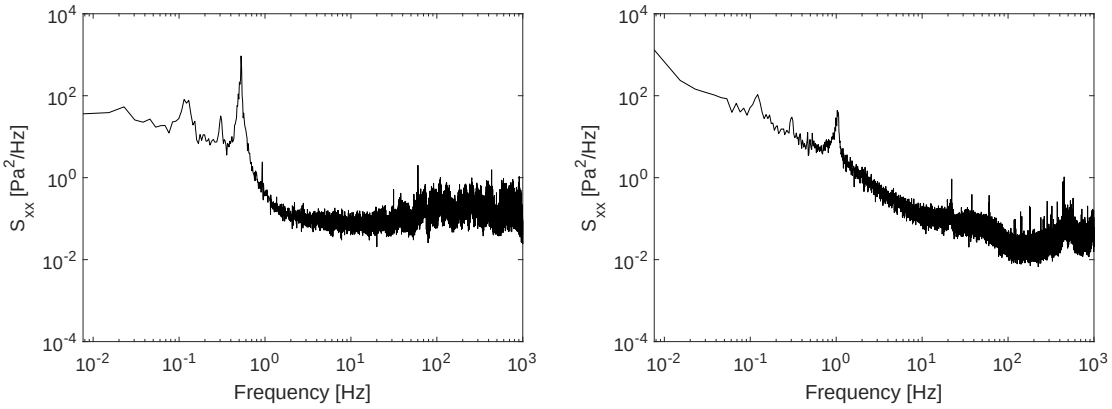

(a) 70°. (b) 180°.

Figure 3-4: $Re = 19,000$ pressure power spectral density for channels located at (a) 70° and (b) 180°.

Kármán vortices shed parallel to the circular cylinder. The signal was oversampled by a factor of 1000 in order to allow for noise reduction in the phase-averaging analysis. The block-averaged power spectral density of the raw signal for two different pressure tap locations is shown in figure 3-4, where the averaging occurred across 18 blocks. A low number of blocks had to be used to preserve the low frequency resolution around the 0.53 Hz von Kármán vortex shedding frequency. The time spent collecting PIV snapshots simultaneously with pressure was optimized, resulting in a significantly lower number of blocks being available in this case compared to the $Re = 9,000$ case. The $Re = 19,000$ case contained 13% of the number of pressure data points collected in the $Re = 9,000$ case. The pressure tap located at 70° is dominated by the von Kármán shedding frequency as expected. The pressure tap located at 180° was expected to have a frequency associated with the drag, which oscillates at twice the von Kármán shedding frequency, as is seen here (Nishimura and Taniike, 2001). Little evidence of the von Kármán shedding frequency exists, and a large peak exists at 1.03 Hz, roughly double the von Kármán shedding frequency. An example section of the fluctuating voltage signal before and after the application of the Wiener filter is shown in figure 3-5. The noise reduction had a significant effect on the clarity of the signal in this case, dramatically reducing the noise.

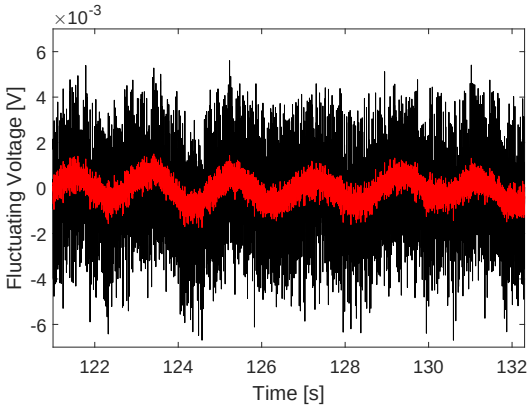

Figure 3-5: $Re = 19,000$ pressure transducer fluctuating voltage before (black) and after (red) the application of a Wiener filter.

3.3 Phase-Averaging

Phase-averaging was utilized to increase the temporal resolution of the experimentally obtained velocity fields, which were collected at 4 Hz due to limitations of the equipment. It also allowed for the stitching of multiple windows of velocity data that were collected at different times to increase the spatial domain size. Phase-averaging was conducted on the $Re = 9,000$ case using both snapshot proper orthogonal decomposition (POD) applied to the PIV velocity fields, and with the simultaneous static pressure signal at a fixed location. Phase-averaging was applied to the $Re = 19,000$ case using the pressure signal in an identical manner to the $Re = 9,000$ case. Both techniques were described and compared by Perrin et al. (2007), who found that both techniques performed adequately for a single window of PIV data, however the pressure signal technique overestimated the contribution of the random fluctuations in the velocity field to the turbulent shear stress due to the finite lag time between the pressure signal and the velocity fluctuations. This means that the pressure signal technique yielded errors in the phase angle calculation since there were more random fluctuations in each phase-averaged velocity field than in the phase-averaged fields calculated using POD. In the work presented here, both techniques yielded similar results, but challenges arose when trying to use the POD technique for phase-averaging between multiple downstream locations. A comparison between the two techniques is provided below.

3.3.1 Proper Orthogonal Decomposition

The snapshot Proper Orthogonal Decomposition (POD) technique developed by Sirovich (1987) was used to decompose the velocity fields collected by PIV into spatial eigenmodes and temporal coefficients on an energy basis. Snapshot POD uses the two-time correlation tensor, $C(t,t')$, which is defined as:

$$C(t,t') = \frac{1}{T_s}\int_{\mathcal{D}} \sum_{i=1}^{3} u_i(\boldsymbol{x},t)u_i(\boldsymbol{x},t')d\boldsymbol{x}, \tag{3.6}$$

where T_s is the total number of PIV velocity fields (snapshots), $\mathcal{D}$ represents the spatial domain of the PIV velocity fields, and $u_i(\boldsymbol{x},t)$ is the fluctuating velocity field. The two-time correlation tensor is then used in the integral eigenvalue problem:

$$\int_{T_s} C(t,t')a_n(t')dt' = \lambda^{(n)}a_n(t), \tag{3.7}$$

where $a_n(t)$ are the temporal coefficients, and $\lambda^{(n)}$ are the eigenvalues, or the amount of energy contained in the nth mode. Spatial eigenmodes, $\phi^{(n)}$, are calculated from:

$$\phi^{(n)}(\boldsymbol{x}) = \frac{1}{T_s\lambda^{(n)}}\int_{T_s} a_n(t)u_i(\boldsymbol{x},t)dt. \tag{3.8}$$

The modes are then sorted by decreasing energy (eigenvalue), and a representation of the velocity fields using a certain number of modes can be calculated from:

$$u_i(\boldsymbol{x},t) = \sum_{n=1}^{N} a_n(t)\phi_i^{(n)}(\boldsymbol{x}), \tag{3.9}$$

where N is the total number of modes used.

In periodic flows, POD modes are found to occur in pairs that represent the orthogonal components of the harmonics of the vortex shedding process (Oudheusden et al., 2005). In the $Re = 9,000$ case, the first two modes contained approximately 30% of the total energy of the flow and were associated with the convection of the von Kármán vortices. Figure 3-6 shows the the temporal coefficients of the first two modes normalized by their energy, where each x is the location of a_2 versus a_1 for a velocity field. The variation in

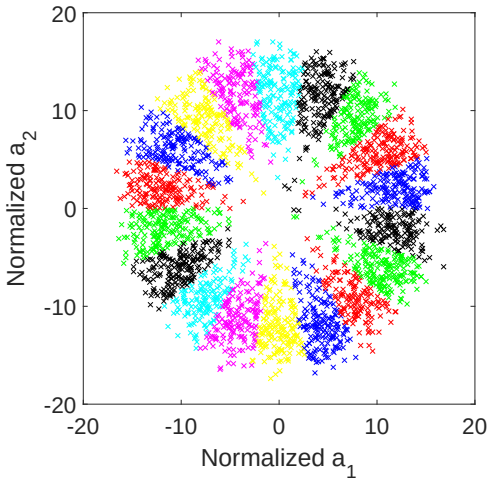

Figure 3-6: $Re = 9,000$ POD phase-averaging bins.

the radius of the circle is thought to be caused by variations in the periodicity of the von Kármán vortex shedding which are induced by turbulence and small-scale fluctuations (Oudheusden et al., 2005). In order to phase-average this data, velocity fields were organized into bins with a width of 20 degrees to define each phase, which are colored in figure 3-6. The full velocity fields associated with the temporal coefficients in each bin were averaged to produce one phase-averaged velocity field per bin. This technique requires large enough spatial windows of data to allow for accurate calculation of the POD modes within each window (camera location) of data. When this technique is performed at multiple spatial locations that will be stitched together, the phases need to be aligned to ensure they are representing the same physical phase of data in both locations. This was done by comparing the wake structures of the phase-averaged velocity fields between each spatial location using Q, while varying the phase bias in the POD phase angle for one location until the two spatial locations appeared to be at the same phase. This process is inexact and time consuming, and was the reason this technique was not used in the $Re = 19,000$ case.

3.3.2 Pressure Signal

The periodic pressure signal related to the von Kármán vortices is commonly used to phase-average velocity fields generated from PIV for circular cylinder flows. In both

experimental cases, the triggering signal for the first PIV laser flash (Q-switch) was used as the timing of the velocity field acquisition. The phase-averaging code determined the phase angle of each velocity field by determining the phase of the coincident pressure signal at the time the velocity field was acquired. This was done by locating two peaks and a trough for the pressure signal in the region encompassing the timing of the velocity field of interest. If the peak-to-peak period of the signal section was more than 20% greater or less than the average period of the von Kármán vortex shedding, the period was considered irregular and that velocity field was discarded. 20% was chosen to allow for variations in the period that are present in experimental results at this Reynolds number. Periods more than 20% different were primarily due to errors in the peak finding algorithm. The phase angle was calculated based on the velocity field's relative time between the two peaks in the pressure signal. The exact phase of the pressure signal peak was difficult to determine as some noise was still present in the pressure signal after filtering, so the signal was averaged over a certain number of points in each case. For the $Re = 9,000$ case, the block size for averaging was 100 resulting in a final signal resolution of 30 Hz, and for the $Re = 19,000$ case, the block size for averaging was 99, resulting in a final signal resolution of 20 Hz. This technique greatly improved the accuracy of the peak finding algorithm, even though it reduced the time resolution, and allowed for phase angle calculations using this technique. An example of the filtered signal, averaged signal, and PIV snapshot location are shown in figure 3-7. The phase angles associated with each velocity field are then placed within phase bins in a similar manner to the POD phase-averaging described above. The $Re = 9,000$ case used 20° bins, resulting in 18 phases per period, and the $Re = 19,000$ case used 15° bins, resulting in 24 phases per period.

3.3.3 Phase-Averaging Comparison

Figure 3-8 shows the phase angles found by both the POD and pressure signal phase-averaging techniques for a portion of the $Re = 9,000$ data. The POD technique consistently finds the correct phase, as seen by the constant $2\pi/T$ slope of each line, but while the pressure signal technique generally finds approximately the same slope, it is often

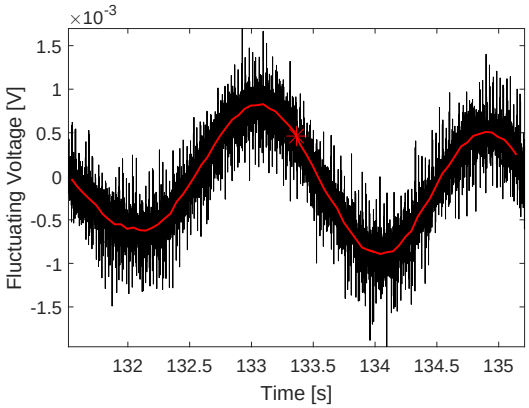

Figure 3-7: Sample filtered signal (black), averaged signal (red), and PIV snapshot location (red asterisk).

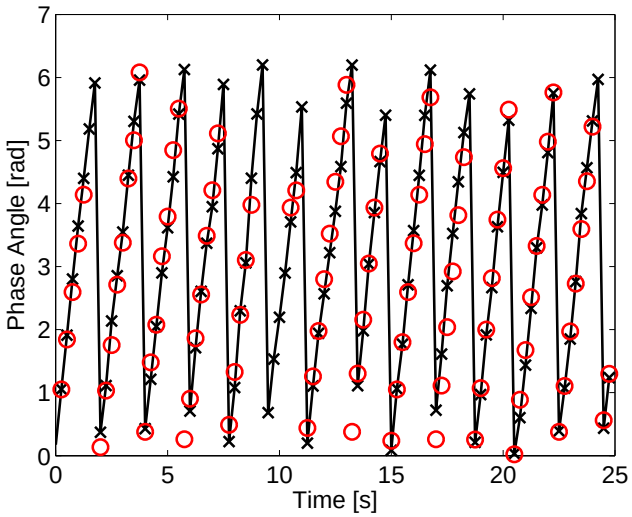

Figure 3-8: Phase angles found by POD (black x's) and pressure signal (red o's).

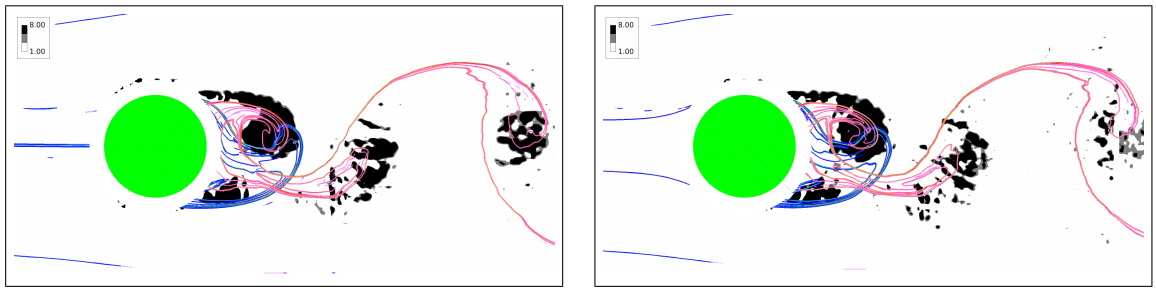

(a) POD. (b) Pressure signal.

Figure 3-9: Comparison of Q (grey), nFTLE (red), and pFTLE (blue) results for different phase-averaging techniques at $Re = 9,000$.

shifted slightly above or below the line from the POD technique in each period. This is likely due to errors in the peak finding algorithm discussed above. If both of the peaks were found to be shifted one point off from the correct peak in the same direction, this would cause an error of 6° in the found phase angle. Since the peaks could be found incorrectly in either direction by a couple of points on the 30 or 20 Hz averaged signals due to high levels of noise, this can lead to errors close to one bin width in magnitude. While errors in the phase angle of this magnitude can cause some velocity fields to be placed in the wrong phase-averaging bin, the errors are minimized during the averaging process, as the number of samples is high $\mathcal{O}(100)$, and the majority of the files will be in the correct bin. There will be a small increase in the random fluctuations away from the true phase-averaged velocity field, as discussed by Perrin et al. (2007), but this small increase in error does not affect the FTLE field in a significant manner, as seen in figure 3-9. The only clear difference between the wake structure in between the two techniques is the loss of coherence in the vortex furthest downstream (to the right) found by Q in the pressure signal case. Since the FTLE results were not significantly effected by the use of the pressure signal technique, it was implemented in favor of the POD technique to avoid the inaccurate and time consuming phase lag determination between multiple spatial locations. When only one window of PIV data is in consideration, the POD technique is recommended.

3.4 Three-Dimensional Effects

While methods to find the FTLE ridges from experimental data are both possible and promising using existing techniques, there is still considerable work to be done to address how the accuracy of Lagrangian scalar fields can be established. For many complex three-dimensional flows, three-component velocity fields covering a sufficiently large, three-dimensional portion of the fluid domain over a sufficient period of time are rarely available due to time and system cost constraints.

If velocity information is only available on one plane of data in a three-dimensional flow field, significant errors in the FTLE trajectory calculations can arise. Unpublished work found that the orientation of the coherent structures relative to the FTLE plane can cause errors in a two-dimensional FTLE calculation. When the vorticity vector is aligned nearly perpendicular to the FTLE plane, the vortex induced velocity is primarily in the plane, but if the vorticity vector is aligned in a non-perpendicular fashion it induces large out-of-plane velocities that are not captured in a two-dimensional FTLE calculation. Even if three-component velocity information is available in one plane, the particles that are advected out of the plane cannot be followed, and therefore can not be used in the FTLE calculation.

In order to quantify the degradation of FTLE as a function of the local vortex angle, the simple example of Hill's spherical vortex was used. This flow is an analytical solution to Euler's equation that allows for easy calculations of local vortex angle and FTLE boundaries for a single vortex. The velocity field is defined by Hill (1894) and results in a spherical vortex ring with a prescribed radius. The equations defining the velocities inside and outside of the Hill's spherical vortex are shown below, where $\alpha = 2$ and the vortex radius, r, is 1. While the spherical vortex is technically two-dimensional (axisymmetric), it provides a systematic change in vortex angle in rectangular space. The freestream flow is in the negative z-direction, and planes of data at constant y were studied. In each constant y plane, two cores are visible in the intersection of the vortex ring. Figure 3-10 shows the $y/r = 0$ plane with streamlines highlighting the two cores. At $y/r = 0$, these vortex cores are perpendicular to the plane. As the plane of computation shifts ($y/r > 0$),

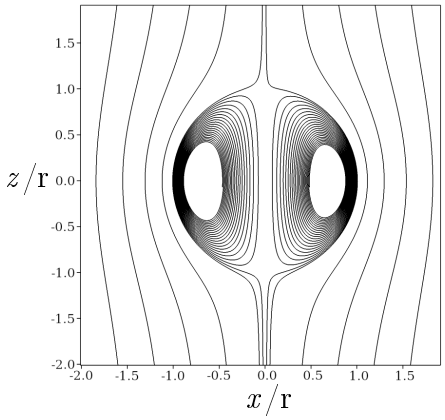

Figure 3-10: Streamlines of Hill's spherical vortex at $y/r = 0$.

the out of plane vorticity angle at the vortex core, which starts at 90°, begins to decrease as the vortices start to tilt into the plane.

Inside vortex

$$u = \alpha xz/5, \tag{3.10}$$

$$v = \alpha yz/5, \tag{3.11}$$

$$w = (\alpha/5)\left(r^2 - z^2 - 2x^2 - 2y^2\right), \tag{3.12}$$

Outside vortex

$$u = \alpha r^5 xz/\left[5\left(x^2+y^2+z^2\right)^{(5/2)}\right], \tag{3.13}$$

$$v = \alpha r^5 yz/\left[5\left(x^2+y^2+z^2\right)^{(5/2)}\right], \tag{3.14}$$

$$w = \frac{-\alpha r^2\left\{\left[2\left(x^2+y^2+z^2\right)^{(5/2)}\right] - 2r^3z^2 + r^3y^2\right\}}{15\left[\left(x^2+y^2+z^2\right)^{(5/2)}\right]}, \tag{3.15}$$

To investigate the effect of only having one plane of data in a three-dimensional flow, both full and constrained FTLE calculations were conducted in planes parallel to the free stream. The full three-dimensional velocity data domain was used for the full nFTLE

calculation, while for the constrained nFTLE case, out-of-plane velocity (v) was set to zero as a model of planar PIV, so the trajectories used to calculate the constrained FTLE were limited to the data plane. A few examples of the full and constrained nFTLE fields are shown in figures 3-11, 3-12, and 3-13. A two-dimensional cross correlation between the full and constrained FTLE fields with no spatial shift was performed to determine how close the constrained FTLE was to the correct results. Figure 3-14 displays the FTLE correlation values as a function of vortex core angle through the plane. When the vorticity vector is aligned perpendicular to the plane of interest at the midsection of the sphere (90° out-of-plane vorticity angle), the out-of-plane velocity is identically zero, so the constrained FTLE is identical to that of the full FTLE, as represented by the unity correlation value. As the vorticity vector becomes less perpendicular to the plane, the error in the constrained FTLE increases, resulting in a lower correlation. At $y/r = 0.64$, where the vortex core angle is 48° from the plane surface, the correlation is only 53%.

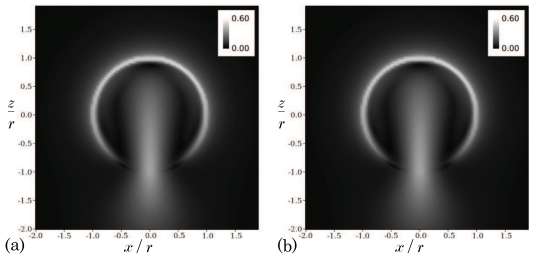

Figure 3-11: nFTLE for Hill's spherical vortex at $y/r = 0.0$ (a) Full nFTLE (b) Constrained nFTLE

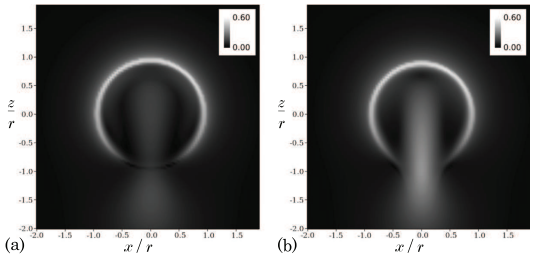

Figure 3-12: nFTLE for Hill's spherical vortex at $y/r = 0.32$ (a) Full nFTLE (b) Constrained nFTLE

A similar study was conducted using the three-dimensional $Re = 400$ numerical data. The full FTLE calculation allowed the particles to advect throughout the full three-

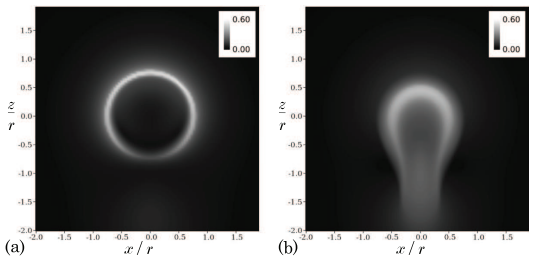

Figure 3-13: nFTLE for Hill's spherical vortex at $y/r = 0.64$ (a) Full nFTLE (b) Constrained nFTLE

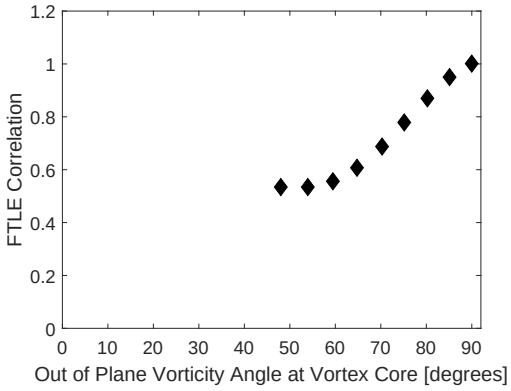

Figure 3-14: Correlation values between full and constrained nFTLE for Hill's spherical vortex.

dimensional domain, but the constrained FTLE treated the spanwise velocity component as identically zero, fixing the particles to the plane. The results of this study are seen in figure 3-15. While there are some differences in the two FTLE fields, the main features of interest for this study in the vicinity of the von Kármán vortices are similar. This is to be expected, as the out of plane velocity in those regions is low due to the alignment of the vortices perpendicular to the plane. The location with a large amount of error is the region just downstream of the lower vortex, marked with a black arrow in each image, where a streamwise-orientated vortex induces a large amount of out of plane velocity. Most importantly, the Lagrangian saddle (green box) behavior is nearly identical between the two cases, indicating that planar PIV results will be sufficient for the Lagrangian saddle calculations, even at Reynolds numbers where three-dimensional effects are present. More details comparing the two cases are shown in section 4.1.2.

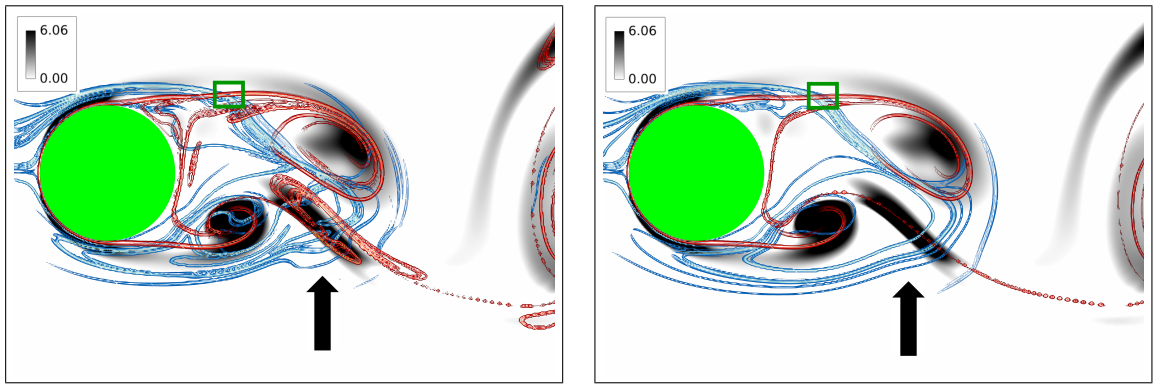

(a) Full FTLE. (b) Constrained FTLE.

Figure 3-15: Comparison of Q (grey), nFTLE (red), and pFTLE (blue) results for full and constrained FTLE calculations for a circular cylinder simulation at $Re = 400$. The green box indicates the Lagrangian saddle, and the black arrow indicates the region of high FTLE error due to out-of-plane velocities caused by streamwise-oriented vortices.

3.4.1 Flow Visualization Study

Due to the potential for errors in the experimental FTLE calculations, which used a single plane of two-component velocity data, a three-dimensional flow visualization study of the near-wake was conducted for the $Re = 9,000$ case. This study sought to determine if the von Kármán vortices were nearly perpendicular to the PIV plane. The surface of the cylinder was painted with highly concentrated fluorescein dye, and then immersed into still water. A continuous wave laser operating at 473 nm, which was near the peak excitation wavelength of fluorescein, was used to illuminate the fluorescein as it was entrained into the von Kármán vortices after the flow was introduced. A 12 megapixel color camera was used to capture images. The high freestream velocity and three-dimensional turbulence resulted in the majority of the dye being removed from the cylinder surface soon after the transient effects due to starting the water tunnel died out, making it difficult to capture high contrast images of the wake structure. The $Re = 19,000$ case was not included in this study, as the further increase in Reynolds number would degrade the clarity of images produced by this technique.

Two representative images are presented in figure 3-16. In both images the flow is traveling from left to right, with the cylinder mounted vertically on the left side of each

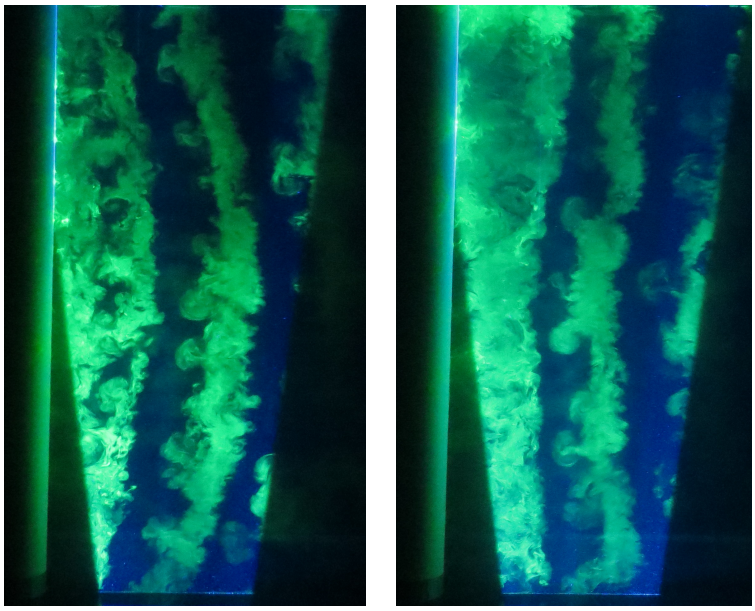

(a) (b)

Figure 3-16: Fluorescein dye flow visualization on a circular cylinder at $Re = 9,000$.

image. The view is from the side of the water tunnel, and the fluorescing green regions are the von Kármán vortices that contain the fluorescein dye. There is significant variation between the angular distribution of the spanwise vortices between different images. The angle of the vortex also varies along the span of the vortex, and is affected by the end conditions (Williamson, 1989). Near the floor of the water tunnel and at the free surface, the vortex core angle drops as low as 70°, but in each case the angle of the vortex at the centerline is nearly 90°. This relationship held true over several, $\mathcal{O}(10)$, flow visualization runs. The images selected are representative of all of the runs, and were chosen based on their dye clarity. The planar PIV data was collected at the tunnel centerline at a cylinder spanwise constant plane. Since the out of plane vortex core angle is approximately 90° in this plane, it is assumed that the errors in the FTLE results due to three-dimensional effects are minimal.

Chapter 4

Results

In this chapter the results obtained for the four cases previously described are presented. The various sections focus on visualization of the wake using Q and FTLE, the Lagrangian saddle locations, and the relationship between the wake, the Lagrangian saddles, and the static pressure on the cylinder surface.

4.1 Wake Visualization

The wake of a circular cylinder is visualized using the Eulerian Q criterion and the Lagrangian finite-time Lyapunov exponent (FTLE), which were calculated using the experimentally and numerically generated velocity fields. Visualizations of the wake for each of the four Reynolds numbers studied is shown below. The figures focus on the portion of the shedding period that includes the formation and shedding of one of the two von Kármán vortices shed each period and its associated Lagrangian saddle from the upper shear layer.

4.1.1 $Re = 150$

The near-wake region behind the circular cylinder at $Re = 150$ is visualized at six instants in time in figure 4-1, chosen to highlight the Lagrangian saddle shedding process. Flow is from left to right, and the cylinder is shown in green. The development of the von Kármán

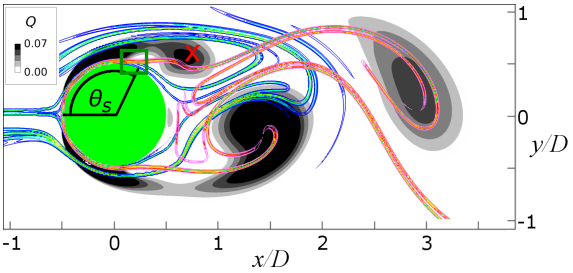

(a) $Re = 150$ wake at $t/T = 0.16$. Red "X" highlights the vortex of interest.

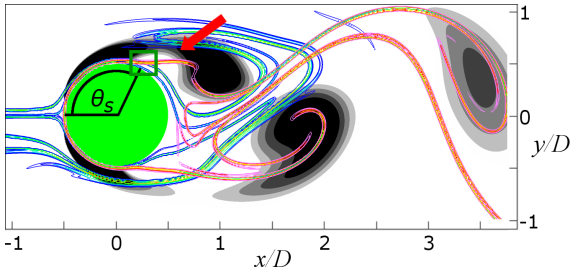

(b) $Re = 150$ wake at $t/T = 0.33$. The red arrow indicates the gap in FTLE ridges where the shear layer is entrained into the forming vortex.

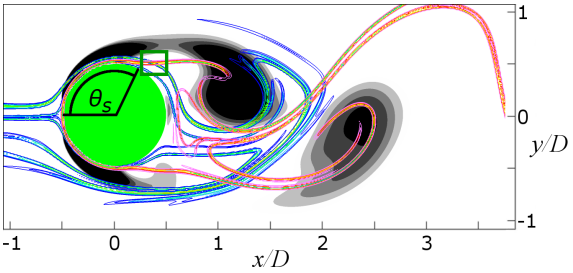

(c) $Re = 150$ wake at $t/T = 0.49$.

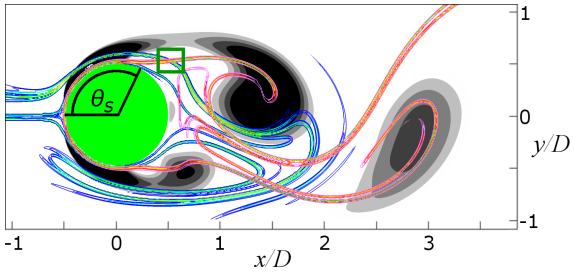

(d) $Re = 150$ wake at $t/T = 0.65$.

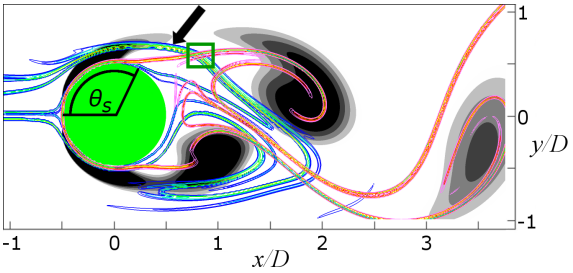

(e) $Re = 150$ wake at $t/T = 0.84$. The black arrow highlights the pFTLE ridge that separates the shear layer from the shed vortex.

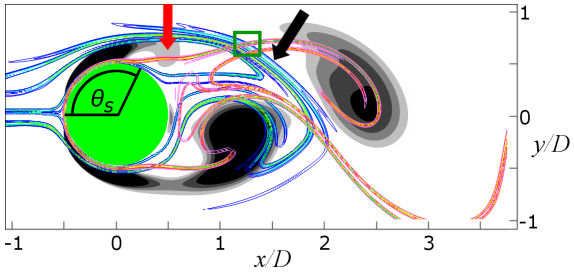

(f) $Re = 150$ wake at $t/T = 1.0$. The red arrow shows the new vortex that is beginning to form. The black arrow highlights the splitting pFTLE ridge.

Figure 4-1: Wake visualization for $Re = 150$ with Q criterion (gray contours), nFTLE ridges (red), pFTLE ridges (blue), and cylinder (green). The Lagrangian saddle is located inside of the green box.

vortex street can be seen as the dark grey regions of Q that are shed in an alternating pattern from the top and bottom half of the cylinder. The FTLE ridges can be seen in blue (repelling ridge, pFTLE) and red (attracting ridge, nFTLE), and the vortex cores are identified as regions where $Q > 0$ with grey contours. The colorbar for Q is kept identical throughout the figure. The Lagrangian saddle of interest, found at the intersection of the nFTLE and pFTLE ridges just upstream of the clockwise-rotating vortex (marked with a red "X") forming and shedding from the upper surface of the cylinder , is indicated by the green box. The attracting nFTLE ridges (red) wrap around the outside boundaries of the vortices as they form, separate, and convect downstream. The repelling pFTLE ridges (blue) form the boundaries between vortices, between forming vortices and the cylinder surface, and between vortices and the freestream flow.

In figure 4-1(b) the forming vortex is entraining fluid from the shear layer through a gap between the nFTLE and pFTLE ridges, marked with a red arrow. The Lagrangian saddle is located close to the cylinder, where it remains as the vortex continues to grow in size. In figure 4-1(c), the vortex is now in the process of shedding from the cylinder. The Lagrangian saddle lifts away from the cylinder surface at this time, and the gap between the FTLE ridges sweeps around the vortex to its downstream side. By $t/T = 0.84$ (figure 4-1(e)) the upstream side of the vortex is fully-enclosed by the FTLE ridges, and has separated from the shear layer. This separation can be seen from the pFTLE ridge that crosses the downstream edge of the shear layer (black arrow), separating it from the vortex. The Lagrangian saddle is now in a location between the shear layer and the vortex. Figure 4-1(f) shows the continued evolution of the flow, as another vortex begins to form from the shear layer above the cylinder, marked with a red arrow. The pFTLE ridge associated with the Lagrangian saddle can now be seen splitting into multiple ridges, marked with a black arrow. One of the ridges will remain in roughly its current location, and will separate the forming vortex from the downstream portions of the flow, while the other branch of the ridge will continue downstream containing the Lagrangian saddle associated with the shed vortex.

4.1.2 $Re = 400$

Figure 4-2 displays the three-dimensional wake structure for the $Re = 400$ case. Figure 4-2(a) shows a dark grey isosurface at $Q = 0.017Q_{max}$, with the cylinder shown in light grey for reference. The Q threshold was increased from $Q > 0$ to $Q = 0.017Q_{max}$ to keep portions of the wake from being obscured by structures with low Q magnitudes. Flow is from the bottom left to the top right ($+x$ direction). The von Kármán vortices can be seen as bands of high Q that are roughly parallel to the cylinder, and mode B vortices can be seen as the thin strings of streamwise-oriented Q-isosurfaces between the von Kármán vortices. The mode B vortices are more clearly highlighted in the subsequent figures where the Q-isosurface is colored by the magnitude of each component of vorticity. The streamwise and transverse (x and y, respectively) components of vorticity highlight the mode B vortices in figures 4-2(b) and 4-2(c), and the spanwise (z) component of vorticity highlights the von Kármán vortices in figure 4-2(d). More details of the wake structure can be identified by investigating spanwise-constant cross-sections, which allow for comparison between this case and the cases with only planar data.

Figure 4-3 shows the three components of vorticity, as well as the out-of-plane velocity in a spanwise-constant plane at $z/D = 3.72$, a location that was chosen to intersect with a mode B vortex. In the figure, a black contour is included at $Q = 0.003Q_{max}$ as a reference for the vortex locations. The contour was selected just above 0 to more clearly outline the von Kármán vortices. Figure 4-3(a) shows the spanwise component of vorticity, which is concentrated in the von Kármán vortices as expected. Figure 4-3(a) also shows a small region of negatively signed vorticity on the downstream surface of the cylinder. This is indicative of the transverse flow (downward) induced by the positively-signed forming vortex near the cylinder. Figures 4-3(b) and 4-3(c) show the streamwise and transverse component of vorticity, respectively, and are concentrated in the mode B vortices between the von Kármán vortices. The out-of-plane velocity shown in figure 4-3(d) is mainly concentrated on the top and bottom of the mode B vortices, where the streamwise-oriented vortices induce large out-of-plane motions. As discussed in section 3.4, the constrained FTLE breaks down in this region, but the area upstream

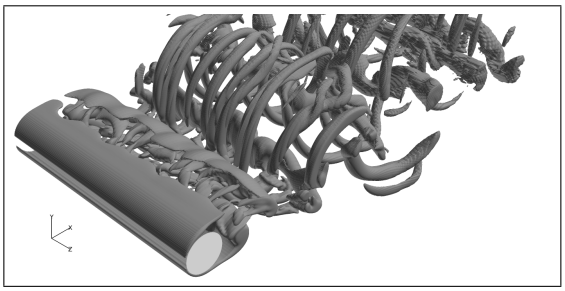

(a) Three-dimensional wake structure visualized by an isosurface at $Q = 0.017Q_{max}$.

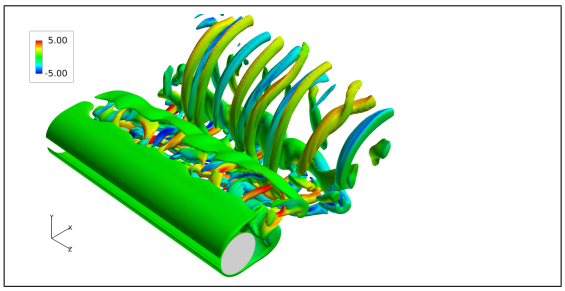

(b) Q colored by streamwise vorticity ω_x [rad/s].

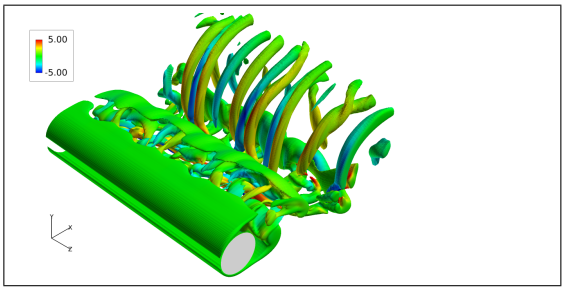

(c) Q colored by transverse vorticity ω_y [rad/s].

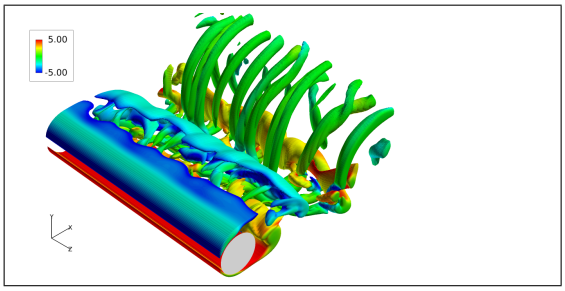

(d) Q colored by spanwise vorticity ω_z [rad/s].

Figure 4-2: $Re = 400$ three-dimensional wake structure at $t/T = 0.80$ with cylinder in grey, and an isosurface of Q at $Q = 0.017Q_{max}$.

of the von Kármán vortices where the Lagrangian saddle is located remains accurate due to minimal out-of-plane velocity.

FTLE ridges in the near-wake region at $Re = 400$ for a spanwise-constant plane located at $z/D = 3.72$ are shown in figure 4-4. At this Reynolds number the flow is three-dimensional, but a two-dimensional slice of the full FTLE field is presented to allow for ease of visualization and comparison to other cases. The full three-dimensional velocity data domain is still used for the FTLE particle integration. The grey Q contours highlighting the vortex cores capture the von Kármán vortices as in the $Re = 150$ case, but they also show the mode B vortices (green arrow in figure 4-4(a)) in between the von Kármán vortices. Due to the complex movement of the particles as they are advected out of the plane by the induced out-of-plane velocity, there are more ridges in the FTLE field compared to the two-dimensional results at $Re = 150$. The alleyway of entraining fluid that feeds the forming vortex from the shear layer is not as apparent in figures 4-4(a), but there are multiple lobes enclosed by pFTLE ridges that demarcate regions of

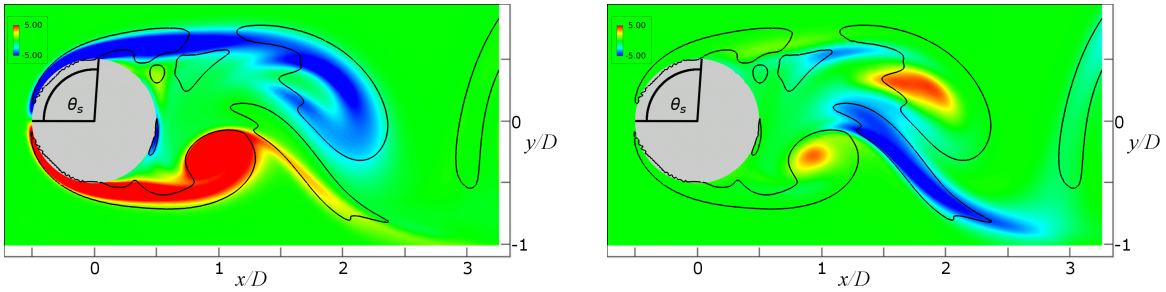

(a) Spanwise vorticity ω_z [rad/s].

(b) Streamwise vorticity ω_x [rad/s].

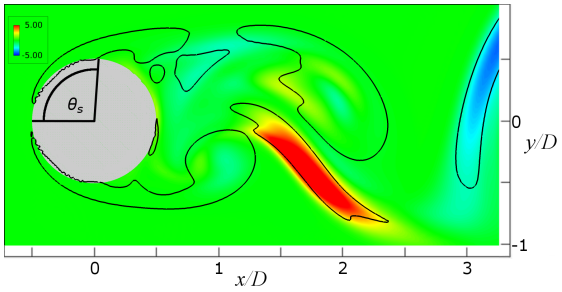

(c) Transverse vorticity ω_y [rad/s].

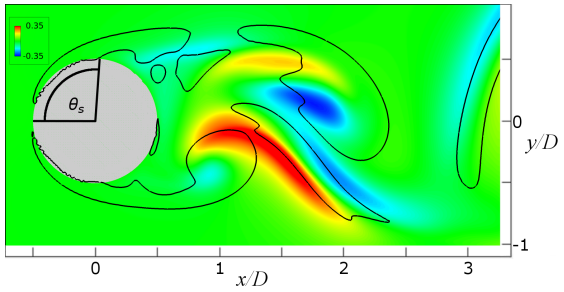

(d) Out-of-plane velocity normalized by freestream velocity w/U_∞

Figure 4-3: $Re = 400$ three-dimensional effects for $z/D = 3.72$ plane at $t/T = 0.80$ with cylinder in grey, and $Q = 0.003Q_{max}$ contour in black.

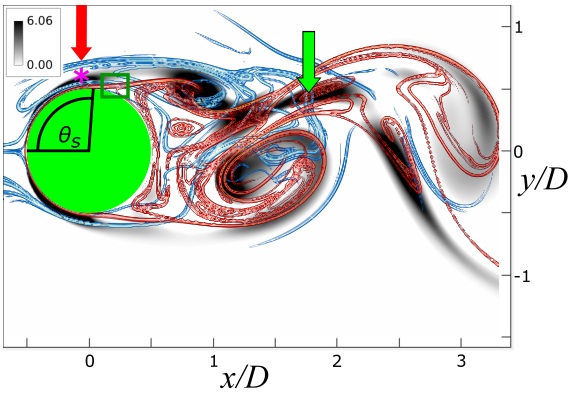

(a) $Re = 400$ wake at $t/T = 0.16$. The green arrow indicates a mode B vortex. The magenta asterisk and red arrow highlight a lobe that is being entrained into the forming vortex.

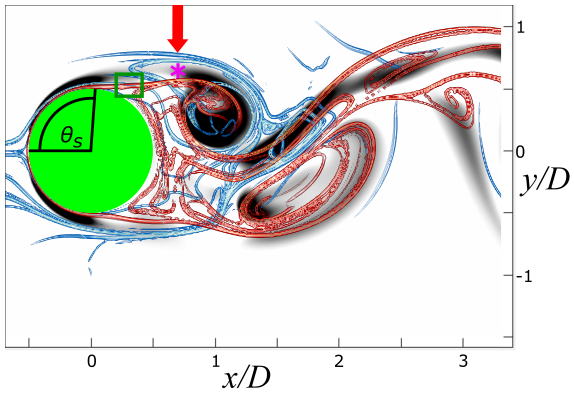

(b) $Re = 400$ wake at $t/T = 0.32$. The magenta asterisk and red arrow highlight a lobe that is being entrained into the forming vortex.

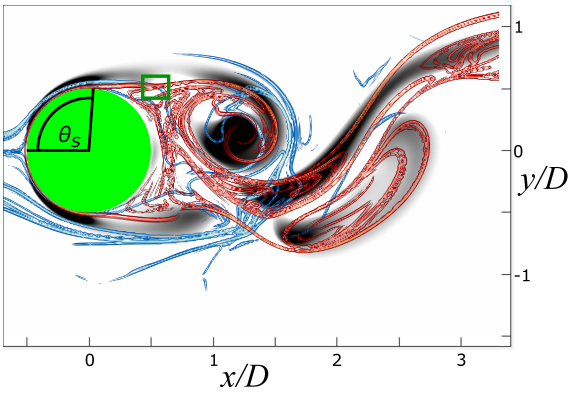

(c) $Re = 400$ wake at $t/T = 0.48$.

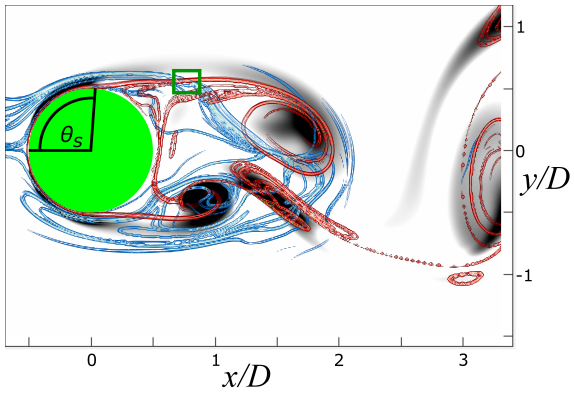

(d) $Re = 400$ wake at $t/T = 0.68$.

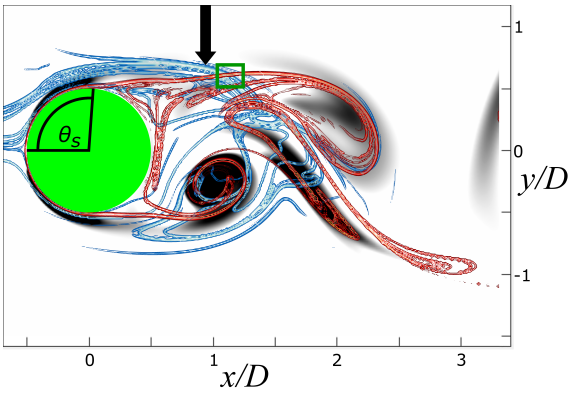

(e) $Re = 400$ wake at $t/T = 0.84$. The black arrow highlights the splitting pFTLE ridge.

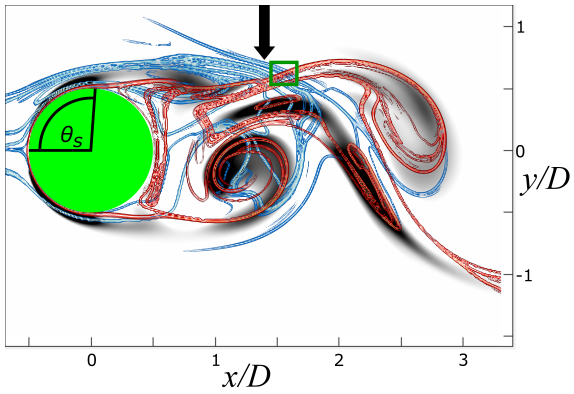

(f) $Re = 400$ wake at $t/T = 1.0$. The black arrow highlights the splitting pFTLE ridge.

Figure 4-4: Wake visualization for full $Re = 400$ with Q criterion (gray contours), nFTLE ridges (red), pFTLE ridges (blue), and cylinder (green). The Lagrangian saddle is located inside of the green box.

fluid that will be fed into the forming vortex from the shear layer. This can be seen during the vortex formation process in figures 4-4(a) and 4-4(b) where one of the lobes is marked with a magenta asterisk and a red arrow. The Lagrangian saddle is close to the cylinder surface in figure 4-4(a), but can be seen moving away from the cylinder slightly in figure 4-4(b), and more clearly in figure 4-4(c) onward. As the vortex sheds and begins to convect downstream, the core region where $Q > 0$ begins to lose coherence. This is likely due to stretching of the vortex by three-dimensional effects. The splitting of the pFTLE ridge (marked by a black arrow) can be seen in figures 4-4(e) and 4-4(f), with the ridge splitting into multiple ridges at this Reynolds number, as opposed to the two-dimensional case where the ridge only split in two. This is indicative of more complex interactions between different portions of the flow, and can be seen in the more complex FTLE field throughout the wake.

Figure 4-5 displays the results for the $Re = 400$ constrained FTLE case, which is used to mimic the effects of having only planar velocity data. This is planar FTLE where the out-of-plane velocity values were set to zero during the particle advection, artificially constraining them to the plane of interest. The three-dimensional Q values are plotted for comparison to the full three-dimensional FTLE case shown in figure 4-4. The FTLE ridges still bound the vortex cores found by Q, but much of the complexity that was seen in figure 4-4 no longer exists. This case looks more similar to the two-dimensional $Re = 150$ case shown in figure 4-1. Interestingly, the alleyways that allowed the shear layer to feed the forming vortex in the $Re = 150$ case are still not present in this case, instead exhibiting the lobed feeding (magenta asterisk and red arrow in figures 4-5(a) and 4-5(b)) from the shear layer that was seen in the full $Re = 400$ FTLE case. The Lagrangian saddle behavior is nearly identical between the full and constrained cases at $Re = 400$, and the main inaccuracies in the FTLE field occur in the vicinity of the streamwise oriented vortices, as expected. The main focus of this work is the identification and tracking of the Lagrangian saddles in the near-wake region, so the inaccuracies near the streamwise oriented vortices were not of major concern as the flow between the forming and shedding von Kármán vortices and the cylinder has minimal out-of-plane velocity.

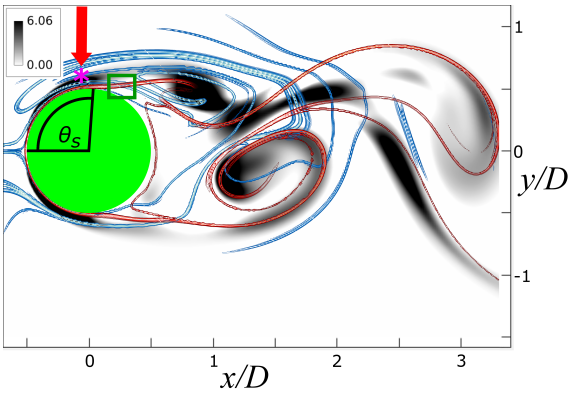

(a) $Re = 400$ wake at $t/T = 0.16$. The magenta asterisk and red arrow highlight a lobe that is being entrained into the forming vortex.

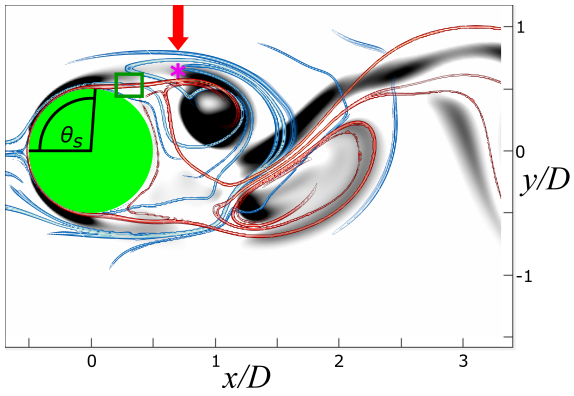

(b) $Re = 400$ wake at $t/T = 0.32$. The magenta asterisk and red arrow highlight a lobe that is being entrained into the forming vortex.

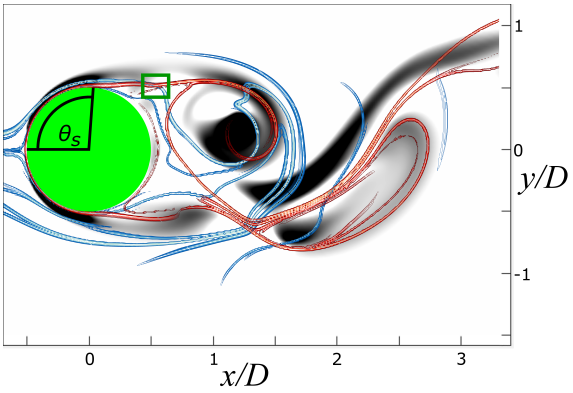

(c) $Re = 400$ wake at $t/T = 0.48$.

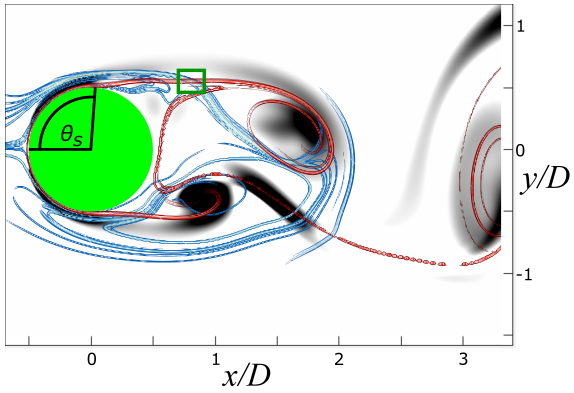

(d) $Re = 400$ wake at $t/T = 0.68$.

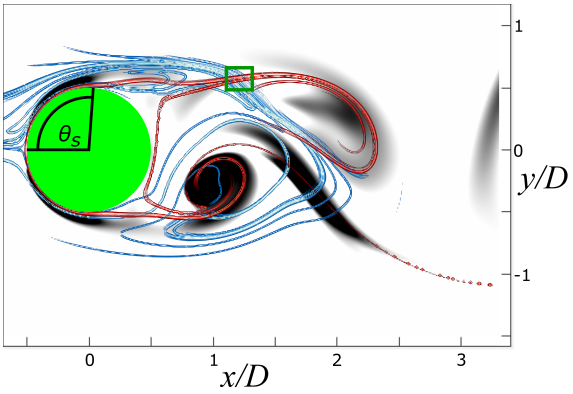

(e) $Re = 400$ wake at $t/T = 0.84$.

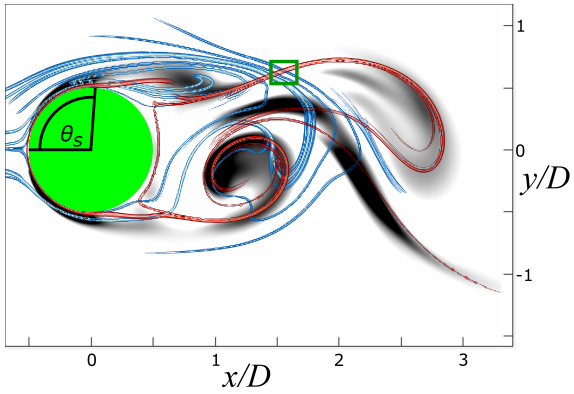

(f) $Re = 400$ wake at $t/T = 1.0$.

Figure 4-5: Wake visualization for constrained $Re = 400$ with Q criterion (gray contours), nFTLE ridges (red), pFTLE ridges (blue), and cylinder (green). The Lagrangian saddle is located inside of the green box.

4.1.3 $Re = 9,000$

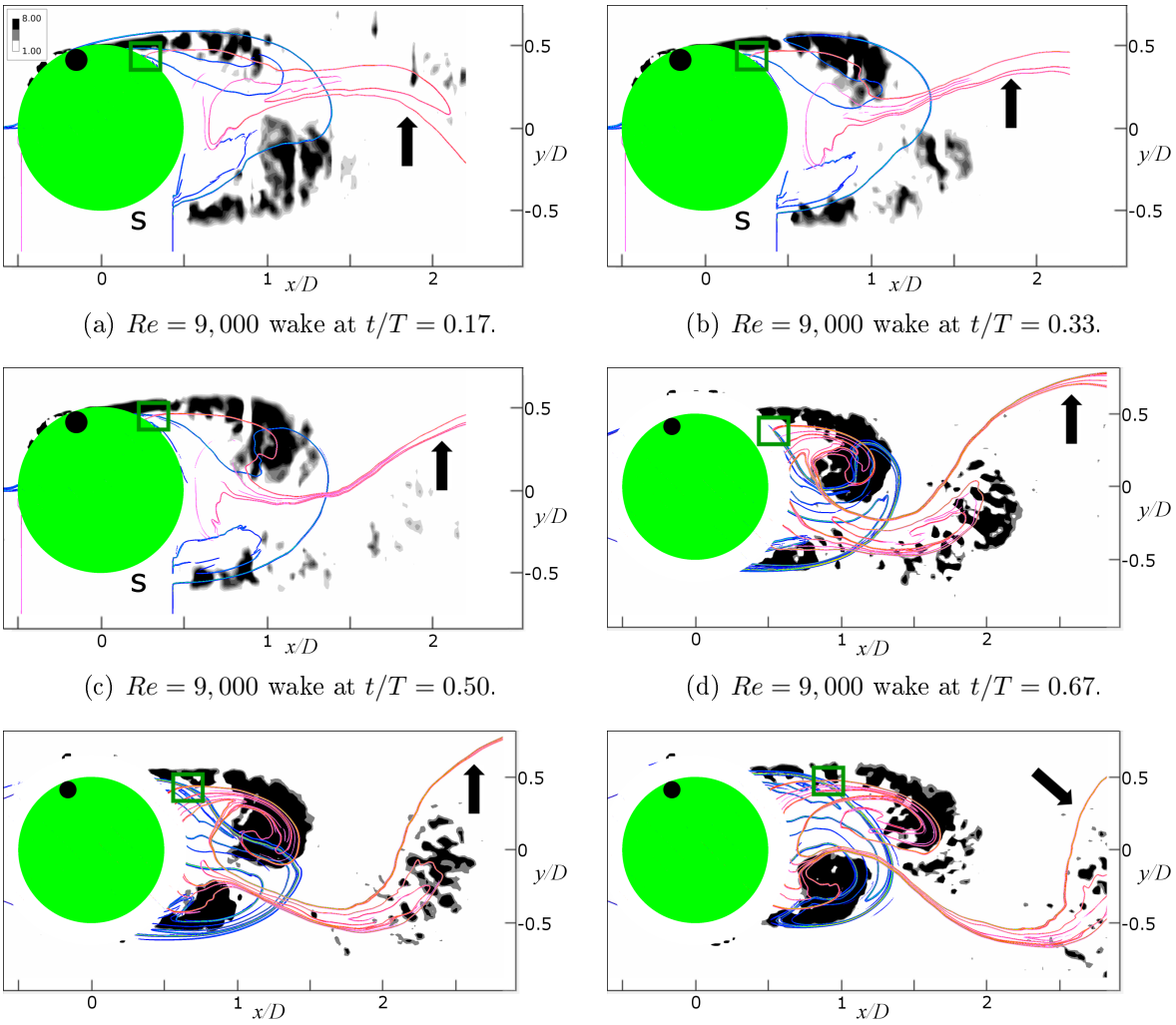

(a) $Re = 9,000$ wake at $t/T = 0.17$.

(b) $Re = 9,000$ wake at $t/T = 0.33$.

(c) $Re = 9,000$ wake at $t/T = 0.50$.

(d) $Re = 9,000$ wake at $t/T = 0.67$.

(e) $Re = 9,000$ wake at $t/T = 0.83$.

(f) $Re = 9,000$ wake at $t/T = 1.0$.

Figure 4-6: Wake visualization for $Re = 9,000$ with Q criterion (gray contours), nFTLE ridges (red), pFTLE ridges (blue), and cylinder (green). The Lagrangian saddle is located inside of the green box. The black arrow indicates the nFTLE ridge which is splitting the top and bottom half of the wake.

Experimental results at $Re = 9,000$ are shown in figure 4-6. Figures 4-6(a), 4-6(b), and 4-6(c) are from the supplemental case where only the near wake region was captured in an attempt to obtain Lagrangian saddle data that was missing from the initial $Re = 9,000$ case. Only one laser was available at the time so the cylinder shadow region below the cylinder, marked with a black "s", was not illuminated. Due to this, all nFTLE

values below the approximate centerline of the flow should be disregarded, since they are advected into the shadow region where there is no velocity information, resulting in incorrect results. A threshold of $Q = 0.01Q_{max}$ was used to highlight the vortex cores, while removing some of the erroneous regions caused by noise in the experimental data. Even with the increased Q threshold, there is still a significant amount of noise in the Q values, especially in regions farther downstream. Experimental data has larger amounts of noise than numerical data which is amplified by the spatial derivatives used in the calculation of Q, but the downstream dependency is likely also related to the larger variation in vortex position and coherence due to three-dimensional effects as the vortices convect downstream. The black circle located inside of the green cylinder is the location of the pressure tap used to measure the static pressure for phase-averaging. The white ring surrounding the cylinder in figures 4-6(d), 4-6(e), and 4-6(f) is the region obscured by the bottom of the cylinder during the larger window (far) PIV experiments.

The Lagrangian saddle upstream of the shedding vortex can be seen in throughout figure 4-6, and the pFTLE ridge can be seen splitting in figure 4-6(f). The overall structure of the FTLE ridges is similar to that of the constrained $Re = 400$ case, even with the missing portion of the domain. The Lagrangian saddle can be seen near the cylinder in figure 4-6(a), and then moving away from the cylinder before traveling downstream with the vortex in subsequent images. There is an nFTLE ridge that separates the top and bottom halves of the wake marked with a black arrow. This nFTLE ridge provides the justification for the validity of the top half of the FTLE results in the near case with a shadow below the cylinder (figures 4-6(a) through 4-6(c)). In the negative-time particle integration used for the nFTLE ridge calculation, the particles are advected backwards in time, so they travel upstream for most locations in the flow field. When these particles move into the shadow region with no velocity information, they remain there. Recalling that the FTLE ridges reveal material lines, this causes the majority of the particles that were initialized below the wake-splitting nFTLE ridge to advect to nearly the same location, resulting in low FTLE values. The particles above the wake-splitting nFTLE ridge are advected around the top surface of the cylinder, so they avoid the shadow region below the cylinder. Therefore, these trajectories are not subject to the same inaccuracy,

and the nFTLE ridge calculation for this portion of the flow field is still correct.

4.1.4 $Re = 19,000$

A main concern of the $Re = 19,000$ dataset was to fully resolve the flow around the circular cylinder, as well as to capture a large enough portion of the downstream domain to allow for accurate pFTLE calculations. Capturing the near-cylinder velocity fields allows for the visualization of the Lagrangian saddle behavior during the vortex formation process, and the downstream data allows for large enough separation to occur between FTLE particles before they leave the domain in the pFTLE calculation. Figure 4-7 shows that the overall FTLE and Q structure is very similar to the constrained $Re = 400$ FTLE, as well as the $Re = 9,000$ experimental case. The vortex feeding process through multiple lobes of pFTLE can again be seen during the vortex formation process in the top shear layer in figures 4-7(a) and 4-7(b) where a lobe is marked with a magenta asterisk and a red arrow. The splitting of the pFTLE ridge can be seen in figure 4-7(e) (black arrow), but the downstream pFTLE ridge is not visualized in figure 4-7(f) as it is below the plotting threshold. Figure 4-8 displays the image in figure 4-7(f) compared with a visualization of the wake with the pFTLE threshold lowered to 0.45FTLE_{max}. This shows that pFTLE ridge still exists, but is weaker than the ridges further upstream due to its proximity to the downstream boundary of the velocity domain. The particle integration for the pFTLE calculation advects the particles forward in time, resulting in particles leaving the downstream edge of the data window. When particles exit the window, they are advected by the freestream velocity only, so they do not separate any further, resulting in artificially low pFTLE values for particles initialized near the downstream data boundary compared to particles that were integrated through a larger part of the domain. The lower pFTLE threshold was not used in other images because it reduces the clarity of the wake visualization in the region just downstream of the cylinder.

One major difference between the numerical and experimental results is the location of the nFTLE ridge that is within the separated shear layer upstream of the forming vortex. In the numerical cases (figures 4-1 and 4-4) where the mean separation location, θ_s, was greater than 90° this ridge traveled nearly parallel to the freestream flow. In

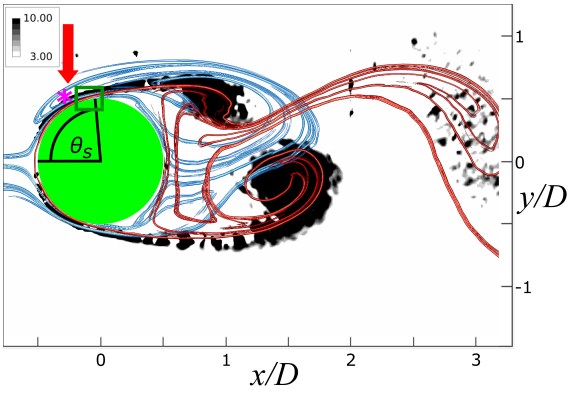

(a) $Re = 19,000$ wake at $t/T = 0.17$. The magenta asterisk and red arrow highlight a lobe that is being entrained into the forming vortex.

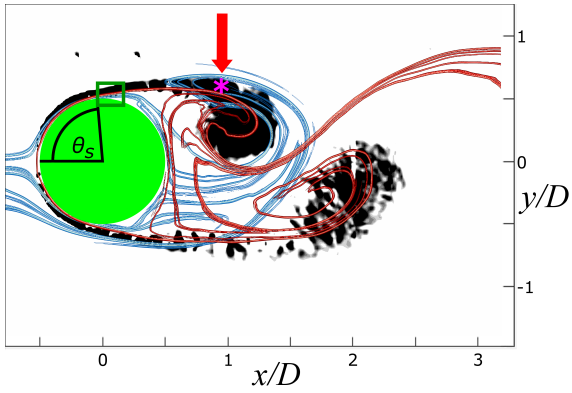

(b) $Re = 19,000$ wake at $t/T = 0.32$. The magenta asterisk and red arrow highlight a lobe that is being entrained into the forming vortex.

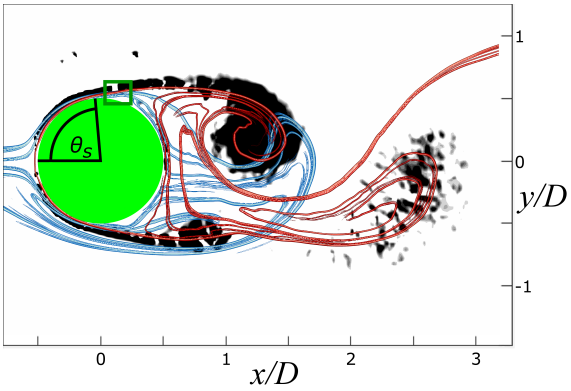

(c) $Re = 19,000$ wake at $t/T = 0.48$.

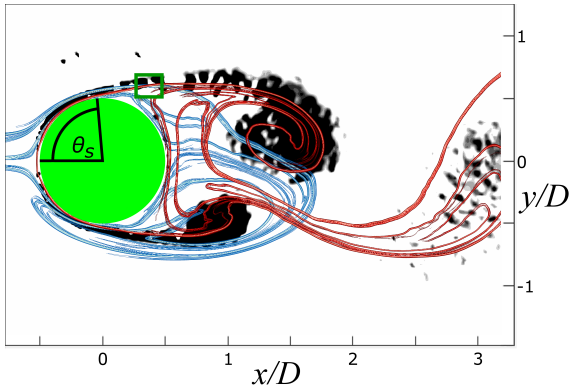

(d) $Re = 19,000$ wake at $t/T = 0.65$.

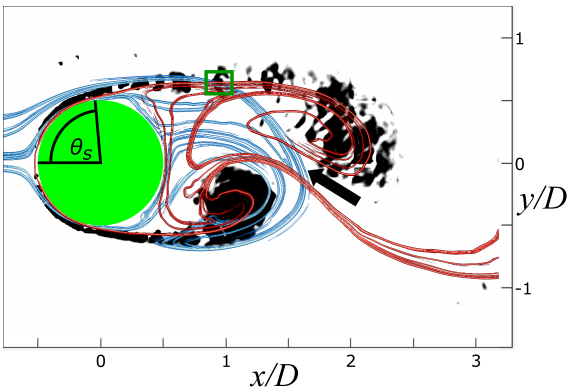

(e) $Re = 19,000$ wake at $t/T = 0.82$. The black arrow highlights the splitting pFTLE ridge.

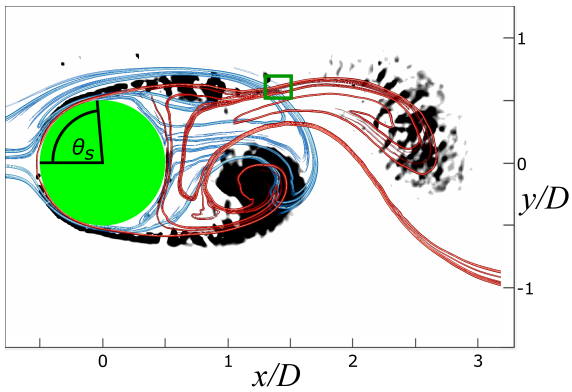

(f) $Re = 19,000$ wake at $t/T = 0.98$.

Figure 4-7: Wake visualization for $Re = 19,000$ with Q criterion (gray contours), nFTLE ridges (red), pFTLE ridges (blue), and cylinder (green). The Lagrangian saddle is located inside of the green box.

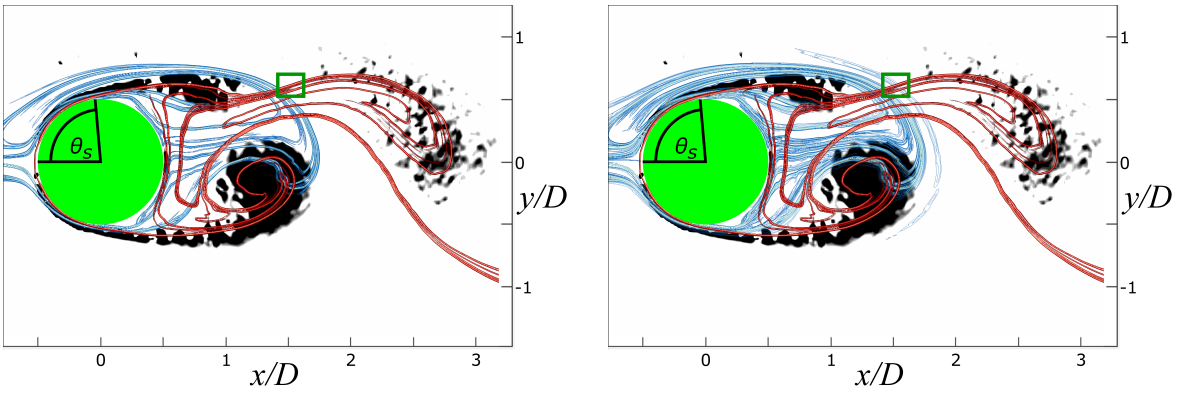

(a) $Re = 19,000$ wake at $t/T = 1.0$ with pFTLE threshold of 0.60FTLE_{max}.

(b) $Re = 19,000$ wake at $t/T = 1.0$ with pFTLE threshold of 0.45FTLE_{max}.

Figure 4-8: Wake visualization for $Re = 19,000$ with Q criterion (gray contours), nFTLE ridges (red), pFTLE ridges (blue), and cylinder (green). The Lagrangian saddle is located inside of the green box.

the experimental $Re = 19,000$ case, the separation angle is around 85° and the nFTLE ridge travels significantly further away from the wake centerline at an angle that is nearly tangent to the cylinder surface at the separation point. The Lagrangian saddle moves with this ridge, resulting in an increase in the distance away from the cylinder for the $Re = 19,000$ saddle track compared to the other cases where the nFTLE ridge is nearly parallel to the freestream flow near the separation location. This is discussed in more detail in section 4.2.

4.1.5 Comparison Among Cases

Figure 4-9 displays each case at approximately the same time in the shedding period. The timing of the numerical and experimental data sets were matched by visually comparing the scaled downstream wake organization. At this instant in time, across all cases, the vortex is in the process of shedding and the Lagrangian saddle is accelerating away from the cylinder. This time was chosen since it displays the similarities and differences between the cases clearly. There are many similarities between the different results, even across the range of Reynolds numbers presented. The Lagrangian saddle is located off the cylinder surface, between the shed vortex and the cylinder. There is a pFTLE ridge that

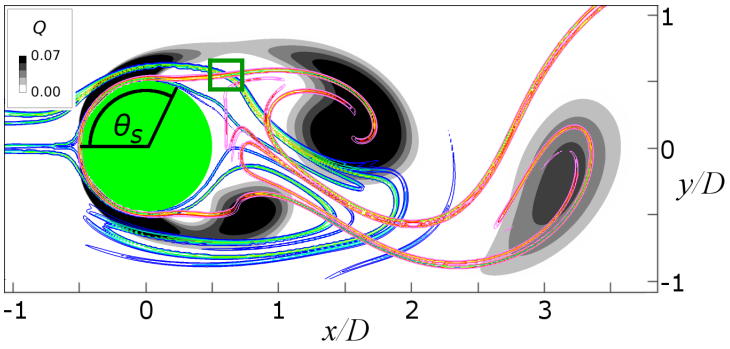

(a) $Re = 150$ wake at $t/T = 0.73$.

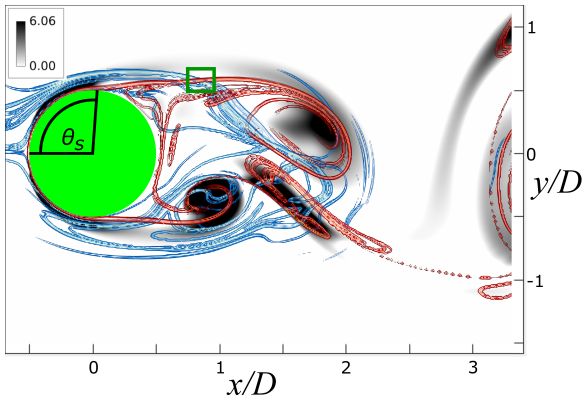

(b) $Re = 400$ full wake at $t/T = 0.72$.

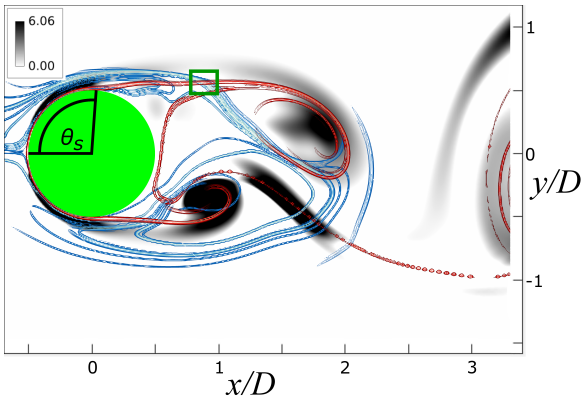

(c) $Re = 400$ constrained wake at $t/T = 0.72$.

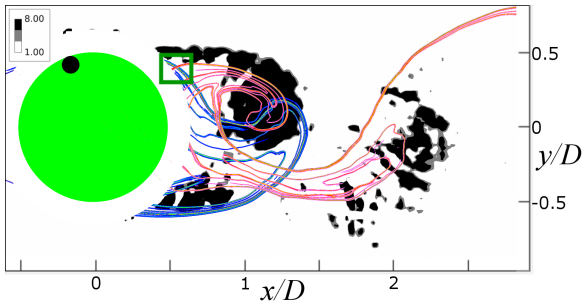

(d) $Re = 9,000$ wake at $t/T = 0.72$.

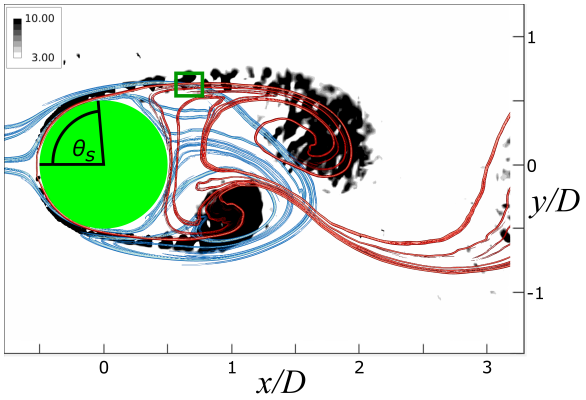

(e) $Re = 19,000$ wake at $t/T = 0.73$.

Figure 4-9: Wake comparison across all cases with Q criterion (gray contours), nFTLE ridges (red), pFTLE ridges (blue), and cylinder (green). The Lagrangian saddle is located inside of the green box.

separates the shear layer from the shed vortex (not visible in the $Re = 9,000$ case), which is splitting into multiple ridges. There are also some clear differences across the cases, mostly related to the location of the vortices and Lagrangian saddle, and the detail in the FTLE field. While each image is at roughly the same phase in the shedding process, the exact Lagrangian saddle location varies greatly from case to case. In the $Re = 150$, $Re = 9,000$, and $Re = 19,000$ cases, the Lagrangian saddle is located relatively close to the cylinder surface, between $0.5D$ and $0.7D$ downstream of the cylinder center. For both $Re = 400$ cases, the Lagrangian saddle is significantly further downstream, about $1D$ downstream of the cylinder center. This is related to the formation length of the vortices. $Re = 400$ has the largest formation length across the cases, meaning that the vortices roll-up further downstream. The FTLE fields in the $Re = 150$, and constrained $Re = 400$ cases are simpler, and contain fewer ridges than the other cases. In two-dimensional calculations, any out-of-plane movements of the FTLE particles during integration are not calculated, resulting in fewer regions that are dynamically distinct, and therefore fewer FTLE ridges. While the experimental results also used a two-dimensional calculation, they are at a significantly higher Reynolds number, and the turbulent fluctuations present in the wake increase the complexity of the FTLE field.

4.2 Lagrangian Saddle Locations

In each case, the location of the Lagrangian saddle found upstream of the vortex forming and shedding from the top half of the circular cylinder was tracked manually. The saddle track in time provides valuable insight into the shedding time of the von Kármán vortices for each of the cases investigated.

4.2.1 $Re = 150$

In the numerical two-dimensional $Re = 150$ case, the vortex center was tracked using the maximum Q value inside of the vortex core. Figure 4-10 displays the resulting track of the vortex center compared with the track of the Lagrangian saddle. The non-dimensional distance on the y-axis is measured from the location $(x/D, y/D) = (0, R)$, where R is the

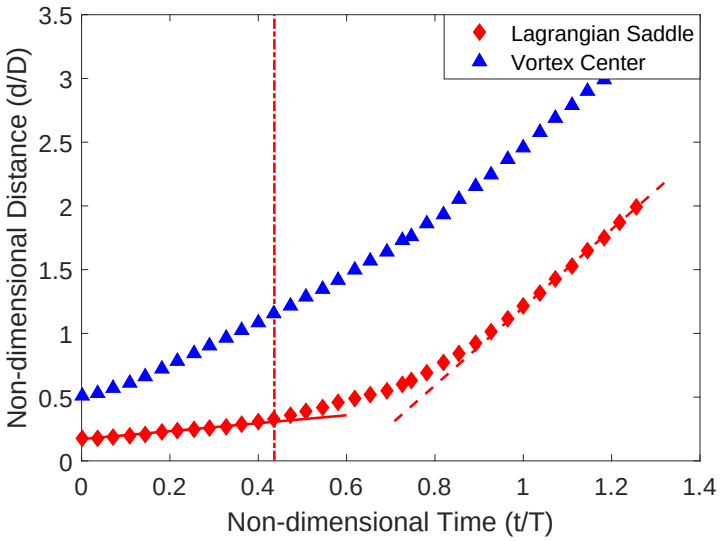

Figure 4-10: $Re = 150$ Lagrangian saddle and vortex tracks.

cylinder radius. This location was used as the origin of the distance measurement across all cases. The change in the location of the vortex center shows that as the vortex forms and sheds, there is a gradual increase in the distance away from the top of the cylinder with no clear indication as to when the vortex sheds. In contrast, as the vortex forms, the corresponding Lagrangian saddle remains nearly stationary near the cylinder surface. As the vortex sheds, the saddle lifts off and accelerates away from the cylinder surface at the time highlighted by the vertical dash-dot line in figure 4-10. This will be referred to as the vortex shedding time throughout this section, but formally, this is the beginning of the vortex shedding portion of the period. There is no singular time at which the vortex sheds, and the marked time indicates that the shedding is beginning.

A solid red line is fit to the near-zero motion of the saddle (red diamonds) at early times in the vortex shedding period, while the vortex is still attached and forming. The equation of this line was found by using a least-squares linear fit, and maximizing the R^2 value by varying the number of Lagrangian saddle locations considered. The slopes for each case are reported in section 4.2.5. Near $t/T = 0.44$, the saddle accelerates away from the cylinder surface, which is observed as the departure of the red diamonds from the solid red line. While there is no direct objective criterion for determining when the Lagrangian saddle has departed from the line, a consistent distance of $0.015d/D$ above

the solid line was used as the threshold for each case to determine if the Lagrangian saddle had shed. Once the Lagrangian saddle begins to accelerate, it will begin to move away from the cylinder at a higher speed than during vortex formation, which is seen by the saddle track increasing its slope in figure 4-10. The threshold value was set as low as possible, but still high enough to avoid the Lagrangian saddle location uncertainty. In contrast to the Lagrangian saddle acceleration, there is no distinct change in the speed of the vortex center found by the maximum Q value. Around $t/T = 0.90$, the vortex center has reached a constant velocity as it convects downstream. At the same time, the saddle finishes accelerating to its final velocity, shown by a dashed red line, which matches the speed of the vortex center. While the trace of the saddle location shows a dramatic change in slope, the trace of the vortex center has only a subtle continuous change in slope. Since this change in slope is small and based on instantaneous velocity field gradients, it would be sensitive to errors in the velocity field in experimental or three-dimensional data. In fact, the vortex center location cannot be located accurately in the current work using Q for the three-dimensional numerical or two-dimensional experimental flows. In the three-dimensional case at $Re = 400$, the vortex loses coherence as seen in figure 4-4(a), causing the track of maximum Q inside of the vortex to move erratically. The experimental cases have too much noise to accurately determine the location of maximum Q automatically from the velocity field. There are several maxima of various magnitudes clustered around the central portion of the vortex core.

4.2.2 $Re = 400$

Figure 4-11(a) displays the three-dimensional nFTLE field in the wake of the circular cylinder at $Re = 400$. The nFTLE ridges wrap around the vortices visualized by the Q isosurface in figure 4-2(a). A zoomed-in portion of the $Re = 400$ three-dimensional FTLE field is shown in figure 4-11(a). There is a distinct wavelength along the cylinder span present in the nFTLE field in the near-cylinder region shown in the figure, so the Lagrangian saddle behavior was investigated along $1.5D$ of the span to see how the saddle tracks varied. The analyzed tracks fall between the two transparent black planes in figure 4-11(a). This region contains 17 z/D planes, and about two of the nFTLE

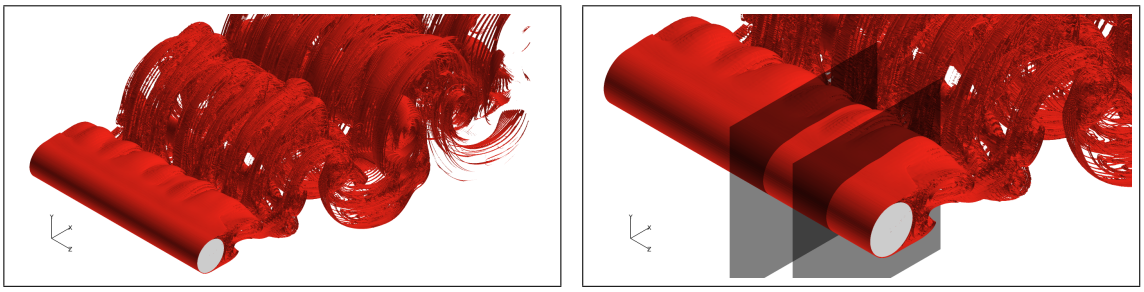

(a) Cylinder wake nFTLE ridges (red) and cylinder (grey).

(b) Zoomed in cylinder wake nFTLE ridges (red) and cylinder (grey).

Figure 4-11: $Re = 400$ three-dimensional nFTLE ridges at $t/T = 0.72$.

wavelengths. Figure 4-12(a) shows the Lagrangian saddle tracks for each z/D plane across this portion of the span. While there is some variation in the exact Lagrangian saddle location with span, all of the tracks follow the same trend in described in section 4.2.1 for the $Re = 150$ two-dimensional case. There is an initially slow movement of the Lagrangian saddle as the vortex forms, before a rapid acceleration as the vortex sheds. Eventually, the saddle settles onto the vortex convection speed.

Figure 4-12(b) displays the Lagrangian saddle tracks at $z/D = 3.72$ for the full and constrained FTLE cases. While there are large differences in the physics between the two cases, their Lagrangian saddle tracks are nearly identical, lending validity to our experimental results when using two-dimensional data to approximate the Lagrangian saddle behavior in a three-dimensional wake dominated by vortices aligned perpendicular to the FTLE plane. Figure 4-12(c) displays the mean Lagrangian saddle track for the z/D locations considered. Error bars indicate one standard deviation, which is minimal until well after the vortex has shed from the cylinder. The mean track is used for comparison to the other cases, as well as the determination of the shedding time as it is simpler to analyze, but was still calculated from the three-dimensional variation of the Lagrangian saddle tracks. The shedding time for this case occurs at $t/T = 0.36$, which is $0.08T$ earlier than the $Re = 150$ case, but still reasonably close.

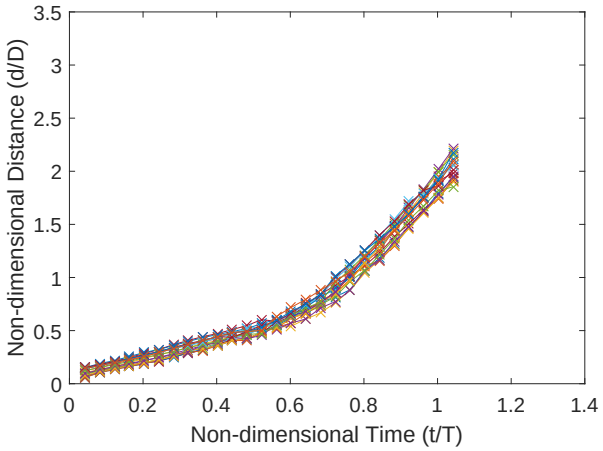

(a) Variation in Lagrangian saddle tracks along span ($\Delta z/D = 1.5$).

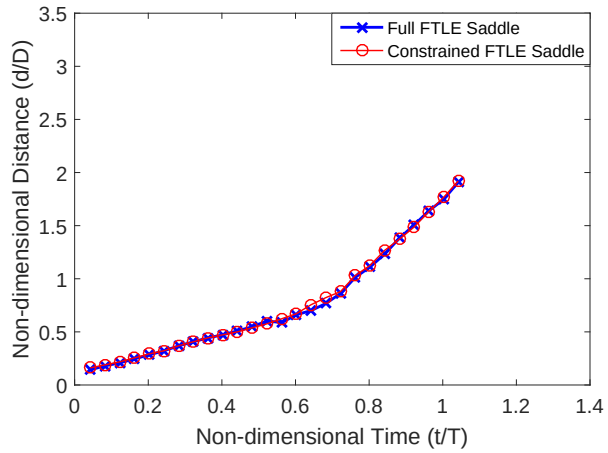

(b) Full vs. constrained Lagrangian saddle tracks for plane at $z/D = 3.72$.

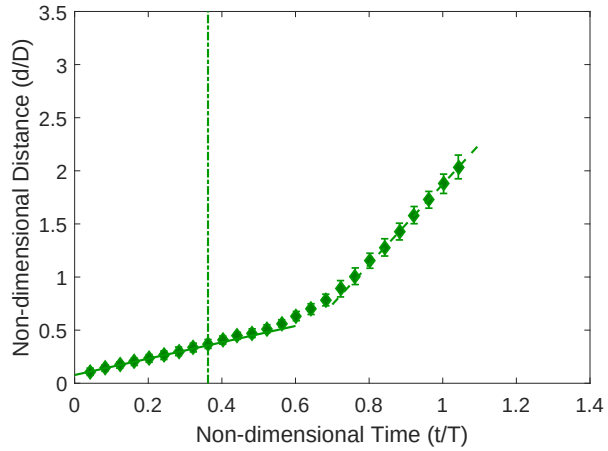

(c) Mean Lagrangian saddle track with error bars of 1σ.

Figure 4-12: $Re = 400$ Lagrangian saddle tracks.

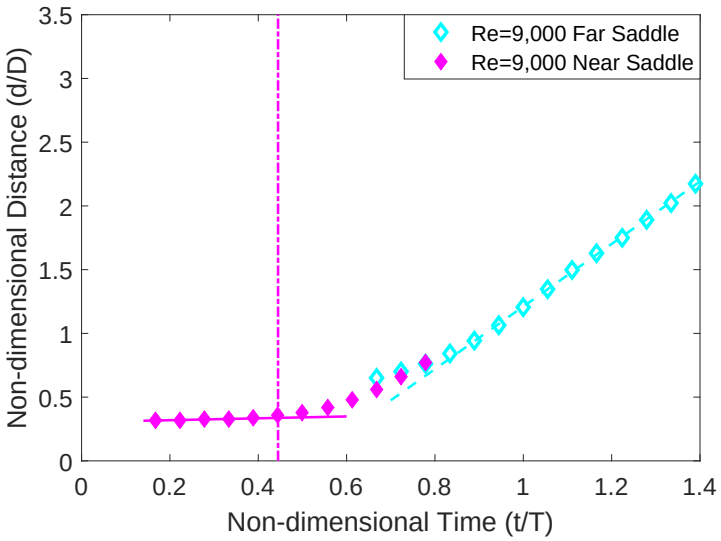

Figure 4-13: $Re = 9,000$ Lagrangian saddle tracks.

4.2.3 $Re = 9,000$

The Lagrangian saddle tracks for the $Re = 9,000$ case is shown in figure 4-13. The closed diamond magenta saddles that are closer to the cylinder are from the supplemental dataset used to resolve the near cylinder region. The two sets of data fit together well, with the near wake saddle locations transitioning well into the far wake locations. The Lagrangian saddle is essentially fixed as the vortex is forming in this case, and there is a clear acceleration away from the initial speed as the vortex sheds. The shedding time for this case occurs at $t/T = 0.44$, approximately the same as the $Re = 150$ case.

4.2.4 $Re = 19,000$

The Lagrangian saddle track for the $Re = 19,000$ case is shown in figure 4-14. Due to the nFTLE ridge arcing away from the wake centerline, the initial speed of the Lagrangian saddle is higher than the other cases during the vortex formation. In the other cases, the movement of the Lagrangian saddle is primarily in the streamwise direction, along the nFTLE ridge. In this case, the arcing of the nFTLE ridge adds a transverse component of movement to the saddle trace, increasing the total distance from the measurement location. There is still a clear acceleration of the vortex, and the shedding time for this case is $t/T = 0.61$.

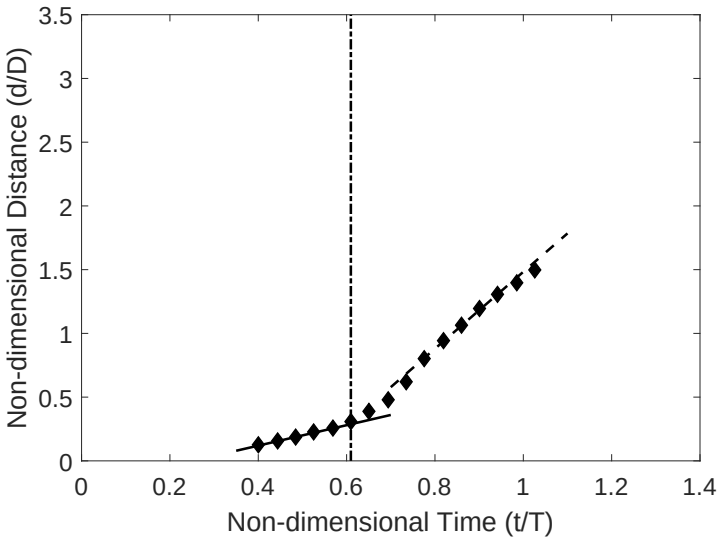

Figure 4-14: $Re = 19,000$ Lagrangian saddle track.

4.2.5 Comparison Among Cases

The Lagrangian saddle tracks across all cases are shown in figure 4-15. The timing (x-axis) of the numerical and experimental data sets were matched by visually comparing the scaled downstream wake organization, so there is some uncertainty associated with the x-axis locations for comparison among the cases. While there are considerable differences in the shedding time (vertical dash-dot line) and Lagrangian saddle speed during vortex formation across the four cases, the qualitative behavior of the saddles is similar. There is always a relatively low speed of the Lagrangian saddle during the vortex formation followed by a clear acceleration of the saddle before it eventually settles onto the vortex convection speed. There are some visual differences in the final slopes of the convecting portion of the Lagrangian saddle movement. The slopes of these lines are scaled by a factor of T/D due to the scaling of the data for comparison, so the slopes were multiplied by D/TU_∞ to scale the convection speed of the vortices by the freestream velocity. The Lagrangian saddle slopes and corrected speeds are shown in table 4.1. Formation slope refers to the slope of the line drawn through the Lagrangian saddles during vortex formation, saddle formation speed is the formation slope multiplied by D/TU_∞, and convection slope refers to the slope of the line drawn through the Lagrangian saddles during vortex convection. While there is considerable variation amongst the cases, the values

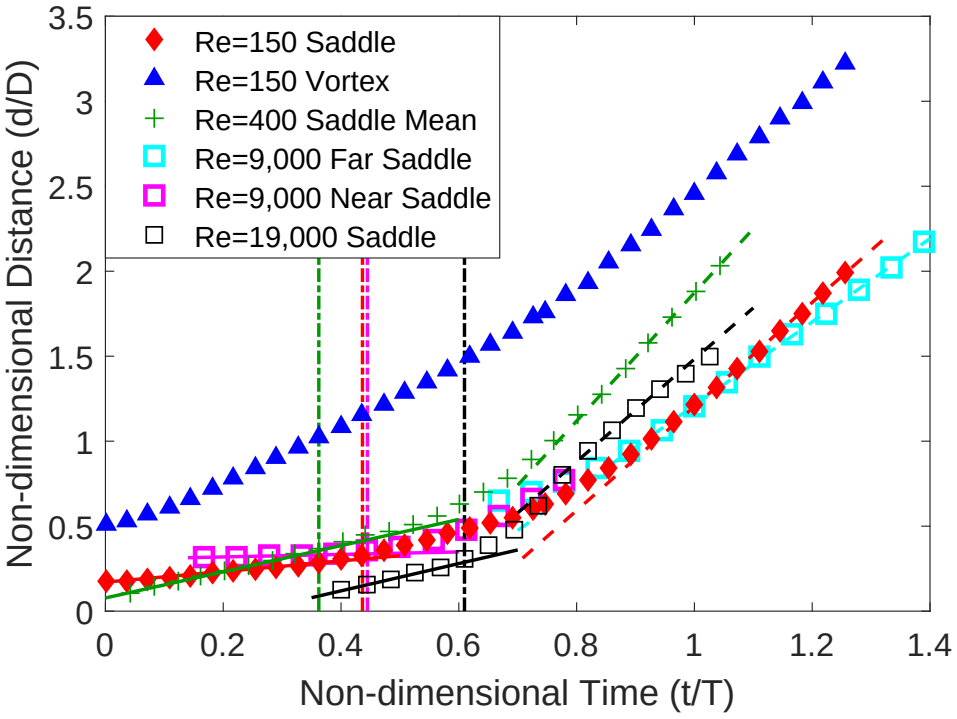

Figure 4-15: Lagrangian saddle tracks across all cases.

are reasonable according to Norberg and Sunden (1987), who stated that depending on the distance downstream, the vortex convection speed scaled by the freestream speed will vary between 0.5 and 0.75 as x/D increases from the formation length to 3.0 for a flow at $Re = 20,000$. While the $Re = 400$ case is at a significantly higher value for vortex convection speed in the near-wake region than the other cases, this may be due to the large difference in Reynolds number.

Re	Formation slope	Saddle formation speed	Convection slope	Vortex convection speed u_v/U_∞
150	0.31	0.06	3.1	0.56
400	0.77	0.16	3.8	0.78
9,000	0.07	0.02	2.5	0.52
19,000	0.80	0.17	3.0	0.65

Table 4.1: Slopes and vortex convection speed found from Lagrangian saddle tracks.

4.3 Pressure

The mean and fluctuating coefficient of pressure distributions are studied for the cases at Reynolds numbers of 150, 400, and 19,000. The mean coefficient of pressure distribution is used to estimate the separation location, and the fluctuating coefficient of pressure distribution is investigated in the vicinity of the vortex shedding time.

4.3.1 $\overline{C_p}$ Distributions

The mean coefficient of pressure ($\overline{C_p}$) distribution is used to determine the mean separation location of the flow around a circular cylinder, as well as to make comparisons among cases with different Reynolds numbers. The $\overline{C_p}$ distributions for $Re = 150$ and $Re = 400$ are shown in figure 4-16. The values for $Re = 400$ are for the z/D portion of the cylinder discussed section 4.2.2. There is little variation in $\overline{C_p}$ along the cylinder span, with the largest magnitude of variation occurring in the angular region higher than 130°. A zoomed in portion of the $\overline{C_p}$ distribution is shown in figure 4-16(c) to illustrate the small amount of variation along the span. The high $\overline{C_p}$ value at 0° in both cases is due to the mean stagnation point, and the $\overline{C_p}$ value decreases with increasing angular location as the flow accelerates around the cylinder surface. $\overline{C_p}$ reaches a minimum near 80° in each case before the flow begins to decelerate. This deceleration of the flow leads to flow separation, which occurs at the inflection point during the $\overline{C_p}$ increase. The mean separation point is at 115° for the $Re = 150$ case and at 94° for the $Re = 400$ case. While the $\overline{C_p}$ distribution was calculated for the $Re = 19,000$ case, the large change in the voltage bias throughout the testing procedure and extreme sensitivity of the coefficient of pressure to the exact pressure values rendered the $\overline{C_p}$ distribution invalid. The fluctuating coefficient of pressure distribution was not effected by this error, since the error was solely in the mean value at each location. The mean pressure at each location, and the error associated with it, is removed when the fluctuating coefficient of pressure distribution is calculated.

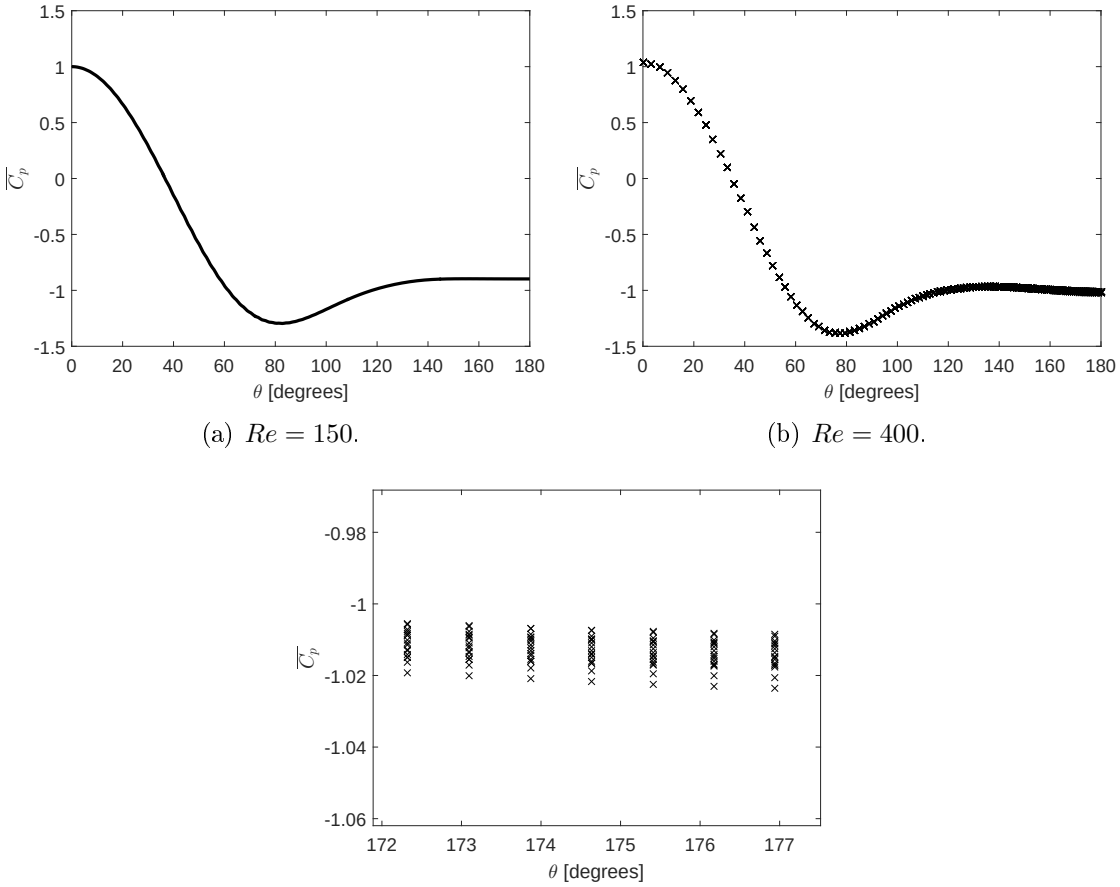

(a) $Re = 150$.

(b) $Re = 400$.

(c) $Re = 400$, zoomed in to show spanwise variation.

Figure 4-16: Numerical $\overline{C_p}$ distributions.

4.3.2 Lift and Circulation

When the instantaneous pressure distribution is integrated around the entire cylinder, the fluctuating lift and drag forces can be determined by decomposing the resultant forces into their streamwise (drag) and transverse (lift) components. This calculation is done to study the variation in the lift and drag, and how they relate to the vortex shedding time for the two numerical cases. Circulation is another commonly used analysis tool for studying vortex shedding, and is calculated around a von Kármán vortex for the $Re = 150$ case for comparison.

The timing of the Lagrangian saddle acceleration provides a clear indication of when the vortex sheds from a wake dynamics perspective, but further insight can be gained by comparing the shedding time with the fluctuating lift and drag experienced by the cylinder and the circulation of the shedding vortex. The fluctuating lift coefficient per unit span on the cylinder ($C'_L = L'/(0.5\rho_\infty U_\infty^2 D)$) was found by integrating the instantaneous static pressure distribution on the cylinder surface and calculating the fluctuating force component per unit span in the vertical direction, L'. The fluctuating drag coefficient per unit span was calculated using the same method, but instead used the horizontal component of the force. Results from this calculation are displayed in figure 4-17, where it is observed that the maximum fluctuating coefficient of lift is approximately 0.5, which agrees with previously published work (Inoue and Hatakeyama, 2002). The vortex shedding time inferred from the Lagrangian saddle lift off ($t/T = 0.44$) is shown in figure 4-17 by the vertical dash-dot line. This time indicates the initial shedding of the vortex, and here is shown to correspond to the maximum fluctuating lift. After this time the vortex begins convecting downstream, so it has a decreased effect on the cylinder pressure distribution. There is a maximum in fluctuating drag just after the vortex begins to shed, indicating that the vortex has a lingering effect on the pressure distribution near the downstream ($\theta = 180°$) portion of the cylinder, which is closer to the vortex.

Vortex separation and shedding can be described as a process in which the shear layer stops feeding circulation to the forming vortex, and the vortex does not pinch-off until it reaches its maximum circulation (Ringuette et al., 2007). The time to maximum

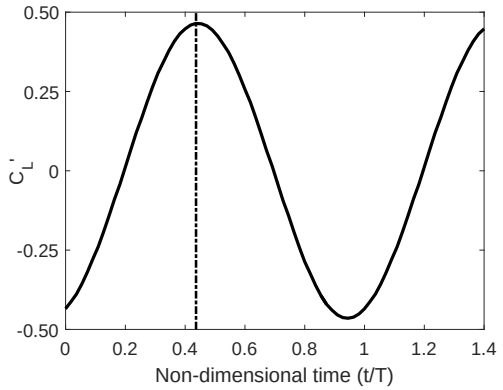

(a) $Re = 150$ fluctuating coefficient of lift.

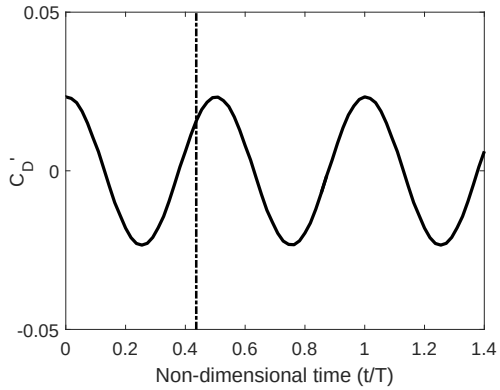

(b) $Re = 150$ fluctuating coefficient of drag.

Figure 4-17: $Re = 150$ force coefficients.

circulation of a forming vortex has been referred to as the formation time (Rosenfeld et al., 1998), and there is evidence that there may be a universal range of formation times in the vicinity of 4, for flow fields such as piston-generated vortex rings (Rosenfeld et al., 1998), pitching flat plates (Milano and Gharib, 2005), circular cylinders started from rest (Jeon and Gharib, 2004), and biological flows such as jellyfish propulsion (Dabiri, 2009). The circulation of the vortex forming and shedding from the upper cylinder surface was calculated using two different areas, and is shown in figure 4-18 for comparison with the lift history and Lagrangian shedding time. The first bounding box for the circulation was determined by locating the distance from the vortex center to the contour of $0.01Q_{max}$ in the downstream and transverse (down in figure 4-19) directions, and using that as the distance to the respective rectangular box boundary in each direction. This bounding box enclosed the boundaries of the vortex, defined by $0.01Q_{max}$, and cut out the majority of the shear layer when the vortex was near the cylinder, as shown by the green box in figure 4-19. This was done intentionally to avoid the variable effect of the shear layer as the vortex and corresponding circulation area travel downstream. The circulation values, shown by the green triangles in figure 4-18, are smaller than those found by Green and Gerrard (1993). When the circulation area is made large enough to include the majority of the shear layer, the value for maximum circulation is above 1.0, and is comparable to Green and Gerrard (1993). This is shown with the red box in figure 4-19, and the

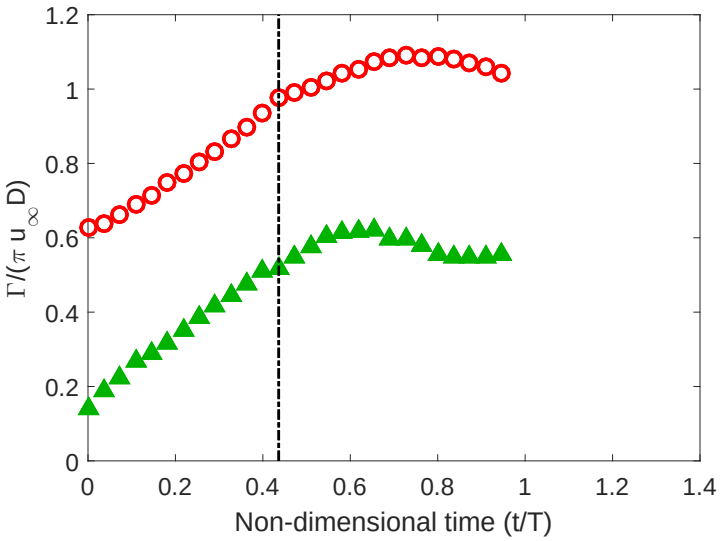

Figure 4-18: $Re = 150$ circulation for two different areas.

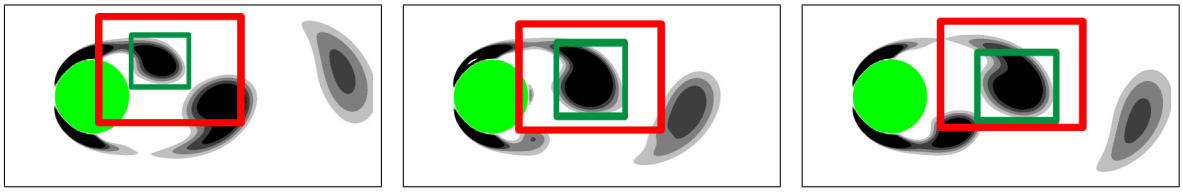

(a) $t/T = 0.29$. (b) $t/T = 0.58$. (c) $t/T = 0.78$.

Figure 4-19: $Re = 150$ circulation areas used.

resulting time-history of circulation in this area is shown as the red open circular symbols in figure 4-18. These results demonstrate the dependence of the circulation calculation on the size and shape of the bounding box.

Figure 4-18 shows that the times of maximum circulation ($t/T = 0.65$ and $t/T = 0.73$) are later than the shedding time found by the Lagrangian saddle departure ($t/T = 0.44$). It is interesting to note that by including more of the shear layer, the time of peak circulation is even later after the peak in lift. It is difficult to determine the exact time at which the shear layer stops feeding the vortex using a quantity such as the Q criterion, as the contours are determined by a user selected threshold. An integrated calculation of circulation shows when the shear layer stops feeding the vortex more clearly, but while this information is useful for understanding the flow physics, it is still not a good method for determining the shedding time of the vortex due to its reliance on user-defined

boundaries and its propensity to include portions of nearby shear layers. Tracking the Lagrangian saddle acceleration is not subject to the same user decisions about calculation area or thresholds, and is shown here to correspond with the extrema in vertical force.

The fluctuating sectional coefficients of lift and drag for $z/D = 3.72$ in the $Re = 400$ case are shown in figure 4-20. Figure 4-20(a) shows a similar trend to that found in figure 4-17(a), with the positive lift force increasing as the vortex induces low pressure along the upper surface of the cylinder as it grows in size and strength. The vortex shedding time found by the Lagrangian saddle corresponds to the time one phase after the maximum value in the fluctuating lift force. This small discrepancy between the maximum lift and the vortex shedding time may be related to the increased formation distance, or inaccuracy in the determination of the vortex shedding time. The fluctuating drag also reaches its maximum near the vortex shedding time, but slightly after the vortex begins to shed. The jump in C'_L and C'_D that occurs around $t/T = 0.55$ is due to the FTLE and pressure data available for the Lagrangian saddle and C'_L calculations, respectively. The continuous period of data that was available encompassed the formation and shedding of a vortex from the lower surface of the cylinder. During that period, a formed vortex shed from the top half of the cylinder near the beginning of the period, and a new vortex formed from the top shear layer near the end of the period. Since the previous investigation focused on the vortex forming and shedding from the top half of the vortex, the available period of data was cut in half, and then the two portions were switched in time. By doing that, the period of data begins with the formation of the vortex from the top shear layer, then leads to the shedding and convection of this vortex, as in the other cases. Due to this rearrangement of the data files, the original period's final and initial data files are now in the middle of the rearranged shedding period. Since this is a fully three-dimensional flow, the final flow field and the initial flow field are not identical, but they are close enough that the difference in lift and saddle locations are not egregious. Conversely, a full sequential set of $1.5T$ was used for the calculation of each FTLE field.

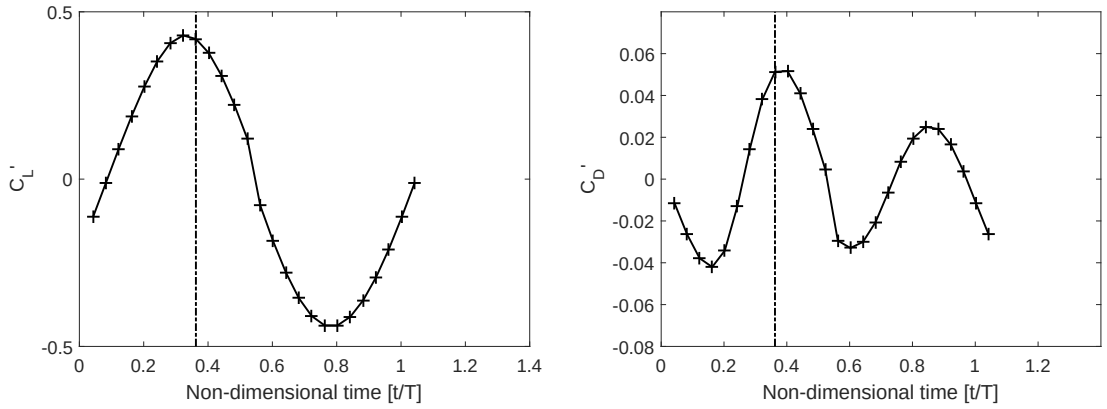

(a) $Re = 400$ fluctuating sectional coefficient of lift.

(b) $Re = 400$ fluctuating sectional coefficient of drag.

Figure 4-20: $Re = 400$ fluctuating sectional force coefficients for $z/D = 3.72$.

4.3.3 Fluctuating C_p vs. θ and vortex shedding time

While the coefficient of lift has a maximum at or near the vortex shedding time, it can be prohibitive to instrument a surface with enough pressure taps to accurately calculate lift on-the-fly. A force transducer could measure the lift, but is impractical to implement in real world applications. For this reason, the distribution of the fluctuating coefficient of pressure on the cylinder surface was investigated to determine if the time-evolution of the surface pressure at any location had a distinctive feature at the liftoff time of the Lagrangian saddle. Figure 4-21 displays the time history of fluctuating coefficient of pressure at multiple angular locations along the cylinder surface for the three cases with available pressure data. The fluctuating coefficient of pressure is calculated by subtracting the mean from the total coefficient of pressure at each location. This allows the variation of pressure at multiple angular locations to be easily compared on a common set of axes, and avoids any errors in the $\overline{C_p}$ calculation for the experimental case. The vertical dash-dot line in each figure indicates the time at which the Lagrangian saddle, and therefore the vortex, begins to shed from the cylinder. As the angular location increases from the region near the upstream stagnation point (0°) the magnitude of the pressure fluctuations increases, with the peak fluctuation magnitude at the region just upstream of the mean separation location in each case. The mean separation location

(θ_s) is 115° for the $Re = 150$ case, 94° for the $Re = 400$ case, and about 85° for the $Re = 19,000$ case. The peak fluctuations occurred at 100°, 80°, and 75°, respectively. These large fluctuations are due to the von Kármán vortices, and are the justification for installing the phase-averaging pressure taps in this location in the experiments.

In the $Re = 150$ and $Re = 400$ cases, the pressure upstream of the mean separation locations reaches its minimum after the shedding time of the vortex for angular locations much lower than the mean separation location. For an angular location approximately 15° upstream of the mean separation location there is a minimum in pressure as the Lagrangian saddle begins to shed. Angular locations further along the cylinder surface from this point reach their pressure minimum at a time earlier than the vortex shedding time. This relationship implies that these regions could be targeted with pressure taps to inform closed-loop flow control applications on the behavior of the von Kármán vortices. The region just upstream of the von Kármán vortices has a large, consistent signal from the von Kármán vortices and can be relied on to provide useful information for flow control.

The $Re = 19,000$ case yields a slightly different result. While the trend of the minimum pressure value occurring at earlier times in the period as angular location increases still holds, the location 15° upstream of the mean separation location no longer has a minimum in pressure at the time of vortex shedding. The mean separation location for this case is near 85°, so the 75° pressure tap was expected to have its minimum in pressure very close to the vortex shedding time. While this is only 10° upstream of the mean separation location, it is the location closest to 15° that was available. Instead, the 75° location has a minimum in pressure $0.1T$ earlier than the vortex shedding time.

There are a number of small errors, as well as some physical differences in the flow field that likely contributed to this discrepancy. There is always finite error in the velocity fields acquired from PIV, although the FTLE calculation is relatively insensitive to these, as explained in section 3.1.3. There may be some phase-averaging inaccuracies due to using a pressure tap that is offset from the PIV plane for phase averaging. While this offset is constant for both the pressure and PIV data, there may be some phase-averaging errors due to a non-constant phase shift along the span. There are also some

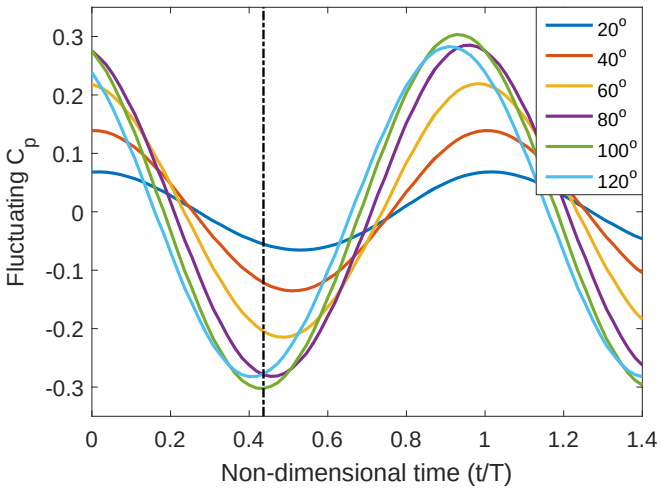

(a) $Re = 150$, numerical. $\theta_s = 115^{\circ}$.

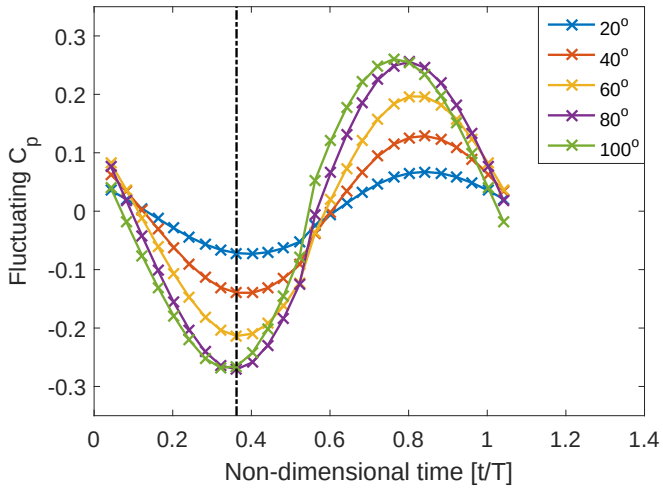

(b) $Re = 400$, numerical. $\theta_s = 94^{\circ}$.

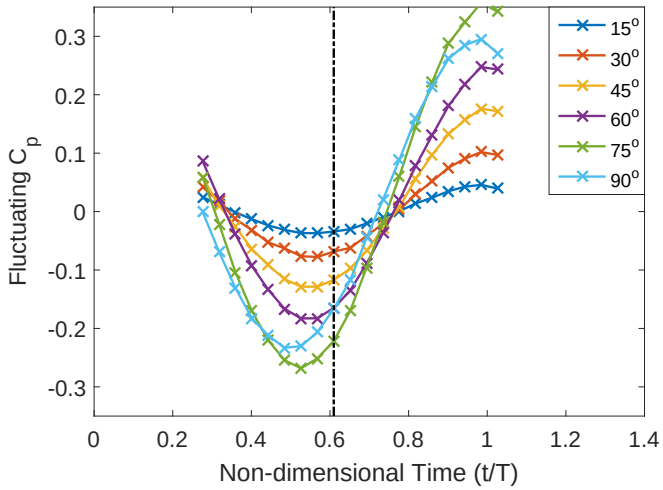

(c) $Re = 19,000$, experimental. $\theta_s = 85^{\circ}$.

Figure 4-21: Fluctuating C_p for a range of θ.

physical changes in the flow between the $Re = 400$ case and the $Re = 19,000$ case. In the $Re = 19,000$ case there are three-dimensional structures in the flow on the scale of the shear layer vortices, and the von Kármán vortices are not shedding parallel to the cylinder. While much of this is averaged out by the phase-averaging process, the combination of the three-dimensional effects and the phase-averaging inaccuracies due to the non-constant phase lag between the PIV measurement plane and the pressure signal measurement location for phase-averaging are the likely culprits of this finite lag time between the minimum pressure time at the 75° location and the vortex shedding time. More extensive testing at a variety of Reynolds numbers with a modified geometry would be required to conclusively determine the reason for the difference between the cases.

Chapter 5

Concluding Remarks

The locations of Lagrangian saddles found from finite-time Lyapunov exponent (FTLE) fields were used to determine an objective vortex shedding time for circular cylinder wakes. The FTLE field calculation used both experimentally and numerically generated velocity fields over a range of Reynolds numbers from 150 to 19,000. The vortex shedding time was compared to the cylinder lift, vortex circulation, and cylinder static pressure distribution to determine the best method for detecting this vortex shedding time using widely available sensors.

5.1 Conclusions

An investigation into the flow around a circular cylinder using both numerically and experimentally generated velocity data found that the FTLE field yielded new insight into the dynamics of the von Kármán vortices shed in the near-wake region. While traditional Eulerian techniques, such as the Q criterion, have proven useful for locating vortex cores in a range of two-dimensional and three-dimensional flow fields, the Lagrangian FTLE objectively locates transport boundaries in the flow field, yielding new insight on the changes in the structure of the flow field as the von Kármán vortices form and shed in the cylinder wake. An FTLE analysis allowed for the identification of fluid packets being entrained into a forming vortex, and the conditions under which the upper and lower portions of the cylinder wake remain distinct from one another, even several diameters

downstream. Lagrangian saddles were located from the intersections of positive-time and negative-time FTLE ridges, and tracking their location determined that a Lagrangian saddle accelerates away from the cylinder surface at the shedding time of the associated vortex. This shedding time was compared with the shedding time determined by the force history and the vortex circulation. The force history agreed well with the Lagrangian saddle shedding time in the numerical cases, as a maximum in lift force occurred at or very near the vortex shedding time found by the Lagrangian saddle. The vortex circulation maxima occurred at times that did not correspond to the vortex shedding time, instead the maximum circulation values occurred significantly later in the shedding process.

While the Lagrangian saddle dynamics elucidate the physical dynamics of vortex trajectories, they cannot directly be determined in real-time. To address this, the time-resolved static pressure distribution on a circular cylinder was used to find a relationship between the pressure on the cylinder surface and the behavior of the Lagrangian saddles. Across two-dimensional and three-dimensional simulation data, the surface static pressure 15° upstream of the mean separation point was found to reach its minimum just as the vortex was shed from the cylinder, indicated by the Lagrangian saddle beginning to accelerate away from the cylinder surface. A similar relationship was found from two-dimensional results generated experimentally, but the minimum in pressure occurred $0.1T$ earlier than the vortex shedding time found by the Lagrangian saddle, and was measured at a location 10° upstream of the mean separation location. This relationship makes possible the detection of vortex shedding, described objectively by the Lagrangian saddle motion, simply using common sensors at or around a particular angular location. Some current closed-loop flow control methods already use pressure to inform control algorithms, but the minimum in pressure at a specific location has not been previously linked to an objective vortex shedding time, which is realizable by tracking the Lagrangian saddle found from intersections of FTLE ridges. Data acquired from a few specifically placed pressure sensors could then be used to inform closed-loop flow control around bluff bodies, deploy high-lift devices to prevent stall, or to inform fuel injection levels in a mixing application.

5.2 Recommendations for Future Work

While the current body of work determined a method to detect the location and evolution of von Kármán vortices in the wake of a circular cylinder, there is still further understanding that could be gained from the continuation of this research. There is still uncertainty about the lag between the pressure minimum and the vortex shedding time in the experimental results. Is it a physical change due to the increase in Reynolds number, or is it merely caused by an accumulation of experimental errors? Further work to improve the phase-averaging algorithm could help reduce these experimental errors, but another study using sensors with higher sensitivity at a range of other Reynolds number would be necessary to truly determine if the lag was physical. Another method that could help reduce the errors from the current analysis procedure would be to use a PIV system with a higher resolution in both space and time. A higher temporal resolution, greater than about 12 Hz, would allow for the abandonment of the phase-averaging scheme entirely, and allow for the FTLE fields to be calculated directly from time-resolved PIV velocity fields. An increase in spatial resolution would also improve the FTLE fields, as it would allow for more accurate flow map calculations, as well as further refinement of the cylinder boundary, and the velocities close to the wall. Pressure sensors with a higher sensitivity are not available for measurements in water, but measurements could be conducted in a low-speed wind tunnel, allowing for the application of a larger variety of pressure transducers, including smaller transducers that would allow for an increased angular resolution in the pressure distribution. This could also open up a different range of Reynolds numbers that could be used to further verify the current results. Additional numerical studies at Reynolds numbers closer to the experimental Reynolds numbers could also help answer the question about the finite lag between the minimum pressure upstream of the mean separation location and the time of vortex shedding found by the Lagrangian saddle. Numerical simulations at Reynolds numbers on the order of a few thousand require a highly resolved three-dimensional grid to capture the small-scale turbulent fluctuations, resulting in a long computation time, so our collaborators were unable to provide us with simulation data near the experimental Reynolds numbers.

The next steps in the current research would be to integrate the current results into a closed-loop flow control system. The first step would be to implement the system in a numerical simulation to determine effective control strategies using the vortex shedding time and its relationship with the static pressure distribution. Suction and blowing systems would affect the pressure distribution on the cylinder, and could cause the Lagrangian saddle and associated von Kármán vortex to shed earlier or later, depending on whether a reduction or enhancement of vortex shedding was desired. These systems would be most effective at changing the separation location on the cylinder surface, which could be used to vary the frequency and size of the von Kármán vortices. Ultimately, an experimental study using numerically-effective techniques would allow the control techniques to be tested across multiple Reynolds numbers to determine if they could improve upon the current state of the art in flow control.

Appendices

Appendix A

PIV Uncertainty

Errors in the exact location of PIV particles can have a significant effect on the velocity vectors calculated using cross-correlations. These errors can arise from multiple sources, such as particle image diameter, particle image displacement, background noise, and flow gradients as discussed in Raffel et al. (2013). In the current analysis, 16×16 pixel interrogation areas were used to calculate the instantaneous velocity vector fields, and the particle image diameter was 2 pixels. Each of the following errors are r.m.s. uncertainties calculated using the simulation results provided in Chapter 5.5 of Raffel et al. (2013).

The error in the particle location based on the particle image diameter is 0.06 pixels. The amount of time between each image pair was chosen such that the mean distance traveled by the PIV particles in the domain was approximately 4 pixels. While Raffel et al. (2013) does not contain information on a particle displacement errors for a 16×16 pixel interrogation area, the 4 pixel displacement for a 32×32 pixel interrogation area was assumed to be the most similar, and the error related to that displacement is 0.02 pixels. A conservative estimate of the background noise error for a 32×32 pixel interrogation area is 0.03 pixels, assuming that the background noise could be approximated as white noise with a magnitude 10% or less of the image dynamic range.

The largest source of error in the current results is due to the velocity gradients present in the flow field. The wakes of bluff bodies experiencing vortex shedding contain regions with high velocity gradients, with the largest magnitudes present in the separated shear layer. The maximum velocity difference between two neighboring velocity vectors was

0.050 m/s in the $Re = 9,000$ case, and 0.097 m/s in the $Re = 19,000$ case. The gradients were calculated to be 0.18 pixels per pixel and 0.24 pixels per pixel, respectively. These gradients caused errors of 0.6 pixels and 1.0 pixel. In regions outside of the shear layer, the gradients were significantly lower in both cases, resulting in errors on the order of 0.08 pixels or lower in the rest of the flow field. The total error in pixel location for the $Re = 9,000$ case was 0.19 pixels in the shear layer, and less than 0.11 pixels in the rest of the flow field. The particle location error magnitude for the $Re = 19,000$ case was 1.0 pixel in the shear layer, and 0.11 pixels for the rest of the flow field. When these errors are divided by the 4 pixel movement of the particles, the velocity vector error for the $Re = 9,000$ case is 4.8% inside of the shear layer, and 2.8% or lower in the rest of the flow field. For the $Re = 19,000$ case, the error in the velocity vector is 25% inside of the shear layer, and 2.8% or lower in the rest of the velocity field.

While a maximum velocity error of 25% is significant, it is important to consider that this error is highly localized to the narrow shear layer region in the cylinder wake. Only a few velocity vectors are subject to an error of this magnitude, and the simulated particles used in the FTLE calculation would only experience one of these erroneous vectors at one time in the particle integration, which would not have a large effect on the final particle location. Another reason this error is not of great concern is that the FTLE ridges in the shear layers are nearly parallel to the freestream flow. Since the largest velocity gradients are in the freestream component of velocity, the large errors would also be isolated to that component, making it nearly impossible for an error to be large enough to "push" one of the FTLE particles across the FTLE ridge into a dynamically different region of the flow, resulting in an incorrect FTLE ridge location.

Appendix B

Comparison Between $Re = 9,000$ and $Re = 10,000$ Velocity Data

The wake behind a circular cylinder undergoes minimal changes between $Re = 9,000$ and $Re = 10,000$. Mean and phase-averaged vorticity and velocity fields are shown in this appendix to display the similarities between the two cases. The cylinder diameter was the same for each case, so the freestream velocity was increased from 151 mm/s to 168 mm/s. The mean vorticity (ω), streamwise velocity (u), and transverse velocity (v) fields are shown in figure B-1. There is an increase in the overall magnitude of streamwise velocity from $Re = 9,000$ to $Re = 10,000$, but the mean vorticity and velocity fields are nearly identical otherwise.

Phase-averaged vorticity and velocity fields at the same phase are shown in figure B-2. The overall structure of the flow is similar between the two cases. The formation length, or distance downstream that the vortices form is slightly lower in the $Re = 10,000$ case, which is noticeable in the location the negatively-signed von Kármán vortex is forming in figures B-2(a) and B-2(b). In the $Re = 10,000$ case, the von Kármán vortex is slightly closer to the cylinder as it forms. The difference in formation length over this range of Reynolds numbers is minimal, and has little effect on the overall wake structure. Other than the slight change in vortex location due to the decreased formation length, the vorticity and velocity fields are nearly identical, and the Lagrangian saddle behavior is assumed to be approximately the same.

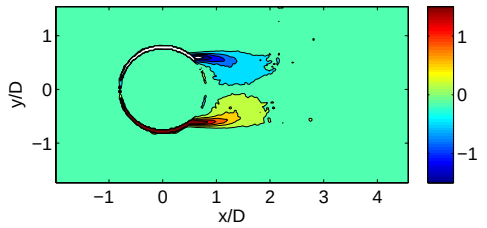

(a) $Re = 9,000$ mean ω.

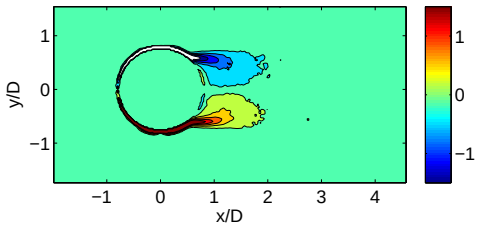

(b) $Re = 10,000$ mean ω.

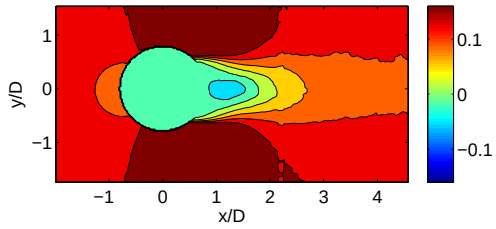

(c) $Re = 9,000$ mean u.

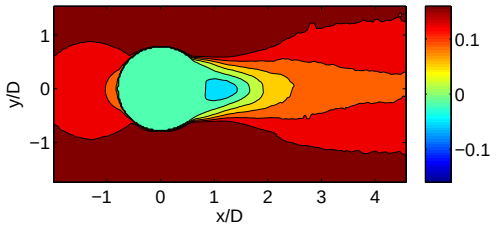

(d) $Re = 10,000$ mean u.

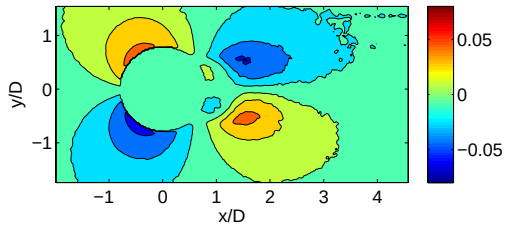

(e) $Re = 9,000$ mean v.

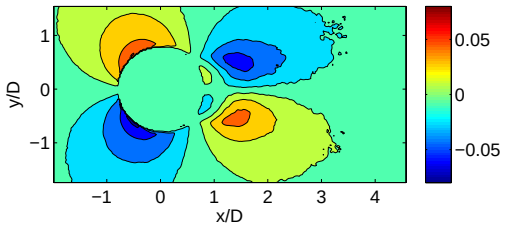

(f) $Re = 10,000$ mean v.

Figure B-1: Mean spanwise vorticity (ω), streamwise velocity (u), and transverse velocity (v) contours for $Re = 9,000$ (left) and $Re = 10,000$ (right).

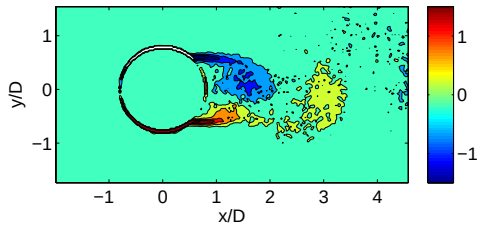

(a) $Re = 9,000$ phase-averaged ω.

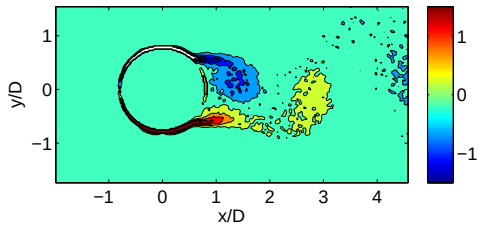

(b) $Re = 10,000$ phase-averaged ω.

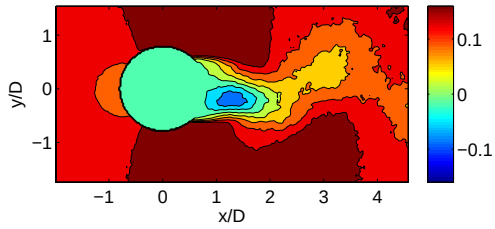

(c) $Re = 9,000$ phase-averaged u.

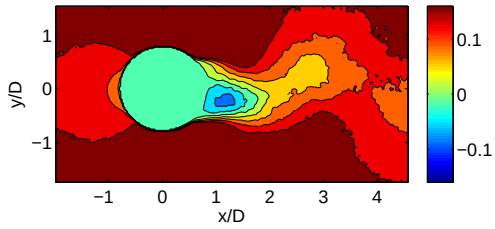

(d) $Re = 10,000$ phase-averaged u.

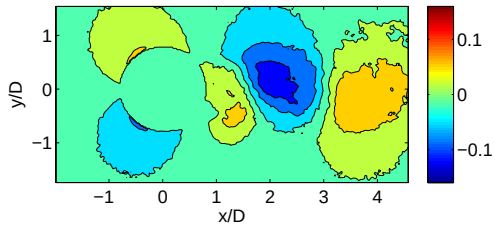

(e) $Re = 9,000$ phase-averaged v.

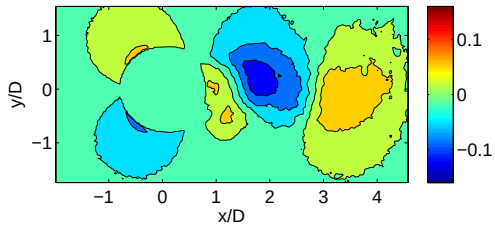

(f) $Re = 10,000$ phase-averaged v.

Figure B-2: Phase-averaged vorticity (ω), streamwise velocity (u), and transverse velocity (v) contours for $Re = 9,000$ (left) and $Re = 10,000$ (right).

Appendix C

Code Used

MATLAB and Fortran 90 were used extensively for the calculation of FTLE fields, phase-averaging, velocity field stitching, and analysis of the resulting data. Fieldview was used to generate wake visualization images. All codes used are available on http://greenfluids.syr.edu/, and a list of the files and a short description for each is included below.

C.1 Fortran 90 codes

General codes

1. intprog.f90: Top-level code to integrate trajectories and calculate FTLE fields.
2. grid.f90: Read in input parameters and set up FTLE grid.
3. inout.f90: All input and output subroutines.
4. ftlecalc.f90: Particle integration, FTLE calculation, and velocity field interpolation.
5. Makefile: File used to compile all modules at once.
6. ftle.inp: Input parameters, usually located in a subfolder.

***Re* = 150 specific codes**

1. dataconvert.f90: Converts data from 2D structured cylindrical grid to a 2D structured rectangular grid.

$Re = 400$ specific codes

1. dataconvert.f90: Organizes connectivity data from Tecplot for interpolation.

2. zonebin.f90: Organizes cells from numerical simulation into "zones" based on their spatial location in the 3D unstructured grid.

3. interpset.f90: Determines interpolation constants for the 3D unstructured grid.

4. velinterp.f90: Interpolates velocity files from 3D unstructured grid onto 3D structured rectangular grid.

C.2 MATLAB codes

General codes

1. avgu_new.m: Calculates mean u and v velocity and standard deviation. Plots u, v, and vorticity.

2. saddlefind_ftle.m: Visualizes pFTLE+nFTLE field for locating Lagrangian saddles at the intersection of ridges.

3. saddleanalysis_ExpNum.m: Contains Lagrangian saddle locations for all cases. Plots Lagrangian saddle traces.

$Re = 150$ specific codes

1. ForceCalc.m: Calculates coefficients of lift and drag over a period of pressure data. Plots C_L and C_D.

2. SaddlePressureCorrelation.m: Calculates mean, instantaneous, and fluctuating coefficient of pressure distributions. Plots the above distributions.

3. CirculationCalc.m: Calculates circulation for two different vortex areas. Plots circulation results.

4. saddle_traj_plots_good.m: Reads in trajectories from FTLE code (fortran) and colors them in the vicinity of the saddle point. Plots the particle evolution in the vicinity of a Lagrangian saddle.

$Re = 400$ specific codes

1. velconvert.m: Reads in wake data from numerical simulation, and converts it to ASCII velocity data.

2. PressureAnalysis.m: Calculates mean and fluctuating coefficient of pressure distributions, and lift and drag coefficients. Plots the above distributions and values.

3. saddleanalysis.m: Contains Lagrangian saddle locations along a portion of the span for 3D FTLE, and saddle locations for 1 constrained FTLE plane. Plots saddle traces.

$Re = 9,000$ specific codes

1. PhaseAnglePlot.m: Generates phase angle plot for comparison between POD and pressure phase-averaging techniques.

2. PressureAnalysis_wcalibration.m: Determines calibration curve. Calculates average power spectral density, and Wiener filter. Filters the pressure data to remove noise. Plots calibration curve, power spectral density, and filtered data example.

3. PIVtriggerPull_Re09k.m: Reads in filtered pressure data and PIV trigger voltage signal. Determines phase angle of each velocity field and phase-averages data.

4. PODanalysis09k.m: Uses proper orthogonal decomposition to determine phase angle and phase-averages data.

5. cyl_windowstitching_wlinfit_1_2015.m: Reads in two PIV generated velocity fields and stitches them together.

6. cylUSwDS_Press_windowstitching_11_2014.m: Stitches together windows from different downstream locations that were previously stitched with

cyl_windowstitching_wlinfit_1_2015.m code. This is for data phase-averaged with pressure signal.

7. cyl_windowstitchingUSDS_wlinfit_1_2015.m: Stitches together windows from different downstream locations that were previously stitched with cyl_windowstitching_wlinfit_1_2015.m code. This is for data phase-averaged with POD.

8. TurbIntensityCalc.m: Adapted from avgu_new.m code to also calculate turbulence intensity from freestream data.

$Re = 19,000$ specific codes

1. CalConstants.m: Calculates calibration constants for six simultaneously sampled channels.

2. PressureFilteringRe19k.m: Using Wiener filter to reduce noise in the pressure signal. Plots power spectral density plot and noise reduction example.

3. PressPhaseAveraging_Re19k.m: Phase averages velocity data using pressure signal. Plots phase angle plot.

4. PressSignalPhaseAveraging_Re19k_new.m: Calculates mean and fluctuating coefficient of pressure distributions. Plots the distributions and the phase angles. Also plots radial coefficient of pressure versus spatial location of Lagrangian saddle plots.

5. cyl_stitching_USp30_10_2016.m: Stitches upstream window of velocity data from PIV.

6. cyl_stitching_DS1_10_2016.m: Stitches first downstream window of velocity data from PIV.

7. cyl_stitching_DS2_10_2016.m: Stitches second downstream window of velocity data from PIV.

8. cyl_stitching_USp30toDS1_10_2016.m: Stitches upstream and first downstream stitched velocity fields together after phase-averaging.

9. cyl_stitching_USp30andDS1toDS2_10_2016.m: Stitches the second downstream phase-averaged velocity fields with the rest of the domain.

C.3 Fieldview code

General code

1. ImageGen_Close.fvx Uses a formatting restart file to generate images with the same formatting for a number of data files.

Bibliography

Achenbach, E. (1968), 'Distribution of local pressure and skin friction around a circular cylinder in cross-flow up to Re= 5×10^6', Journal of Fluid Mechanics **34**(04), 625–639.

Adrian, R., Christensen, K. and Liu, Z. (2000), 'Analysis and interpretation of instantaneous turbulent velocity fields', Experiments in fluids **29**(3), 275–290.

Allshouse, M. R. and Peacock, T. (2015), 'Refining finite-time Lyapunov exponent ridges and the challenges of classifying them', Chaos: An Interdisciplinary Journal of Nonlinear Science **25**(8), 087410.

Allshouse, M. R. and Thiffeault, J.-L. (2012), 'Detecting coherent structures using braids', Physica D: Nonlinear Phenomena **241**(2), 95–105.

Artana, G., Sosa, R., Moreau, E. and Touchard, G. (2003), 'Control of the near-wake flow around a circular cylinder with electrohydrodynamic actuators', Experiments in Fluids **35**, 580–588.

Baarholm, G., Larsen, C. and Lie, H. (2006), 'On fatigue damage accumulation from in-line and cross-flow vortex-induced vibrations on risers', Journal of Fluids and Structures **22**(1), 109 – 127.

Batham, J. (1973), 'Pressure distributions on circular cylinders at critical Reynolds numbers', Journal of Fluid Mechanics **57**(02), 209–228.

Beron-Vera, F. J. (2010), 'Mixing by low- and high-resolution surface geostrophic currents', Journal of Geophysical Research: Oceans **115**(C10).

Beron-Vera, F., Olascoaga, M. and Goni, G. (2008), 'Oceanic mesoscale eddies as revealed by Lagrangian coherent structures', Geophysical Research Letters **35**.

Blazevski, D. and Haller, G. (2014), 'Hyperbolic and elliptic transport barriers in three-dimensional unsteady flows', Physica D: Nonlinear Phenomena **273**, 46–62.

Blevins, R. D. (1977), 'Flow-induced vibration', New York, Van Nostrand Reinhold Co., 1977. 377 p. **1**.

Bourgeois, J., Sattari, P. and Martinuzzi, R. (2012), 'Coherent vortical and straining structures in the finite wall-mounted square cylinder wake', International Journal of Heat and Fluid Flow **35**, 130 – 140. 7th Symposium on Turbulence & Shear Flow Phenomena (TSFP7).

Braza, M., Chassaing, P. and Minh, H. H. (1986), 'Numerical study and physical analysis of the pressure and velocity fields in the near wake of a circular cylinder', Journal of Fluid Mechanics **165**, 79–130.

Bres, G. A., Nichols, J. W., Lele, S. K. and Ham, F. E. (2012), 'Towards best practices for jet noise predictions with unstructured large eddy simulations', Cell **1**, M2.

Brunton, S. L. and Rowley, C. W. (2010), 'Fast computation of finite-time Lyapunov exponent fields for unsteady flows', Chaos: An Interdisciplinary Journal of Nonlinear Science **20**(1), 017503.

Catalano, P., Wang, M., Iaccarino, G., Sbalzarini, I. F. and Kuomoutsakos, P. (2002), Optimization of cylinder flow control via actuators with zero net mass flux, in 'Center for Turbulence Research, Proceedings of the Summer Program'.

Chakraborty, P., Balachandar, S. and Adrian, R. J. (2005), 'On the relationships between local vortex identification schemes', Journal of Fluid Mechanics **535**, 189–214.

Chong, M., Perry, A. and Cantwell, B. (1990), 'A general classification of three-dimensional flow fields', Physics of Fluids **2**, 765–777.

Coutanceau, M. and Defaye, J.-R. (1991), 'Circular cylinder wake configurations: A flow visualization survey', Applied Mechanics Reviews **44**(6), 255–305.

Dabiri, J. O. (2009), 'Optimal vortex formation as a unifying principle in biological propulsion', Annual Review of Fluid Mechanics **41**(1), 17–33.

Dabiri, J. O. and Gharib, M. (2004), 'Fluid entrainment by isolated vortex rings', Journal of Fluid Mechanics **511**, 311–331.

Dong, S., Triantafyllou, G. S. and Karniadakis, G. E. (2008), 'Elimination of vortex streets in bluff-body flows', Phys. Rev. Lett. **100**, 204501.

du Toit, P. and Marsden, J. (2010), 'Horseshoes in hurricanes', Journal of Fixed Point Theory and Applications **7**, 351–384.

Dubief, Y. and Delcayre, F. (2000), 'On coherent-vortex identification in turbulence', Journal of turbulence **1**(1), 011–011.

Eldredge, J. and Chong, K. (2010), 'Fluid transport and coherent structures of translating and flapping wings', Chaos **20**.

Fey, U., König, M. and Eckelmann, H. (1998), 'A new Strouhal-Reynolds-number relationship for the circular cylinder in the range $47 < \mathrm{Re} < 2 \times 10^5$', Physics of Fluids **10**(7), 1547–1549.

Froyland, G., Santitissadeekorn, N. and Monahan, A. (2010), 'Transport in time-dependent dynamical systems: Finite-time coherent sets', Chaos: An Interdisciplinary Journal of Nonlinear Science **20**(4).

Gerrard, J. (1978), 'The wakes of cylindrical bluff bodies at low Reynolds number', Philosophical Transactions of the Royal Society of London A: Mathematical, Physical and Engineering Sciences **288**(1354), 351–382.

Gerrard, J. H. (1966), 'The mechanics of the formation region of vortices behind bluff bodies', Journal of Fluid Mechanics **25**, 401–413.

Graftieaux, L., Michard, M. and Grosjean, N. (2001), 'Combining PIV, POD and vortex identification algorithms for the study of unsteady turbulent swirling flows', Measurement Science and Technology **12**(9), 1422.

Green, M., Rowley, C. and Smits, A. (2010), 'Using hyperbolic Lagrangian coherent structures to investigate vortices in bioinspired fluid flows', Chaos **20**.

Green, M., Rowley, C. and Smits, A. (2011), 'The unsteady three-dimensional wake produced by a trapezoidal pitching panel', Journal of Fluid Mechanics **685**, 117–145.

Green, R. and Gerrard, J. (1993), 'Vorticity measurements in the near wake of a circular cylinder at low Reynolds numbers', Journal of Fluid Mechanics **246**, 675–691.

Griffin, O. M. (1995), 'A note on bluff body vortex formation', Journal of Fluid Mechanics **284**, 217–224.

Haller, G. (2001), 'Distinguished material surfaces and coherent structures in three-dimensional fluid flows', Physica D **149**, 248–277.

Haller, G. (2002), 'Lagrangian coherent structures from approximate velocity data', Physics of Fluids **14**(6), 1851.

Haller, G. (2005), 'An objective definition of a vortex', Journal of Fluid Mechanics **525**, 1–26.

Haller, G. (2011), 'A variational theory of hyperbolic Lagrangian coherent structures', Physica D: Nonlinear Phenomena **240**(7), 574–598.

Haller, G. (2015), 'Lagrangian coherent structures', Annual Review of Fluid Mechanics **47**(1), 137–162.

Haller, G. and Beron-Vera, F. J. (2012), 'Geodesic theory of transport barriers in two-dimensional flows', Physica D: Nonlinear Phenomena **241**(20), 1680 – 1702.

Haller, G. and Beron-Vera, F. J. (2013), 'Coherent Lagrangian vortices: the black holes of turbulence', Journal of Fluid Mechanics **731**.

Haller, G., Hadjighasem, A., Farazmand, M. and Huhn, F. (2016), 'Defining coherent vortices objectively from the vorticity', Journal of Fluid Mechanics **795**, 136–173.

Haller, G. and Sapsis, T. (2011), 'Lagrangian coherent structures and the smallest finite-time Lyapunov exponent', Chaos **21**(023115).

Hernández-Carrasco, I., López, C., Hernández-García, E. and Turiel, A. (2011), 'How reliable are finite-size Lyapunov exponents for the assessment of ocean dynamics?', Ocean Modeling **36**(3), 208 – 218.

Hill, M. J. M. (1894), 'On a spherical vortex', Philosophical Transactions of the Royal Society of London. (A.) **185**, 213–245.

Huang, Y. and Green, M. A. (2015), Eulerian and Lagrangian methods for detecting vortex formation and shedding, in 'AIAA Science and Technology Forum'.

Hunt, J., Wray, A. and Moin, P. (1988), Eddies, streams, and convergence zones in turbulent flows, in 'Center for Turbulence Research, Proceedings of the Summer Program'.

Inoue, O. and Hatakeyama, N. (2002), 'Sound generation by a two-dimensional circular cylinder in a uniform flow', Journal of Fluid Mechanics **471**, 285–314.

Jeon, D. and Gharib, M. (2004), 'On the relationship between the vortex formation process and cylinder wake vortex patterns', Journal of Fluid Mechanics **519**, 161–181.

Jeong, J. and Hussain, F. (1995), 'On the identification of a vortex', Journal of Fluid Mechanics **285**, 69–94.

Jukes, T. N. and Choi, K.-S. (2009), 'Flow control around a circular cylinder using pulsed dielectric barrier discharge surface plasma', Physics of Fluids **21**(8), 084103.

Karrasch, D. and Haller, G. (2013), 'Do finite-size Lyapunov exponents detect coherent structures?', Chaos: An Interdisciplinary Journal of Nonlinear Science **23**(4).

Keating, S. R., Smith, K. S. and Kramer, P. R. (2011), 'Diagnosing lateral mixing in the upper ocean with virtual tracers: Spatial and temporal resolution dependence', Journal of Physical Oceanography **41**(8), 1512–1534.

Khalighi, Y., Ham, F., Moin, P., Lele, S. K. and Schlinker, R. H. (2011), Noise prediction of pressure-mismatched jets using unstructured Large Eddy Simulation, in 'ASME 2011 Turbo Expo: Turbine Technical Conference and Exposition', American Society of Mechanical Engineers, pp. 381–387.

Khalighi, Y., Nichols, J. W., Lele, S., Ham, F. and Moin, P. (2011), 'Unstructured large eddy simulation for prediction of noise issued from turbulent jets in various configurations', AIAA paper **2886**, 2011.

Kourentis, L. and Konstantinidis, E. (2011), 'Uncovering large-scale coherent structures in natural and forced turbulent wakes by combining PIV, POD, and FTLE', Experiments in Fluids **52**(3), 749–763.

Kriegseis, J., Kinzel, M. and Rival, D. E. (2013), 'On the persistence of memory: do initial conditions impact vortex formation?', Journal of Fluid Mechanics **736**, 91–106.

Lee, S.-J., Lim, H.-C., Han, M. and Lee, S. S. (2005), 'Flow control of circular cylinder with a v-grooved micro-riblet film', Fluid Dynamics Research **37**(4), 246 – 266.

Lei, P., Zhang, J., Li, K. and Wei, D. (2015), 'Study on the transports in transient flow over impulsively started circular cylinder using Lagrangian coherent structures', Communications in Nonlinear Science and Numerical Simulation **22**(1), 953–963.

Leung, S. (2011), 'An Eulerian approach for computing the finite time Lyapunov exponent', Journal of Computational Physics **230**(9), 3500–3524.

Leung, S. (2013), 'The backward phase flow method for the Eulerian finite time Lyapunov exponent computations', Chaos: An Interdisciplinary Journal of Nonlinear Science **23**(4), 043132.

Lim, H.-C. and Lee, S.-J. (2004), 'Flow control of a circular cylinder with o-rings', Fluid Dynamics Research **35**(2), 107 – 122.

Lipinski, D. and Mohseni, K. (2010), 'A ridge tracking algorithm and error estimate for efficient computation of Lagrangian coherent structures', Chaos: An Interdisciplinary Journal of Nonlinear Science **20**(1).

Milano, M. and Gharib, M. (2005), 'Uncovering the physics of flapping flat plates with artificial evolution', Journal of Fluid Mechanics **534**, 403–409.

Miron, P. and Vétel, J. (2015), 'Towards the detection of moving separation in unsteady flows', Journal of Fluid Mechanics **779**, 819–841.

Miron, P., Vétel, J. and Garon, A. (2015), 'On the flow separation in the wake of a fixed and a rotating cylinder', Chaos **25**(8).

Mulleners, K. and Raffel, M. (2011), 'The onset of dynamic stall revisited', Experiments in Fluids **52**(3), 779–793.

Mulleners, K. and Raffel, M. (2012), 'The onset of dynamic stall revisited', Experiments in fluids **52**(3), 779–793.

Nishimura, H. and Taniike, Y. (2001), 'Aerodynamic characteristics of fluctuating forces on a circular cylinder', Journal of Wind Engineering and Industrial Aerodynamics **89**(7–8), 713 – 723. 10th International Conference on Wind Engineering.

Norberg, C. (1986), 'Interaction between freestream turbulence and vortex shedding for a single tube in cross-flow', Journal of Wind Engineering and Industrial Aerodynamics **23**, 501–514.

Norberg, C. (2003), 'Fluctuating lift on a circular cylinder: review and new measurements', Journal of Fluids and Structures **17**(1), 57 – 96.

Norberg, C. and Sunden, B. (1987), 'Turbulence and reynolds number effects on the flow and fluid forces on a single cylinder in cross flow', Journal of Fluids and Structures **1**(3), 337 – 357.

O'Farrell, C. and Dabiri, J. O. (2014), 'Pinch-off of non-axisymmetric vortex rings', Journal of Fluid Mechanics **740**, 61–96.

Olcay, A. B., Pottebaum, T. S. and Krueger, P. S. (2010), 'Sensitivity of Lagrangian coherent structure identification to flow field resolution and random errors', Chaos: An Interdisciplinary Journal of Nonlinear Science **20**(1), 017506.

Onoue, K. and Breuer, K. S. (2016), 'Vortex formation and shedding from a cyber-physical pitching plate', Journal of Fluid Mechanics **793**, 229–247.

Oudheusden, B. W. v., Scarano, F., Hinsberg, N. P. v. and Watt, D. W. (2005), 'Phase-resolved characterization of vortex shedding in the near wake of a square-section cylinder at incidence', Experiments in Fluids **39**(1), 86–98.

Perrin, R., Braza, M., Cid, E., Cazin, S., Barthet, A., Sevrain, A., Mockett, C. and Thiele, F. (2007), 'Obtaining phase averaged turbulence properties in the near wake of a circular cylinder at high Reynolds number using POD', Experiments in Fluids **43**(2-3), 341–355.

Perrin, R., Braza, M., Cid, E., Cazin, S., Moradei, F., Barthet, A., Sevrain, A. and Hoarau, Y. (2006), 'Near-wake turbulence properties in the high Reynolds number incompressible flow around a circular cylinder measured by two- and three-component PIV', Flow, Turbulence, and Combustion **77**, 185–204.

Perry, A. E., Chong, M. S. and Lim, T. T. (1982), 'The vortex-shedding process behind two-dimensional bluff bodies', Journal of Fluid Mechanics **116**, 77–90.

Poje, A. C., Haza, A. C., Özgökmen, T. M., Magaldi, M. G. and Garraffo, Z. D. (2010), 'Resolution dependent relative dispersion statistics in a hierarchy of ocean models', Ocean Modeling **31**(1), 36 – 50.

Press, W. H., Teukolsky, S. A., Vetterling, W. T. and Flannery, B. P. (2007), Numerical recipes 3rd edition: The art of scientific computing, Cambridge University Press.

Raben, S. G., Ross, S. D. and Vlachos, P. P. (2014), 'Computation of finite-time Lyapunov exponents from time-resolved particle image velocimetry data', Experiments in Fluids **55**(1), 1–14.

Raffel, M., Willert, C. E., Wereley, S. and Kompenhans, J. (2013), Particle image velocimetry: a practical guide, Springer.

Rempel, E. L., Chian, A. C.-L., Brandenburg, A., Muñoz, P. R. and Shadden, S. C. (2013), 'Coherent structures and the saturation of a nonlinear dynamo', Journal of Fluid Mechanics **729**, 309–329.

Ringuette, M. J., Milano, M. and Gharib, M. (2007), 'Role of the tip vortex in the force generation of low-aspect-ratio normal flat plates', Journal of Fluid Mechanics **581**, 453–468.

Rockwood, M. P. and Green, M. A. (2015), An analysis of the unsteady wake behind a circular cylinder using Lagrangian coherent structures, in 'AIAA Science and Technology Forum'.

Rockwood, M. P. and Green, M. A. (2016), Correlation of the surface pressure distribution on a circular cylinder with objective identification of vortex formation and shedding, in 'AIAA Science and Technology Forum'.

Rockwood, M. P., Morrida, J. and Green, M. A. (2014), An analysis of the unsteady wake behind a circular cylinder using Lagrangian coherent structures, in 'AIAA Science and Technology Forum'.

Rockwood, M. P., Taira, K. and Green, M. A. (2016), 'Detecting vortex formation and shedding in cylinder wakes using Lagrangian coherent structures', AIAA Journal pp. 1–9.

Rosenfeld, M., Rambod, E. and Gharib, M. (1998), 'Circulation and formation number of laminar vortex rings', Journal of Fluid Mechanics **376**, 297–318.

Roshko, A. (1954), 'On the drag and shedding frequency of two-dimensional bluff bodies', NACA Report .

Roshko, A. (1961), 'Experiments on the flow past a circular cylinder at very high Reynolds number', Journal of Fluid Mechanics **10**(03), 345–356.

Shadden, S., Astorino, M. and Gerbeau, J. (2010), 'Computational analysis of an aortic valve jet with Lagrangian coherent structures', Chaos **20**.

Shadden, S. C., Lekien, F. and Marsden, J. E. (2005), 'Definition and properties of Lagrangian coherent structures from finite-time Lyapunov exponents in two-dimensional aperiodic flows', Physica D: Nonlinear Phenomena **212**(3–4), 271 – 304.

Sirovich, L. (1987), 'Turbulence and the dynamics of coherent structures part I-III', Quarterly of Applied Mathematics **45**(3), 561–571.

Strykowski, P. J. and Sreenivasan, K. R. (1990), 'On the formation and suppression of vortex 'shedding' at low Reynolds numbers', Journal of Fluid Mechanics **218**, 71–107.

Szepessy, S. and Bearman, P. (1992), 'Aspect ratio and end plate effects on vortex shedding from a circular cylinder', Journal of Fluid Mechanics **234**, 191–217.

Takemoto, Y. and Mizushima, J. (2010), 'Mechanism of sustained oscillations in a fluid flowing past a circular cylinder obstacle', Phys. Rev. E **82**.

Tang, S. and Aubry, N. (1997), 'On the symmetry breaking instability leading to vortex shedding', Physics of Fluids **9**(9), 2550–2561.

Tognarelli, M., Taggart, S. and Campbell, M. (2008), Actual VIV fatigue response of full scale drilling risers: with and without suppression devices, in 'Proceedings of the ASME 27th International Conference on Offshore Mechanics and Arctic Engineering'.

Triantafyllou, G. S., Triantafyllou, M. S. and Chryssostomidis, C. (1986), 'On the formation of vortex streets behind stationary cylinders', Journal of Fluid Mechanics **170**, 461–477.

Van Dyke, M. (1982), 'An album of fluid motion', Parabolic Press .

Von Kármán, T. and Rubach, H. (1912), 'Über den mechanismus des flüssigkeits-und luftwiderstandes', Phys. Z **13**(2).

Wang, Y., Haller, G., Banaszuk, A. and Tadmor, G. (2003), 'Closed-loop Lagrangian separation control in a bluff body shear flow model', Physics of Fluids **15**(8), 2251–2266.

Williamson, C. (1996), 'Vortex dynamics in the cylinder wake', Annual Review of Fluid Mechanics **28**, 477–539.

Williamson, C. H. K. (1989), 'Oblique and parallel modes of vortex shedding in the wake of a circular cylinder at low Reynolds numbers', Journal of Fluid Mechanics **206**, 579–627.

Zdravkovich, M. (1997), 'Flow around circular cylinders; Vol. I fundamentals', Journal of Fluid Mechanics **350**(1), 377–378.

Zhou, J., Adrian, R. J., Balachandar, S. and Kendall, T. (1999), 'Mechanisms for generating coherent packets of hairpin vortices in channel flow', Journal of Fluid Mechanics **387**, 353–396.

Zingg, D. W. and Yarrow, M. (1989), 'A direct procedure for interpolation on a structured curvilinear two-dimensional grid', NASA Technical Memorandum .

Vita

Matthew received his B.S. in Aeronautical and Mechanical Engineering from Clarkson University in 2011, and his M.S. in Mechanical and Aerospace Engineering from Syracuse University in 2012. At Syracuse University he performed fluid dynamics experiments and finite-time Lyapunov exponent (FTLE) analysis towards completion of his dissertation. His research utilized the Syracuse University water tunnel to evaluate the behavior of Lagrangian saddles in bluff body shedding behind a circular cylinder. He studied the numerically simulated flow through a turbulent channel and the numerically simulated and experimentally measured flow in the wake of a circular cylinder using FTLE. He determined an objective vortex shedding time from the acceleration of Lagrangian saddles in the cylinder near-wake. He related the vortex shedding time to a minimum in pressure upstream of the mean separation location that could then be used to inform real-time closed loop flow control algorithms. Matthew has one peer-reviewed first author publication, has another under review, and four published conference proceedings.